

RESEARCH PROJECT

INDUSTRIAL ENGINEERING AND MANAGEMENT

Investigating the structural behaviour of the Ocean Battery



**rijksuniversiteit
 groningen**



Author:

L.Y. Hut S2718960

Supervisors:

1st supervisor: A. Vakis

2nd supervisor: B. Jayawardhana

September 25, 2020

Preface

This Research Project report has been the result of seven months of research conducted by the author, in collaboration with the University of Groningen and the Ocean Grazer Company. The research is focused on the foundation of the Ocean Battery, which is currently being developed by the Ocean Grazer Company. The objective was to analyse this foundation its structural behaviour during the installation of the complete Ocean Battery.

It has been hard work to finalize the project but it was very insightful. As the world changed enormously due to the COVID pandemic, the research became more challenging. Nevertheless, I am proud of the result that is this thesis.

I would like to thank both my supervisors, Prof. dr. A. Vakis and Prof. dr. ir. B. Jayawardhana, to have given me the opportunity for this thesis at the Ocean Grazer research group and for the help during this project. Furthermore I would like to thank the CTO of the Ocean Grazer company, M. van Rooij, who helped me throughout this research with all the details of the design of the system.

At last I would like to thank my friends and family who helped me optimizing the thesis and who supported me these seven months.

Lennard Hut
September 25, 2020

Abstract

Currently, renewable energy is becoming more significant within the total energy generation in the world. The Ocean Grazer company has found an innovative way to store renewable energy from wind farms, by making use of a natural pressure difference found at the bottom of the sea. Through the combination of a flexible bladder with atmospheric pressure and the hydrostatic pressure at the seabed, a surplus of energy can be stored by storing potential energy within a working fluid. The overall battery system, called Ocean Battery, is placed on a foundation that is embedded into the seabed through means of suction caissons. Through the under pressure created by these caissons, the foundation of this battery system is able to suck itself into the seabed. In this research the structural behaviour of the foundation of the battery system is investigated for different types of soils. As the Ocean Grazer company currently has no models available to predict the behaviour of the foundation, there is no certainty to know if the system can be fully deployed. The main categories of soil that are considered are cohesive and cohesionless soils. The analysis is done through a Matlab model, to predict the behaviour in terms of force, pressure and holding capacity, and a COMSOL model to analyse the structural behaviour in terms of stress and displacement. The soils showed different influences on the foundation structure in terms of force, pressure and holding capacity. The cohesive soils show a linear influence on the behaviour, whereas the cohesionless soils show a quadratic influence on the behaviour. The stress and displacement analysis shows that the foundation is not subjected to high enough stress concentrations to be able to let the system fail. The adaptable model obtained in this research shows to be a useful tool to predict the behavior of the foundations for different scale versions of the foundation system.

Contents

List of Figures	7
List of Tables	11
1 Introduction	13
2 Problem Definition	14
2.1 Problem Context	14
2.2 Problem Statement	16
3 Research Scope	17
3.1 System Description	17
3.2 Goal Statement	18
3.3 Research Questions	18
4 Methodology	19
4.1 Simulation Methods	19
4.1.1 FEA and FEM	19
4.1.2 CFD	19
4.2 Simulation Tools	20
4.2.1 COMSOL	20
4.2.2 ABAQUS	20
4.2.3 PLAXIS	20
5 Literature Study	21
5.1 Offshore Embedded Structures	21
5.2 Suction Caissons	22
5.2.1 Suction Caisson Principles	22
5.2.2 Suction Caissons Calculations for Cohesionless Soils	23
5.2.3 Suction Caissons Calculations for Cohesive Soils	30
5.3 Sea Soil Properties	34
5.3.1 The North Sea	34
5.3.2 Cohesive Soils	36
5.3.3 Cohesionless Soils	38
5.4 Welding of metals	40

5.4.1	Welding processes	40
5.4.2	Welding joints	41
6	Model Setup	42
6.1	Modeling Tools	42
6.1.1	Matlab	42
6.1.2	COMSOL	42
6.2	Strategy	42
6.3	Assumptions	43
7	Simulation Results	45
7.1	Matlab Results	45
7.1.1	Cohesionless Soil Results	46
7.1.2	Cohesive Soil Results	59
7.1.3	Prediction Prototype 1 Results	66
7.2	COMSOL Results	68
7.2.1	Cohesionless Soil Results	69
7.2.2	Cohesive Soil Results	81
8	Discussion	89
9	Conclusion	91
10	Recommendations and Limitations	92
11	Bibliography	93
12	Appendices	98
12.1	Appendix A: Unified Soil Classification System	98
12.2	Appendix B: Matlab code	99

List of Figures

1	The two developed prototypes. (a) The single caisson prototype, (b) The scale (2x2) prototype.	14
2	Forces acting on the Ocean Grazer storage system. F_b denotes the buoyancy force, F_w denotes the force due to water pressure, F_g denotes the gravitational force, F_f denotes the friction force and F_s denotes the "suction" force.	15
3	The foundation of the design. (a) Top view (b) Bottom view	17
4	Five types of offshore foundations: (a) Mono-pile, (b) Mono-pod (skirted caisson), (c) Jacket structure, (d) Tripod and (e) Floating anchored foundation (20). . . .	21
5	The deployment phases of a suction caisson: 1) Locating phase, 2) Sinking phase, 3) Self-weight penetration phase, 4) Suction-assisted penetration phase and 5) the decommissioning phase	22
6	The resistance of the soil subjected to the suction caisson (24).	23
7	Sediment map of the North Sea (37).	34
8	The depth profile of the North Sea (38).	35
9	Schematic drawing of the Shielded Metal Arc Welding process (61)	40
10	The five basic weld joints (63)	41
11	Friction Forces Statoil [SC]	46
12	Friction Forces Silica [SC]	46
13	Friction Forces Redhill [SC]	46
14	Friction Forces Luce Bay [SC]	46
15	Required Suction Statoil [SC]	47
16	Required Suction Silica [SC]	47
17	Required Suction Redhill [SC]	47
18	Required Suction Luce Bay [SC]	47
19	Holding Capacity Statoil [SC]	48
20	Holding Capacity Silica [SC]	48
21	Holding Capacity Redhill [SC]	48
22	Holding Capacity Luce Bay [SC]	48
23	Activation sequence for the four chamber model.	49
24	Friction Forces Statoil [FS4]	49
25	Friction Forces Silica [FS4]	49
26	Friction Forces Redhill [FS4]	50
27	Friction Forces Luce Bay [FS4]	50
28	Required Suction Statoil [FS4]	50
29	Required Suction Silica [FS4]	50

30	Required Suction Redhill [FS4]	51
31	Required Suction Luce Bay [FS4]	51
32	Holding Capacity Statoil [FS4]	51
33	Holding Capacity Silica [FS4]	51
34	Holding Capacity Redhill [FS4]	52
35	Holding Capacity Luce Bay [FS4]	52
36	Activation sequence for the five chamber model.	52
37	Friction Forces Statoil [FS5]	53
38	Friction Forces Redhill [FS5]	53
39	Friction Forces Luce Bay [FS5]	53
40	Required Suction Statoil [FS5]	53
41	Required Suction Redhill [FS5]	53
42	Required Suction Luce Bay [FS5]	54
43	Holding Capacity Statoil [FS5]	54
44	Holding Capacity Redhill [FS5]	54
45	Holding Capacity Luce Bay [FS5]	55
46	Activation sequence for the nine chamber model.	55
47	Friction Forces Statoil [FS9]	56
48	Friction Forces Redhill [FS9]	56
49	Friction Forces Luce Bay [FS9]	56
50	Required Suction Statoil [FS9]	57
51	Required Suction Redhill [FS9]	57
52	Required Suction Luce Bay [FS9]	57
53	Holding Capacity Statoil [FS9]	57
54	Holding Capacity Redhill [FS9]	57
55	Holding Capacity Luce Bay [FS9]	58
56	Friction Forces Kaolin [SC]	59
57	Friction Forces Nkossa [SC]	59
58	Friction Forces Qiantang [SC]	59
59	Required Suction Kaolin [SC]	60
60	Required Suction Nkossa [SC]	60
61	Required Suction Qiantang [SC]	60
62	Holding Capacity Kaolin [SC]	61
63	Holding Capacity Nkossa [SC]	61

64	Holding Capacity Qiantang [SC]	61
65	Activation sequence for the four chamber model.	61
66	Friction Forces Kaolin [FS4]	62
67	Friction Forces Nkossa [FS4]	62
68	Friction Forces Qiantang [FS4]	62
69	Required Suction Kaolin [FS4]	63
70	Required Suction Nkossa [FS4]	63
71	Required Suction Qiantang [FS4]	63
72	Holding Capacity Kaolin [FS4]	64
73	Holding Capacity Nkossa [FS4]	64
74	Holding Capacity Qiantang [FS4]	64
75	Activation sequence for the five chamber model.	64
76	Friction Forces Qiantang [FS9]	65
77	Required Suction Qiantang [FS9]	65
78	Holding Capacity Qiantang [FS9]	65
79	Existing prototype of the Ocean Grazer	66
80	Soil type that was found during testing on location (64)	66
81	The testing PVC tube set used during location tests (64)	66
82	Prototype 1 suction Kaolin clay	67
83	Prototype 1 suction Nkossa clay	67
84	Prototype 1 suction Qiantang silt	67
85	Prototype 1 suction Statoil sand	67
86	Stress plot Statoil sand	69
87	Stress plot Silica sand	69
88	Stress plot Redhill sand	69
89	Stress plot Luce bay sand	69
90	Inside of the caisson magnified for Statoil sand.	70
91	Stress over a straight line from bottom to the top in Statoil sand	70
92	Displacement plot Statoil sand	71
93	Displacement plot Silica sand	71
94	Displacement plot Redhill sand	71
95	Displacement plot Luce bay sand	71
96	Stress plot Statoil sand	73
97	Stress plot Silica sand	73

98	Stress plot Redhill sand	73
99	Stress plot Luce bay sand	73
100	Magnification on stress locations for the full system with four active chambers for Statoil sand.	74
101	Displacement plot Statoil sand	74
102	Displacement plot Silica sand	74
103	Displacement plot Redhill sand	74
104	Displacement plot Luce bay sand	74
105	Stress plot Statoil sand	76
106	Stress plot Redhill sand	76
107	Stress plot Luce bay sand	76
108	Magnification on stress locations for the full system with five active chambers for Statoil sand.	77
109	Displacement plot Statoil sand	77
110	Displacement plot Redhill sand	77
111	Displacement plot Luce bay sand	77
112	Stress plot Statoil sand	78
113	Stress plot Redhill sand	78
114	Stress plot Luce bay sand	78
115	Magnification on stress locations for the full system with nine active chambers in Statoil sand	79
116	Displacement plot Statoil sand	79
117	Displacement plot Redhill sand	79
118	Displacement plot Luce bay sand	80
119	Stress plot Kaolin clay	81
120	Stress plot Nkossa clay	81
121	Stress plot Qiantang silt	81
122	Inside of the caisson magnified for Kaolin clay.	82
123	Stress over a straight line from bottom to the top in Kaolin clay	82
124	Displacement plot Kaolin clay	83
125	Displacement plot Nkossa clay	83
126	Displacement plot Qiantang silt	83
127	Stress plot Kaolin clay.	84
128	Stress plot Nkossa clay	84
129	Stress plot Qiantang silt	85

130	Magnification on stress locations for the full system with four active chambers in Kaolin clay.	85
131	Displacement plot Kaolin clay.	85
132	Displacement plot Nkossa clay	85
133	Displacement plot Qiantang silt	86
134	Stress plot Qiantang silt	87
135	Displacement plot Qiantang silt	87
136	Magnification on stress locations for the full system with five active chambers in Qiantang silt	88

List of Tables

1	Variable explanation of the presented equations for the cohesionless soils (equation 1 - 29) (25) (13) (26) (27) (28) (29).	24
2	Variable explanation of the presented equations for the cohesive soils (equation 30 - 43) (25) (33) (28).	30
3	Soil Classifications by ISO standards (39).	35
4	The soil parameters of Kaolin clay (42) (25) (35).	36
5	The soil parameters of Nkossa clay (25) (45).	37
6	The soil parameters of Qiantang river silt clay (35) (47).	37
7	The soil parameters of Silica Sand (35).	38
8	The soil parameters of Statoil Sand (25).	38
9	The soil parameters of Redhill 110 Sand (54) (55).	39
10	The soil parameters of Luce Bay Sand (54) (56).	39
11	Code explanation for Matlab results.	45
12	Self-Weight Penetration Depths for the Single Caisson case.	47
13	Maximum Penetration Depths for the Single Caisson case.	48
14	Self-Weight Penetration Depths for the Full System case.	50
15	Maximum Penetration Depths for the Full System case with 4 chambers.	51
16	Maximum Penetration Depths for the Full System case with 5 chambers.	54
17	Self-Weight Penetration Depths for the Full System case.	62
18	Maximum Penetration Depths for the Full System case in Qiantang River Silt.	63
19	Model and Material settings in the COMSOL models.	68
20	Variations in result values with different meshes for the Statoil sand.	72
21	Stress and displacement of the single caisson for the different cohesionless soils.	72
22	Variations in result values with different meshes for the Statoil sand for the four chamber model.	75

23	Stress and displacement of the Full system for the different cohesionless soils with four active chambers.	75
24	Stress and displacement of the Full system for the different cohesionless soils with five active chambers.	78
25	Stress and displacement of the Full system for the different cohesionless soils with nine active chambers.	80
26	Variations in result values with different meshes for the Kaolin clay.	83
27	Stress and displacement of the single caisson for the different cohesive soils. . . .	84
28	Variations in result values with different meshes for the Kaolin clay for the four chamber model.	86
29	Stress and displacement of the Full system for the different cohesive soils with four active chambers.	87
30	Stress and displacement of the Full system for the different cohesive soils with five active chambers.	88
31	The Unified Classification System of soils (43)	98

1 Introduction

In modern days, the battle against climate change becomes more and more pressing (1). Many companies and universities are investigating new and innovative ways to make the world more sustainable. Tesla is one of those companies that is trying to motivate people to move from fossil fuels to electric and more sustainable technologies by offering electric cars and electric battery (Lithium-ion) packs for households (2). In 2017, Elon Musk placed a tweet containing a bet for the Australian Government. Elon Musk stated that his company would install a battery station with enough capacity to solve the South Australia's power grid problems within a hundred days. If his company would fail, the installation would be free of charge (3). In 2017 Tesla built the enormous battery park within three months (4), and was already tested to their limits when the coal-fired Loy Yang power plant failed (5). The battery pack reacted within milliseconds and saved the south of Australia from a power outage (5).

Lithium-ion based batteries are the most common types of batteries. Tesla is using this type of batteries throughout their designs of electric cars as well as their battery packs (2). However, Lithium is a metal that still needs to be mined from the ground. Consequently, there are still social impacts due to the mining of these metals.

In 2014, the Ocean Grazer project started at the University of Groningen. This project aimed to combine wave energy together with a energy storage based on potential energy (6). From this project the Ocean Grazer company was founded. Through several iterations of the design and research from more than 60 students, the company is working on the first prototype of the battery system which was developed by the company. This battery system, in contrast to the battery system of Tesla, does not require any rare earth metals such as lithium. The invented battery system of the Ocean Grazer company is based on a natural pressure difference between the atmospheric pressure within the system and the hydrostatic pressure outside the system. This system can be combined with several off-shore energy sources such as wind farms, providing a hybrid renewable solution to the energy market.

2 Problem Definition

As stated in the previous section, the Ocean Grazer company is working on a battery system to be able to store renewable energy. The main focus of this research lies on the second prototype on which the company is currently working. This is explained in more detail in section 2.1.

2.1 Problem Context

The Ocean Grazer BV is a start up company that was founded by a research group of the University of Groningen. The research group started in 2014 with research in a innovative wave energy converter. Over the years, more than 60 students worked on graduation projects (both Bachelor and Master level) for the Ocean Grazer. Although the core idea, harvesting energy from waves, did not change, the research that was done over the years led to new iterations of the design of the Ocean Grazer (6).

Currently, the Ocean Grazer company is working on the third iteration of the idea. The main focus of the company is on the storage system. This system can be placed on the seabed and functions as a battery. The battery system of the Ocean Grazer is working by means of a natural pressure difference, between atmospheric pressure and hydrostatic pressure, instead of using lithium ions or other chemical principles. The ocean battery system consists of a reservoir, with a working fluid inside, and a bladder. When an excess of energy is produced, by for example a wind farm, the working fluid is pumped from the reservoir to the bladder. As the battery system is deployed on the seabed, a hydrostatic pressure is acting on the system. When the bladder is inflated, the pressure of the ocean tries to push the fluid back to the reservoir, creating a potential energy. When the bladder is deflated, the fluid flows through turbines, and the stored energy can be send to the power grid (6).

In every technology developing process, the technology readiness levels are used. The technology readiness levels are levels that describe how far a certain technology is developed. The lowest level (according to the European Union) is TRL 1, where the basic principles are observed (7). The highest level, TRL 9, is the level where the actual system/technology is proven in operational environment (7). In the case of the storage system of the Ocean Grazer, the system can be placed between TRL 4, "technology validated in lab" and TRL 5, "technology validated in relevant environment"(7). The reason for placing the system of the Ocean Grazer between these two levels, is the fact that the company is currently working on building a prototype that will be tested in the Eemshaven, while the technology is validated in lab environment.

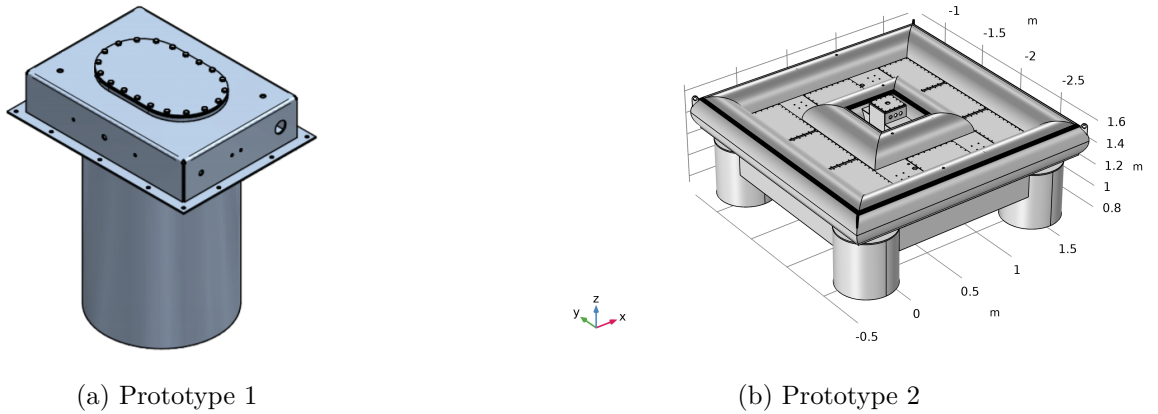


Figure 1: The two developed prototypes. (a) The single caisson prototype, (b) The scale (2x2) prototype.

Within the company, there are three prototypes. These prototypes are used to verify both the tests which were done in the lab and the simulations carried out on computers. The three prototypes are the following:

1. A single caisson with a single powerhouse (figure 1a).
2. A scale model of 2x2 meter (figure 1b).
3. A scale model of 10x10 meter.

Currently, the first prototype is finished and will soon be tested in the test location in the Eemshaven. The second prototype is in development by a company that is specialized in machine building. The third prototype is currently being developed by means of CAD software.

The focus of this project is on the second prototype, the scale model of 2x2 meter. This scale model is build from only steel. The third prototype will consist, in contrary to prototype 2, of multiple materials. This difference will lead to a different structural behaviour. For the second prototype both the reservoirs and the foundation are made of steel, connected with a rubber bladder.

The battery structure will be subjected to different types of forces when deployed on the ocean floor. These forces are subjected by both the surroundings of the structure, as well as the installation of the structure itself. In total there are four circular suction caissons that each account for a quarter of the total holding capacity when activated. If necessary, the other chambers can be activated as a suction caisson as well.

These suction caissons are each producing an underpressure in the caissons, which will result in a suction force acting on the inside of the suction caissons. Besides the suction forces, the structure is subjected to a buoyancy force, which is caused by the displacement of the water volume. Furthermore, the structure is subjected to the hydrostatic pressure, which increases with the depth. The other forces acting on the structure is are the frictional forces that are produces during the installation of the system. The forces are shown in figure 2 schematically.

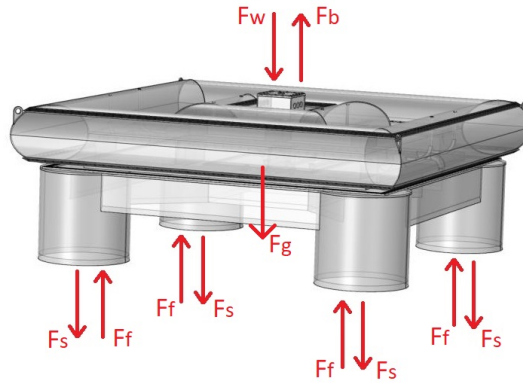


Figure 2: Forces acting on the Ocean Grazer storage system. F_b denotes the buoyancy force, F_w denotes the force due to water pressure, F_g denotes the gravitational force, F_f denotes the friction force and F_s denotes the "suction" force.

Besides the effect of the different forces on the structure, several aspects of the design as shown in figure 1b have to be analysed. As the connections between all the connecting skirts are all welded together, the influence of an oceanic environment on welds is of interest. Another aspect that influences the behaviour of the system, is the soil in which the system will be deployed. The soil determines how well the structure can penetrate the seabed.

2.2 Problem Statement

From the context, as described in section 2.1, it is clear that the Ocean Grazer company has a need for a working simulation model, to be able to investigate the second prototype its structural behaviour. As the company currently has no models to be able to analyse the first scale prototype. Although there are some similarities between the first scale prototype (2x2) and the second prototype (10x10), working models can present useful insights for the development of the 10x10 prototype.

With the context in mind, the following problem statement can be derived:

Currently the Ocean Grazer company has no insight in the structural behaviour through calculation and simulation models, with respect to stresses and deformations, of the foundation of the first scale prototype. Consequently, the company is not able to predict possible weak spots in the structure of the prototype.

3 Research Scope

Within the problem formulated in section 2.2, several boundaries have to be set. These boundaries in the research are stated to make sure that the focus of the research is maintained and the right aspects are investigated. The sections in this chapter are describing the scope and are defining the boundaries of the research.

3.1 System Description

As already stated in the problem context (section 2.1) this research will focus on the second prototype of the company. Due to the complexity of the complete system, only the foundation of the battery system will be investigated in this research. The circular suction caissons are comparable with the first prototype. The foundation of the second prototype is shown in figure 3. The reservoir and the bladder are placed outside the scope in terms of their structures. The forces that are raised from the reservoir and bladder are modelled through external forces that are subjected to the steel foundation.

The system itself consist of three main parts, 1) the four suction caissons, 2) the connecting skirts and 3) the platform. The four suction caissons are enabling the structure to install itself into the seabed. In figure 3b, it can be seen that there are 5 compartments besides the circular caissons. These compartments can be, if necessary, be activated as suction caisson as well. The installation is done in two phases. The first phase is called the self-weight penetration phase. In this phase, the foundation penetrates the seabed through the weight of the structure. The second phase, the suction-assisted penetration phase, is the phase where an under pressure is created in the suction caissons such that the foundation is installed in the seabed. The skirts are offering stability to the platform and form a connection between the four different suction caissons. The skirts will, together with the suction caissons, penetrate the seabed. This provides stability as well for the situation where the structure is operational and installed into the seabed. The platform of the system is a platform that provides a leveled area on which the battery system (reservoir and bladder) can rest. The platform should be able to support the weight of the battery system and withstand the dynamic loads that are subjected to it by charging and discharging the battery.

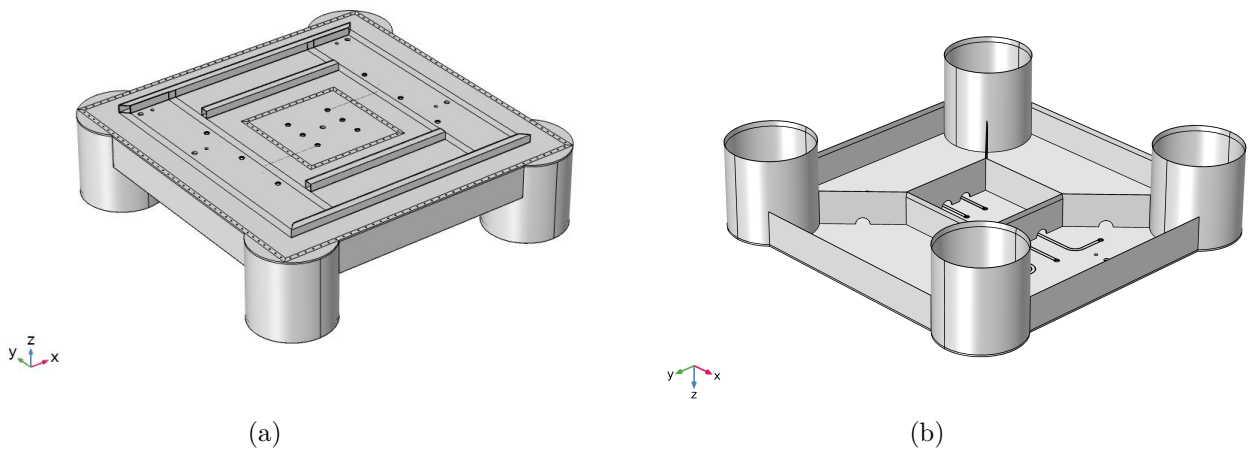


Figure 3: The foundation of the design. (a) Top view (b) Bottom view

3.2 Goal Statement

From the problem context (section 2.1), problem statement (section 2.2) and the system description (section 3.1) the goal of the research can be formulated. The goal that is formulated takes into account the aspects stated in these previous mentioned sections. The aim is to obtain a model that can simulate the behavior of the steel foundation that is being subjected to different forces.

The goal can be formulated to the goal statement given below:

The goal of this research is to investigate, through formulating MATLAB calculation models and COMSOL simulation models, the structural behaviour of the foundation of the second prototype of the Ocean Grazers Battery system within 6 months

3.3 Research Questions

From the problem context and the system description it becomes clear what the scope of the project should be in order to solve the problem of the Ocean Grazer. To obtain an solution for the problem, while reaching the goal, a research question has to be formulated. The research question itself can be divided into several sub questions, that are helpful into dividing the scope of the research into smaller segments.

The main research question that can be obtained is the following:

[RQ]: *How does the foundation of the second prototype, of the Ocean Grazers battery system, behave under different loads and in different soil types in terms of stress and displacement?*

The sub reserach questions that together should be able to answer the main research question are the following questions:

- **[SQ1]** How does the foundation of the second prototype behave under static loading?
- **[SQ2]** What is the influence of the stress and displacement on the welds of the structure?
- **[SQ3]** What is the influence of the cohesionless soil type on the structural behaviour of the structure?
- **[SQ4]** What is the influence of the cohesive soil type on the structural behaviour of the structure?

4 Methodology

Suction caissons are used throughout the field of offshore structures that need a foundation in the seabed. Due to its wide area of application, a significant amount of research has been conducted in the behavior of these suction caissons in their application functions.

4.1 Simulation Methods

Modelling and simulating can be done through various methods. Within engineering, the Finite Element Method and Finite Element Analysis are often used throughout engineering problems (8). However, in other fields of engineering using Computational Fluid Dynamics (CFD) analysis is more common (9). The method that is chosen, depends on the situations that are being modelled and the outcomes which are of interest. Both methods are used in research investigating the behaviour and phenomena corresponding with suction caissons.

4.1.1 FEA and FEM

To analyse the structural behavior of a design, the Finite Element Analysis method can be used to determine the different stress concentrations and deformations. The analysis method is a method that uses a numerical method, called the finite element method. This method divides the structure, which is analyzed, into a finite number of elements. A design can be defined through millions of elements. The finite element method uses these elements to compute solutions to partial differential equations (PDEs), which are defining the physical problem (8). By using different sets of discretizations, the finite element method approximates the real solution through these PDEs.

The research of M. Zeinoddini, S. Mousavi and M. Abdi is one of the investigations on the behaviour of suction caissons by using the finite element method (10). In this research, the researchers are investigating the behaviour of a suction caisson that is penetrating the seabed under the influence of the suction. The research of S.D. Nielsen is another example of an investigation on suction caissons by using the finite element method (11). In the research of Nielsen, the author is investigating the tensile capacity of suction caissons that are deployed in cohesionless soils such as sands or gravels (11).

4.1.2 CFD

The Computational Fluid Dynamics method is commonly used in fields of engineering that are working with fluids and flows. The CFD method can approximate phenomena based on conservation laws that are the basis of fluid mechanics (9). Within the CFD method the finite element method can be used in order to solve for the equations that are prescribing the flow phenomena. However, other methods can be used for CFD as well such as the finite difference method or finite volume method (9).

An example of a research done by using CFD for suction caissons is the research of Z. Guo, D. Jeng, W. Guo and R. He (12). The authors of this article started a research on the flow phenomena at the edge of suction caissons. This phenomena is called the seepage effect and is the flow of sand that is occurring at the edge of the suction caisson. In this research, the CFD method can be applied to model the flow in the seepage effect. Another research that applies the CFD method is the research of A.E. Alluqmani, M.T. Naqash and O. Harireche (13). In this research, the authors investigate the pore pressure around the edge of the suction caisson.

4.2 Simulation Tools

The main tools that are used to simulate the behavior of structures are 3D simulation software packages. These software packages are used to visualize the behaviour of the design, without having to produce a working prototype. Therefore, simulating designs in 3D software is highly cost effective for companies. Engineers can easily make changes to the design and come up with a final design that meets the requirements. It would be more expensive to first build a prototype and test it, finding out that changes have to be made to the design. There are many software packages available for simulations, each having their advantages. Several of these software packages will be discussed in this section.

4.2.1 COMSOL

The COMSOL multiphysics software package is a package that offers many options for the user. Through combining several sets of physic layers, different situation can be simulated through this software. COMSOL can be used widely within different industries due to its large spread of physics and options to simulate different situations. COMSOL offers a additional geomechanics module. However, this module is not added in the standard version of COMSOL (14).

4.2.2 ABAQUS

ABAQUS is a software package from the software developer Dassault Systèmes (also known for acquiring SolidWorks). The ABAQUS software was acquired by Dassault Systèmes in 2005 and was than re-branded to SIMULIA (15). The Simulia software package is a non-linear FEM package, which means that the software can deal with, for example, non linear materials such as rubber. The ABAQUS software is widely used in the industries, from the aerospace industry to the marine and offshore engineering industry (16).

4.2.3 PLAXIS

In contrast to the other two mentioned software packages, PLAXIS is not a software package that is developed for multiple industries. The PLAXIS software is specifically designed for geotechnical FEA simulations (17). The software is able to simulate aspects such as soil structure stability, ground water/heat flow and soil interactions such as foundation work, excavation and tunneling.

5 Literature Study

5.1 Offshore Embedded Structures

Offshore engineering is a field of engineering where engineers are designing offshore structures. An offshore structure can be defined, according to S. Chakrabarti, as a structure that "has no fixed access to dry land and may be required to stay in position in all weather conditions. Offshore structures may be fixed to the seabed or may be floating" (18). The field of offshore engineering started after the end of the second world war, when the first offshore oil rig was installed 18 miles from the coast of Louisiana in 1947 and for a depth of 6 meters (19). In comparison, oil rigs today can cover depths that are exceeding depths of 2000 meters (19). Besides the oil and gas industries, other renewable energy sectors started to work in with offshore structures, such as wind farms. The first offshore wind farm was constructed in Denmark (Vindeby) and counted eleven wind turbines. This wind farm was located 3 km from the main land and was built in 1991 (20).

The structures that are build for the offshore industries, oil rigs or windmills, need a foundation on the seabed in order to function properly. There are different possibilities in offering a foundation for the offshore embedded structures. Five of these foundation possibilities are shown in figure 4. The foundations shown are the mono-pile, mono-pod, jacket structure, tripod and floating anchored foundation. The mono-pile and mono-pod foundations are used in more shallow waters and these foundations are hammered into the soil (19). The jacket structure foundation, Tripod or Floating anchored foundation are used for larger water depths. Often these type of foundations are used in combination with suction caissons (19). The jacket structure is a metal structure that resembles electricity masts and is embedded in the seabed with the use of suction caissons. The tripod foundation consist of a steel tripod with at the ends a suction caisson in place. The floating anchored foundation is a foundation type where a floating is coupled, through a set of cables, to one or more anchors (suction caissons for example) (20).

There is a sixth foundation possibility which is not shown in figure 4, which is the gravity based foundation. In a gravity based foundation the structure is installed completely on the seabed. However, the base of the structure is significantly larger, and heavier, than the rest of the structure. The gravity that is applied on the heavy structure at the base makes that the structure remains in its position. To be able to choose a type of foundation that is suitable for the application for which the offshore structure is designed, several key aspects have to be taken into account (21). The key aspects for choosing one of the foundation types are, among others, the bearing capacity of soils, water depth, climatic loads, installation, dismantling (21).

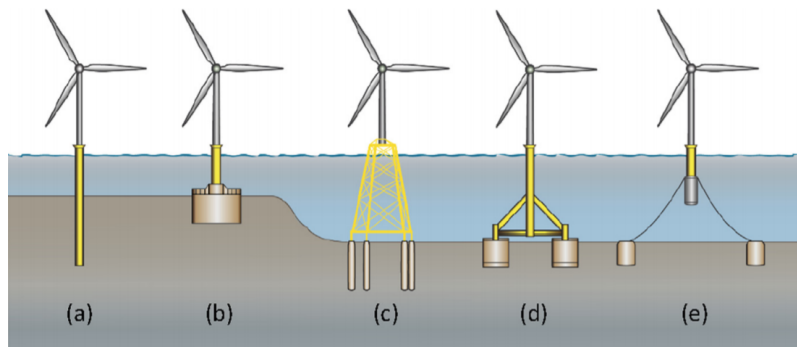


Figure 4: Five types of offshore foundations: (a) Mono-pile, (b) Mono-pod (skirted caisson), (c) Jacket structure, (d) Tripod and (e) Floating anchored foundation (20).

5.2 Suction Caissons

Suction caissons are widely used in the offshore industry. Especially for the oil and gas industry these suction caissons proved to be a useful foundation (13). Besides the oil and gas industry, the suction caissons are also used in the renewable energy industry (22), to provide a stable foundation for large structures such as windmills. These type of foundation structures all have one significant advantage, the fact that they can be easily decommissioned (13). This decommissioning can be done by removing the under-pressure that is created between the inside of the caisson and the sand.

From figure 4 in section 5.1, structures (b), (d) and (e) are making use of suction anchors. In each of these structures, the overarching idea of providing a foundation is the same. However, each of the structure foundations are designed on different conditions of both the depth of the sea bottom, as well as the structure for which it has to provide a foundation.

5.2.1 Suction Caisson Principles

The principle of a suction caisson is based on forming an under-pressure, such that the caisson can suck itself into the bottom of the sea. As previously mentioned, the decommissioning of the caisson is quite easily done by removing the underpressure. The caisson can then be raised to the surface level and be transported to the main land for maintenance or re-location.

There are several stages to the deployment of suction caissons, which are depicted in figure 5. The first two stages are stages where the caisson is positioned. The stages 3 and 4 of figure 5 are together the operational phase of the suction caisson. The last stage is the decommissioning phase, where the caisson is released from the seabed and can be transported to the shore for maintenance.

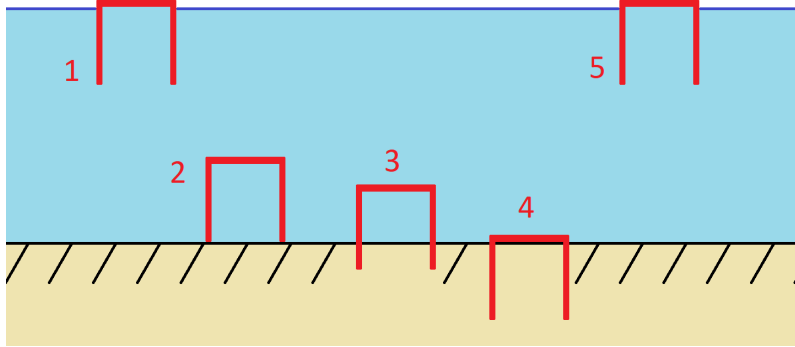


Figure 5: The deployment phases of a suction caisson: 1) Locating phase, 2) Sinking phase, 3) Self-weight penetration phase, 4) Suction-assisted penetration phase and 5) the decommissioning phase

The self-weight penetration phase is the phase where the suction caisson is placed on the desired seabed location, where it will penetrate the seabed due to the gravitational force. The hydrostatic water pressure that is provided by the water depth, can assist the self weight of the caisson for the self-weight penetration phase. Especially in deep waters, this hydrostatic pressure is useful for the self-weight penetration phase. In relatively shallow waters, this assistance is significantly lower (23).

The suction that is enforced, during the suction-assisted phase, on the structure will lead to a development of stresses in the structure. An example of stresses that are developed during the installation are stresses due to friction. The soil of the seabed will have a significant resistance on the structure in terms of friction. This friction is schematically shown in figure 6. From

this figure, it becomes clear that the different parts of the suction caisson each have their own resistance (24).

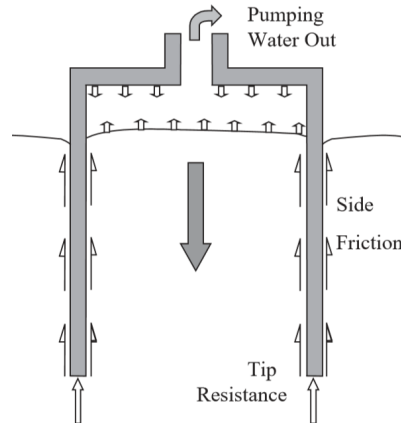


Figure 6: The resistance of the soil subjected to the suction caisson (24).

5.2.2 Suction Caissons Calculations for Cohesionless Soils

When using suction caissons as a foundation of an offshore structure, several parameters have to be calculated in order to design the optimal caisson. The soil in which the caisson is deployed, plays a significant role in these calculations as each type of soil reacts differently to certain interactions. G.T. Houlsby and B.W. Byrne investigated two cases for suction caissons to be installed, one case for sand like soils (cohesionless soils) and one case for clay and other similar soils (cohesive soils) (25). The clay like soils are discussed in 5.2.3.

The calculations provided by Houlsby and Byrne are split in two, one set of calculations is describing the self-weight penetration phase, whereas the other set of calculations describes the suction-assisted penetration phase. These sets of equations will be explained in the dedicated paragraphs below. The formulas take into account the three resistance factors, as described in figure 6. In table 1, the different parameters with the corresponding unit and definition are presented. These parameters are used in the equations that are elaborated on in this section.

5.2.2.1 Table with variable descriptions for cohesionless soils

The definition of the variables used in equations 1 - 29 are given in table 1.

Variable	Unit	Definition
A_i	$[m^2]$	Inner area of the chamber
A_o	$[m^2]$	Outer area of the chamber
a	$[-]$	Ratio of excess pore pressure at caisson tips
C	$[m]$	Average circumference of the plate
C_i	$[m]$	Inner circumference of the plate
C_o	$[m]$	Outer circumference of the plate
D	$[m]$	Average diameter of the caisson
D_i	$[m]$	Inner diameter of the caisson
D_o	$[m]$	Outer diameter of the caisson
h	$[m]$	Installed depth of the caisson
h_w	$[m]$	Height of water above the mudline
h_0	$[m]$	Initial penetration depth
K	$[-]$	Lateral earth pressure coefficient
k_f	$[-]$	Permeability ratio inside to outside of caisson
m	$[-]$	Multiple of the diameter for enhanced stress
N_q	$[-]$	Bearing capacity factor (overburden)
N_γ	$[-]$	Bearing capacity (self-weight)
p_a	$[Pa]$	Athmospheric pressure
p_{abs}	$[Pa]$	Absolute pressure
R	$[m]$	Radius of the suction caisson
s	$[Pa]$	Suction within caisson with respect to ambient seawater pressure
s_{min}	$[Pa]$	Minimal suction within caisson with respect to ambient seawater pressure
Q_b	$[N]$	Tensile bearing capacity of the soil
Q_h	$[N]$	Holding Capacity for suction caisson
Q_{so}	$[N]$	side shear on the outside wall
t	$[m]$	Thickness of the suction caisson walls
V'	$[N]$	Effective vertical load
W_c	$[N]$	Submerged weight of the caisson
W_s	$[N]$	Submerged weight of the soil
z	$[-]$	Vertical coordinate below the mudline
Z_i	$[-]$	Formula simplification factor inside caisson
Z_o	$[-]$	Formula simplification factor outside caisson
γ'	$[kN/m^3]$	Effective unit weight of the soil
γ_w	$[kN/m^3]$	Unit weight of water
δ	$[\circ]$	Interface friction angle
σ'_{vi}	$[MPa]$	Effective vertical stress at the inside of the caisson
σ'_{vo}	$[MPa]$	Effective vertical stress at the outside of the caisson
ϕ	$[\circ]$	Internal friction angle of the soil
ω	$[\circ]$	The angle between the boundary and the central axis of the wall.

Table 1: Variable explanation of the presented equations for the cohesionless soils (equation 1 - 29) (25) (13) (26) (27) (28) (29).

5.2.2.2 Self-weight penetration phase

The total friction that is applied by the soil to the suction caisson is the sum of the friction at the tips, the outside and the inside (25). The overarching equation to calculate the vertical load of the suction caisson is given by the following equation (equation 1)

$$V' = \frac{\gamma' h^2}{2} (K \tan \delta)_o (\pi D_o) + \frac{\gamma' h^2}{2} (K \tan \delta)_i (\pi D_i) + \left(\gamma' h N_q + \gamma' \frac{t}{2} N_\gamma \right) (\pi D t) \quad (1)$$

In this equation each term describes one of the resistance factors. The first term denotes the friction on the outside of the caisson, the second term denotes the friction on the inside of the caisson and the third term denotes the friction at the tips of the caisson.

The factors N_γ and N_q can be calculated through the following two equations, based on the internal friction angle of the soil (equations 2 and 3) (30).

$$N_q = \frac{e^{2\pi(0.75 - (\phi/360)) \tan(\phi)}}{2 \cos^2(45 + (\phi/2))} \quad (2)$$

$$N_\gamma = \frac{2(N_q + 1) \tan(\phi)}{1 + 0.4 \sin(4\phi)} \quad (3)$$

The disadvantage of equation 1 is the fact that, according to Houlsby and Byrne, the enhancement of vertical stress close to the pile, due to friction forces further in the caisson, are not taken into account. Ignoring this stress factor can lead to a underestimation of the force and suction that are needed for the full penetration (25).

When the effect described above is taken into account the following equation can be obtained:

$$V' = \gamma' Z_o^2 \left(\exp \left(\frac{h}{Z_o} - 1 - \left(\frac{h}{Z_o} \right) \right) (K \tan \delta)_o (\pi D_o) \right. \\ \left. + \gamma' Z_i^2 \left(\exp \left(\frac{h}{Z_i} - 1 - \frac{h}{Z_i} \right) \right) (K \tan \delta)_i (\pi D_i) + \sigma'_{end} (\pi D t) \right) \quad (4)$$

In this equation, several parameters (Z_o , Z_i and σ'_{end}) are functions themselves. The value for σ'_{end} depends on a inequality that prescribes different situations. The values for both Z terms are given by equation 5 and 6.

$$Z_i = \frac{D_i}{4(K \tan \delta)_i} \quad (5)$$

$$Z_o = \frac{D_o(m^2 - 1)}{4(K \tan \delta)_o} \quad (6)$$

The inequality that is needed to solve for the value of σ'_{end} is given in equations 7 and 8.

$$\text{If } \sigma'_{vi} - \sigma'_{vo} < \frac{2tN_\gamma}{N_q} \quad \text{Then } \sigma'_{end} = \sigma'_{vo} N_q + \gamma' \left(t - \frac{2x^2}{t} \right) N_\gamma \quad \text{where } x = \frac{t}{2} + \frac{(\sigma'_{vo} - \sigma'_{vi}) N_q}{4\gamma' N_\gamma} \quad (7)$$

$$\text{If } \sigma'_{vi} - \sigma'_{vo} \geq \frac{2tN_\gamma}{N_q} \quad \text{then } \sigma'_{end} = \sigma'_{vo} N_q + \gamma' t N_\gamma \quad (8)$$

The values of σ'_{vi} and σ'_{vo} are denoted by the following equations (equation 9 and 10).

$$\sigma'_{vi} = \gamma' Z_i \left(\exp \left(\frac{z}{Z_i} \right) - 1 \right) \quad (9)$$

$$\sigma'_{vo} = \gamma' Z_o \left(\exp \left(\frac{z}{Z_o} \right) - 1 \right) \quad (10)$$

The initial penetration depth is highly important, due to the fact that it provides an initial seal which is needed for the suction in the suction-assisted penetration phase (13). The weight of the structure will result in a initial "self-weight" penetration depth, where the friction is equal to the self weight as shown in equation 1 and equation 4. To calculate the initial penetration depth, or self-weight penetration, the equation given by the article written by Alluqmani, Naqash and Harireche can be used. The equation is for the initial penetration depth is the shown below (13).

$$h_0 = \frac{-N_q t + \sqrt{(N_q t)^2 - 2K \tan \delta \left(N_\gamma t^2 - \frac{V'}{\pi R \gamma'} \right)}}{2K \tan \delta} \quad (11)$$

The vertical load that is expressed in this equation is the dry weight of the structure minus any of the buoyancy effects (31).

5.2.2.3 Suction-assisted penetration phase

In the case of the suction-assisted penetration phase, the suction has a contribution to the total amount of stress that is subjected to the caisson. According to the article of Houlsby and Byrne, the pressure in the caisson is denoted by variable s . This leads to the absolute pressure being described in equation 12.

$$p_{abs} = p_a + \gamma_w h_w - s \quad (12)$$

When the pore pressure at the tips of the caisson are assumed to be as , the absolute pressure is denoted by equation 13.

$$p_{abs} = p_a + \gamma_w (h_w + h) - as \quad (13)$$

Taking into account these two absolute pressure factors, and using the article of Houlsby and Byrne, the following equation can be obtained to denote the suction-assisted penetration phase.

$$\begin{aligned} V' + s \left(\frac{\pi D_i^2}{4} \right) &= \left(\gamma' + \frac{as}{h} \right) Z_o^2 \left(\exp \left(\frac{h}{Z_o} \right) - 1 - \left(\frac{h}{Z_o} \right) \right) (K \tan \delta)_o (\pi D_o) \\ &+ \left(\gamma' - \frac{(1-a)s}{h} \right) Z_i^2 \left(\exp \left(\frac{h}{Z_i} \right) - 1 - \left(\frac{h}{Z_i} \right) \right) (K \tan \delta)_i (\pi D_i) \\ &+ \left(\left(\gamma' - \frac{(1-a)s}{h} \right) Z_i \left(\exp \left(\frac{h}{Z_i} \right) - 1 \right) N_q + \gamma' t N_\gamma \right) (\pi D t) \end{aligned} \quad (14)$$

In this equation the variable a is given, which denotes the flow factor around the caisson. The value of variable a can be determined through equation 15.

$$a = \frac{a_1 k_f}{(1 - a_1) + a_1 k_f} \quad \text{where } a_1 = c_0 - c_1 \left(1 - \exp \left(- \frac{h}{c_2 D} \right) \right) \quad (15)$$

In the equation for a_1 , the values for c are: $c_0 = 0.45$, $c_1 = 0.36$ and $c_2 = 0.48$, according to Houlsby and Byrne (25).

5.2.2.4 Limits to the Suction Assisted Phase

The article of Houlsby and Byrne proposes, besides the set of equations discussed in the previous paragraphs, several equations that describe the limitations to which these equations can hold. For the suction assisted penetration phase a limit exists for the suction that can be applied to the system.

As the suction is increased over time, the upward hydraulic gradient at the inside of the suction caisson will approach the value at which the phenomenon of *pipng failure* might occur (25). This piping phenomenon leads to the caissons inside and caissons tip effective vertical stresses fall both to zero. If the suction is increased any further beyond this point, the local piping phenomena will be induced. The local piping in the suction caisson will most likely cause a major inflow of water into the caisson, while the caisson will not penetrate the soil any further (25). This situation will occur when the following equality holds (equation 16).

$$\gamma' h - (1 - a)s = 0 \quad (16)$$

This equality in equation 16, can be substituted into the equation 14 and rewritten to the following equation (equation 17)

$$V' + \frac{\gamma' h}{(1 - a)} \frac{\pi D_i^2}{4} = \frac{\gamma'}{(1 - a)} Z_o^2 \left(\exp \left(\frac{h}{Z_o} \right) - 1 - \left(\frac{h}{Z_o} \right) \right) (K \tan \delta)_o + (\gamma' t N_\gamma) (\pi D t) \quad (17)$$

When equation 17 is solved for h , the maximal penetration depth with the use of suction can be calculated. This equation has to be solved for each step of h , due to the fact that a is dependent on h (25).

The limitation of the suction assisted penetration has been investigated through several researches. One of the researches investigated the maximum penetration depth for suction caissons in sand conditions (27). The researchers established an equation that prescribes the minimum suction needed for different penetration depths. The equations that are proposed in this research, are based on the equations given by Houlsby and Byrne. The proposed equation for minimum by the article of W. Yuqi is given in equation 18 (27). For this equation, there is one governing assumption.

$$s_{min} = \frac{(1 + K)Z \left(\exp \left(\frac{h}{Z} \right) - 1 \right) M \gamma' t + 4 \gamma' N K \tan \delta - \frac{V'}{(\pi R)}}{\left(R - \left(\frac{2 N K \tan \delta - \left((1 + K)Z \left(\exp \left(\frac{h}{Z} \right) - 1 \right) t M + 4 N K \tan \delta}{h} \right) (1 - a) \right) \right)} \quad (18)$$

Within this equation, the parameters M and N are given by the following two equations (equation 19 and 20).

$$M = \frac{(1 + \sin(\phi))^2}{(1 - \sin(\phi))} \exp((\pi + 2\omega) \tan(\phi)) \quad (19)$$

$$N = Z^2 \left(\exp \left(\frac{h}{Z} \right) - 1 - \frac{h}{Z} \right) \quad (20)$$

In addition to parameter M, given in equation 19, the ω value can be determined through equation 21.

$$\omega = \frac{1}{2} \arctan \frac{2K \tan \delta}{|1 - K|} \quad (21)$$

The variable K that is given in the equation is the lateral earth pressure coefficient, and is recommended to have a value of $K = 0.8$ (27).

5.2.2.5 Skirt Penetration in Cohesionless Soils

As can be seen in figure 3, the foundation of the Ocean Grazer contains connecting plates between the suction caissons. The calculation procedure of the connected plates is obtained from the global equation of Houlby and Byrne (equation 1) (25). This equation is repeated below.

$$V' = \frac{\gamma' h^2}{2} (K \tan \delta)_o (\pi D_o) + \frac{\gamma' h^2}{2} (K \tan \delta)_i (\pi D_i) + \left(\gamma' h N_q + \gamma' \frac{t}{2} N_\gamma \right) (\pi D t) \quad (22)$$

Although this equation is expressed in with the diameter variable, and therefore suitable for cylindrical shapes, it can be rewritten to a form which is suitable for rectangular shapes (32). As can be seen from equation 1, each of the friction terms is multiplied with the circumference. In the current equation, the area corresponds to a circular form. To describe the frictional terms for the rectangular shape of the connection skirts, the circumference for a rectangle can be used instead of the circular circumference. This will lead to the following equation for the self-weight penetration phase. Where in this equation C stands for the circumference.

$$V' = \frac{\gamma' h^2}{2} (K \tan \delta)_o (C_o) + \frac{\gamma' h^2}{2} (K \tan \delta)_i (C_i) + \left(\gamma' h N_q + \gamma' \frac{t}{2} N_\gamma \right) (C t) \quad (23)$$

When the non-circular caissons are activated, equation 14 can be rewritten for non-circular shapes. This will lead to the following equation 24.

$$\begin{aligned}
V' + sA_i = & \left(\gamma' + \frac{as}{h} \right) Z_o^2 \left(\exp \left(\frac{h}{Z_o} \right) - 1 - \left(\frac{h}{Z_o} \right) \right) (K \tan \delta)_o (\pi C_o) \\
& + \left(\gamma' - \frac{(1-a)s}{h} \right) Z_i^2 \left(\exp \left(\frac{h}{Z_i} \right) - 1 - \left(\frac{h}{Z_i} \right) \right) (K \tan \delta)_i (\pi C_i) \\
& + \left(\left(\gamma' - \frac{(1-a)s}{h} \right) Z_i \left(\exp \left(\frac{h}{Z_i} \right) - 1 \right) N_q + \gamma' t N_\gamma \right) (\pi C t)
\end{aligned} \tag{24}$$

In this equation, the values for Z_o and Z_i are rewritten to the equations given in equations 25 and 26.

$$Z_i = \frac{A_i}{(C_i(K \tan \delta)_i)} \tag{25}$$

$$Z_o = \frac{mA_o - A_o}{(C_o(K \tan \delta)_o)} \tag{26}$$

5.2.2.6 Holding Capacity in Cohesionless Soils

The holding capacity is a performance indicator of a suction caisson. This capacity determines the force the structure can withstand a so called pullout force. When the pullout force is exceeding the holding capacity of the suction caisson, the caisson will be withdrawn from the seabed (28). The pullout load causes the suction water pressures to dissipate and given enough time, the loading will result in the withdrawal of the caisson (28). The article of M.Iskander states that the pullout capacity of a cylindrical suction caisson in undrained conditions is equal to the equation given in equation 27 (28).

$$Q_h = Q_{so} + Q_b + W_c + W_s \tag{27}$$

In this equation, Q_p denotes the holding capacity, Q_{so} denotes the side shear on the outside wall of the caisson, Q_b denotes the tensile bearing capacity of the soil, W_c denotes the submerged weight of the caisson and W_s denotes the submerged weight of the soil plug. Both the side shear on the outside wall and the tensile bearing capacity are described by the article of L.Hung (29). Both terms in the holding capacity equation are given by equation 28.

$$Q_{so} = Q_b = \frac{\gamma' h}{2} * K \tan \delta \pi * D_{av} h \tag{28}$$

The equation shows that for cohesionless soils, the holding capacity is a function of the installation depth with the order of two. Therefore, there is a quadratic relation between the holding capacity and the installation depth. The submerged weight can be calculated through adding all the components of the foundation and multiply the weight by the gravitational constant. The submerged soil weight is calculated by the following equation:

$$W_s = \left(\frac{\pi D_o^2}{4} \right) h \gamma' \tag{29}$$

5.2.3 Suction Caissons Calculations for Cohesive Soils

As the previous section (section 5.2.2) showed the calculations of the physics of suction caissons in cohesionless soils, this section focuses on the calculation for suction caissons in cohesive soils. For cohesive soils, the same distinction in calculation sets can be made as was described in section 5.2.2, the self-weight penetration phase and the suction assisted phase are considered for the cohesive calculations. However, the set of equations will differ significantly from the equations for cohesionless soils. The equations describing the behaviour of suction caissons in cohesive soils are presented in the article of Houlsby and Byrne (25). In table 2 the different used parameters are shown with the corresponding unit and definition. These parameters are used in the equations that are elaborated on in this section.

5.2.3.1 Table with variable descriptions for cohesive soils

The definition of the variables used in equations 30 - 43 are given in table 2.

Variable	Unit	Definition
A_i	$[m^2]$	Inner area of the chamber
C	$[m]$	Average circumference of the plate
C_i	$[m]$	Inner circumference of the plate
C_o	$[m]$	Outer circumference of the plate
D	$[m]$	Average diameter of the caisson
D_i	$[m]$	Inner diameter of the caisson
D_o	$[m]$	Outer diameter of the caisson
D_m	$[m]$	Diameter multiple for enhanced stress
f	$[-]$	bearing capacity correction coefficient
h	$[m]$	Installed depth of the caisson
N_c	$[-]$	Bearing capacity factor (cohesion)
N_c^*	$[-]$	Bearing capacity factor (uplift)
N_q	$[-]$	Bearing capacity factor (overburden)
Q_b	$[-]$	Tensile bearing capacity of the soil
Q_h	$[N]$	Holding Capacity for suction caisson
Q_{so}	$[N]$	side shear on the outside wall
s	$[Pa]$	Suction within caisson with respect to ambient seawater pressure
s_{crit}	$[Pa]$	Critical suction to the suction assisted phase
s_{u0}	$[kPa]$	Shear strength at the mudline
s_{u1}	$[kPa]$	Average shear strength over depth of the skirt
s_{u2}	$[kPa]$	Shear strength at caisson skirt tip
t	$[m]$	Thickness of the suction caisson walls
V'	$[N]$	Effective vertical load
W_c	$[N]$	Submerged weight of the caisson
W_s	$[N]$	Submerged weight of the soil
α	$[-]$	Adhesion factor
γ'	$[kN/m^3]$	Effective unit weight of the soil
ρ	$[kPa/m]$	Rate of change of shear strength with depth
ϕ	$[^\circ]$	Internal friction angle of the soil

Table 2: Variable explanation of the presented equations for the cohesive soils (equation 30 - 43) (25) (33) (28).

5.2.3.2 Self-weight penetration phase

The total friction, for the cohesive soil case, that is applied by the soil is the sum of the adhesion on the outside and inside of the caisson, as well as the tips (25). The adhesion of the soil can be calculated by multiplying the adhesion factor α to the value of the undrained strength of the soil (25). The total frictional load can be described by equation 30.

$$V' = h\alpha_o s_{u1}(\pi D_o) + h\alpha_i s_{u1}(\pi D_i) + (\gamma' h N_q + s_{u2} N_c)(\pi D t) \quad (30)$$

In this equation the terms s_{u1} and s_{u2} are undrained shear strength characteristics. In the undrained case, the term N_q is equal to 1. In the upcoming equations, this term is set to 1 and therefore the term N_q is already taken into account. The term s_{u1} is the average undrained shear strength between the mudline and the depth h , whereas the term s_{u2} is the undrained shear strength at depth h . Both terms can be calculated through the following equations (equation 31 and 32).

$$s_{u1} = s_{u0} + \rho \frac{h}{2} \quad (31)$$

$$s_{u2} = s_{u0} + \rho h \quad (32)$$

In these two equations, the term s_{u0} is the shear strength at the mudline and ρ is the rate of change of shear strength with depth. The value for the bearing capacity factor N_c is dependent on the angle of friction of the soil and the overburden bearing capacity factor (N_q). This relation is shown in equation 33 (33).

$$N_c = \frac{N_q - 1}{\tan(\phi)} \quad (33)$$

5.2.3.3 Suction assisted penetration phase

Once the self-weight penetration is reached, the suction caisson will switch from phase. At the end of the self-weight penetration phase, the penetration of the soil will stop and the suction will be applied to the caisson. At this transition point, the seal that is formed during the self-weight penetration enables the suction to be applied (25).

When the suction is applied to the caisson, the total effective vertical load on the top plate of the caisson increases. This is due to an additional term, which is equal to the suction times the area of the top plate (25). This leads to the the formula shown in equation 34.

$$V' + s \left(\frac{\pi D_i^2}{4} \right) = h\alpha_o s_{u1}(\pi D_o) + h\alpha_i s_{u1}(\pi D_i) + (\gamma' h - s + s_{u2} N_c)(\pi D t) \quad (34)$$

It is important to note that in equation 34, the soil strengths (terms s_{u1} and s_{u2}) are not one value, as they change with respect to the depth h . If the equation is solved for s , the equation will be a quadratic function in terms of the depth h (25).

5.2.3.4 Limits to the Suction Assisted Phase

When the suction is applied to the suction caisson, the penetration depth will increase. However, there exists a limit to the penetration that can be achieved with the suction. As the article by Houlsby and Byrne states, if the difference between the vertical stress inside and outside

the caisson, at the level of the caisson tip, exceeds a certain value, local plastic failure might occur (25). This plastic failure prevents any further penetration of the suction caisson and the soil flows into the caisson. The phenomenon for the prevention of further penetration for the cohesive soil case is called the *"reverse bearing capacity"* problem (25). The reverse bearing capacity failure occurs when the equality in equation 35 is satisfied.

$$-s + \gamma' h + \frac{\pi D_i h \alpha_i s_{u1}}{\left(\frac{\pi D_i^2}{4}\right)} = \gamma' h + \frac{\pi D_o h \alpha_o s_{u1}}{\pi \left(\frac{D_m^2 - D_0^2}{4}\right)} - N_c^* s_{u2} \quad (35)$$

In this equation, the term N_c^* stands for the bearing capacity factor appropriate for uplift of a buried circular footing (25). The factor D_m is equal to $D_m = mD$, where $m=1$ is used. This can be approximated with the use of the ratio given in equation 36 (25).

$$\frac{N_c^*}{4\alpha} = 3 \quad (36)$$

The critical suction is investigated by W. Yuqi through limit analysis (34). Using the provided equation of W. Yuqi, the maximum suction can be determined (equation 37) (34).

$$s_{crit} = \left(\gamma' h + \frac{4h\alpha_i s_{u1}}{D_i} \right) - \left(\gamma' h + \frac{(1 + 1.5/D_o)^2 \alpha_o s_{u1}}{1 + 3h/D_o} \right) + (2 + \pi + \arcsin \alpha_o + \arcsin \alpha_i + \sqrt{1 - \alpha_o^2} + \sqrt{1 - \alpha_i^2}) s_u \quad (37)$$

5.2.3.5 Skirt Penetration in Cohesive Soils

As was mentioned in section 5.2.2.5, the ocean grazer foundation contains connecting plates between the suction caissons. Therefore, there are additional friction sources, that add to the total friction term. To calculate these frictional terms, the main formula can be used, as presented in equation 34. However, instead of using the diameter in this function, the circumference is used (as was done in section 5.2.2.5). The equation for the self-weight penetration phase is given in equation 38. In this equation, the C denotes the circumference.

$$V' = h\alpha_o s_{u1}(C_o) + h\alpha_i s_{u1}(C_i) + (\gamma' h + s_{u2} N_c)(Ct) \quad (38)$$

When the non-circular caissons are activated, equation 34 can be rewritten for non-circular shapes. This will lead to the following equation 39.

$$V' + sA_i = h\alpha_o s_{u1}(C_o) + h\alpha_i s_{u1}(C_i) + (\gamma' h - s + s_{u2} N_c)(Ct) \quad (39)$$

5.2.3.6 Holding Capacity in Cohesive Soils

As mentioned for the cohesionless soil case, the holding capacity is a performance indicator for the suction caissons. The holding capacity denotes how much force is needed to pull out a suction caisson from the ground (28). For the cohesive soils, the same initial holding capacity or pullout capacity is given by equation 40.

$$Q_h = Q_{so} + Q_b + W_c + W_s \quad (40)$$

The denotations in the equation are the same as in equation 27. Q_p denotes the holding capacity, Q_{so} denotes the side shear on the outside wall of the caisson, Q_b denotes the tensile bearing capacity of the soil, W_c denotes the submerged weight of the caisson and W_s denotes the submerged weight of the soil plug. The tensile bearing capacity and the side shear at the outside of the caisson in cohesive soils are calculated are given by the article of M. Iskander (28) and given in equations 41 and 42.

$$Q_{so} = \alpha s_{u0} \pi D_o h \quad (41)$$

$$Q_b = s_{u0} N_c f \left(\frac{\pi D_o^2}{4} \right) \quad (42)$$

In equation 42 the term f denotes a bearing capacity correction coefficient which is takes a value of 0.7 (35). For the term N_c commonly the value is set to 9 (28). The submerged weight can be calculated through adding all the components of the foundation and multiply the weight by the gravitational constant. The submerged soil weight is calculated by the following equation:

$$W_s = \left(\frac{\pi D_o^2}{4} \right) h \gamma' \quad (43)$$

From equations 40 up to 43 it can be observed that the relationship between the holding capacity and the penetration depth in cohesive soils is a linear relationship, as the equations are only dependent on a linear term in h .

5.3 Sea Soil Properties

As suction anchors are used in different applications and locations, the anchors will have to deal with different types of soil. The article of Houlby and Byrne, which is discussed in section 5.2.2 and section 5.2.3, proposes different calculation sets for different types of soil. The article divides the soils in two main categories, the cohesive soils (clay soil types) and cohesionless soils (sand soil types). In this section, different soils and their properties are discussed.

5.3.1 The North Sea

The Ocean Grazer Company has decided to deploy the the battery system in the North Sea. As the North Sea stretches from Belgium up to Norway and from the Netherlands to the United Kingdom, the sediment on the seabed is not a constant soil. In order to determine which types of soils are present in the North Sea, the data of the *European Marine Observation and Data Network* (EMODnet) can be considered. The EMODnet website (36) provides multiple types of data with respect to the environment of the North Sea.

The EMODnet institution consists of more than 150 different organisations. Together, these organisations are focusing on assembling marine data, products and metadata in order to provide less fragmented data to both the public and private end users (36). The website of EMODnet provides a mapviewer where the different sediments are shown (37). Figure 7 shows the different sediments found across the North Sea. As is visible in the figure, the North Sea consists of multiple types of soils. The three main soils are *Mud to Muddy Sand*, *Sand* and *Coarse sediments*.

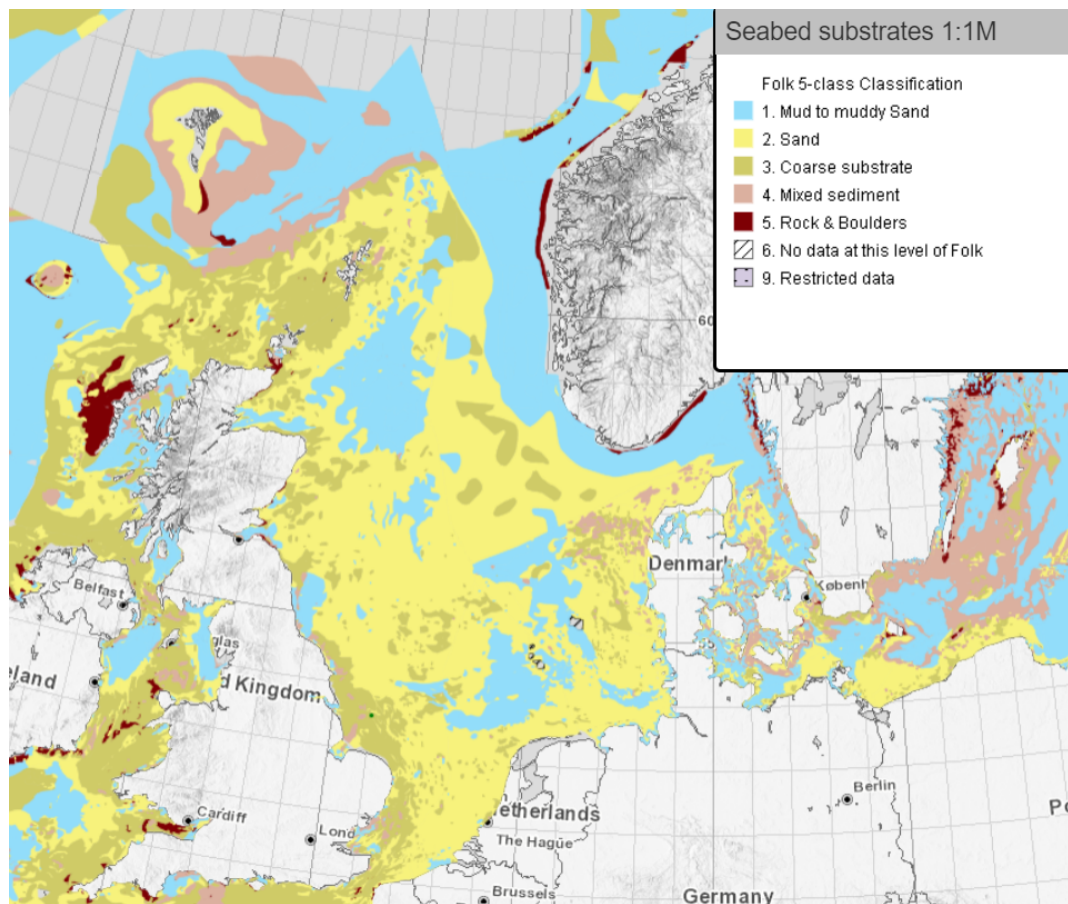


Figure 7: Sediment map of the North Sea (37).

Besides the sediment, the EMODnet website offers a map with the depths of the North Sea (38).

As the hydrostatic pressure increases with the depth, the force on the Ocean Grazer's Battery system changes. The depth of the sea differs at every location and might change throughout the years due to erosion and sediment migration. The depth profile of the North Sea is shown in figure 8.

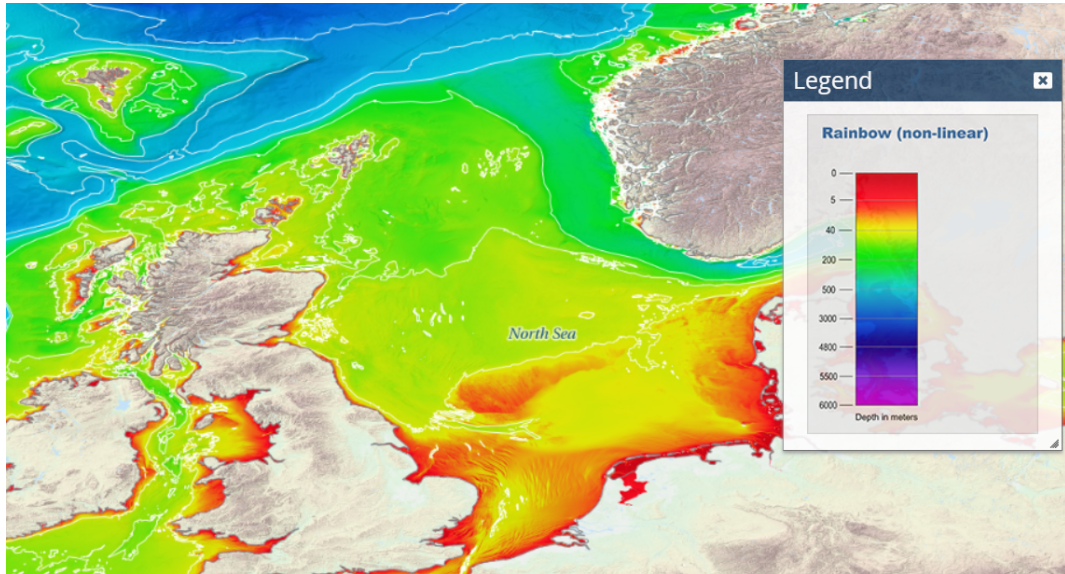


Figure 8: The depth profile of the North Sea (38).

From both figure 7 and figure 8, it can be concluded that for the shallow parts of the North Sea, the soil is mostly sand. When the depth increases, the soil becomes more muddy. As can be seen from figure 7, the coast around the United Kingdom mainly consists of the coarse sediment, whereas the coast of the Netherlands mainly consists of a sandy soil type.

The International Organization for Standardization published a classification document, in which different soils can be identified or classified. The table that is provided within this document is shown in table 3, which classifies different soils based on their particle sizes (39).

Soil Group	Type of particles	Range of Particle Sizes (mm)
Very coarse soil	Large Boulder	> 630
	Boulder	$200 < \text{size} \leq 630$
	Cobble	$63 < \text{size} \leq 200$
Coarse soil	Gravels	$2.0 < \text{size} \leq 63$
	Coarse gravel	$20 < \text{size} \leq 63$
	Medium gravel	$6.3 < \text{size} \leq 20$
	Fine Gravel	$2.0 < \text{size} \leq 6.3$
	Sands	$0.063 < \text{size} \leq 2.0$
	Coarse sand	$0.63 < \text{size} \leq 2.0$
	Medium sand	$0.20 < \text{size} \leq 0.63$
	Fine sand	$0.063 < \text{size} \leq 0.20$
Fine soil	Silts	$0.002 < \text{size} \leq 0.063$
	Coarse silt	$0.02 < \text{size} \leq 0.063$
	Medium silt	$0.0063 < \text{size} \leq 0.02$
	Fine silt	$0.002 < \text{size} \leq 0.0063$
	Clay	≤ 0.002

Table 3: Soil Classifications by ISO standards (39).

5.3.2 Cohesive Soils

The sediment that is called a cohesive soil is defined as a soil that consists of different types of clay. The main characteristic of these soil types is that the particles have a tendency of adhering to other particles. Other characteristics are low-strength, easy deformability and fine grains (40). When subjected to the ISO standards, it can be classified as a fine soil with particle sizes up to 0.0063 mm (39). Furthermore, a soil is only considered a cohesive if the amount of fines (silt and clay-sized materials) exceeds 50% by the weight (40).

5.3.2.1 Kaolin Clay

Kaolin clay is a cohesive soil that can be found throughout the world and is one of the common types of clay. Kaolin clay is commonly known as *china clay*, as it is an essential ingredient for the manufacturing of Chinese porcelain (41). Kaolin clay is a clay that behaves as a plastic. When the kaolin is mixed with 20-30% of water, it can be molded under pressure (41), making it a perfectly plastic clay.

According to the research of H. Zhou (42), the undrained shear strength can be taken as $s_u = 4 + 1.5h [kPa]$. In this linear dependency, h denotes the depth below the seabed surface (42). From this dependency, the mudline shear strength and the shear strength rate can be obtained. The research of Zhou also provides values for the effective soil weight (γ') and the lateral earth pressure coefficient (K), which are $\gamma' = 6.5 [kN/m^3]$ and $K = 0.8$ respectively (42). The article of Housby and Byrne suggest that an adhesion factor of 0.5 is suitable for different types of clay (25).

The angle of friction can be found through the *Unified Soil Classification System* (USCS) classification (43). The complete classification is added to the appendix A. As kaolin clay is an organic type of clay and it has a high plasticity, the classification of *Organic clays of high plasticity* is chosen for kaolin clay (44). The angle of friction for these type of clays has a minimum value of 17° and a maximum value of 35° (44), which results to an average friction angle of 26° . With the use of the angle of friction, the three bearing capacity factors can be calculated (equations 2, 3 and 33). Table 4 shows all these important values.

Variable Name	Symbol	Value	Unit
Particle Diameter	D_{Kaolin}	0.03	$[mm]$
Effective Soil Weight	γ'	6.5	$[kN/m^3]$
Overburden Bearing Capacity	N_q	14.210	$[-]$
Self-Weight Bearing Capacity	N_γ	12.624	$[-]$
Cohesion Bearing Capacity	N_c	27.085	$[-]$
Lateral Earth Pressure Coefficient	K	0.8	$[-]$
Adhesion Factor	α	0.5	$[-]$
Mudline Shear Strength	s_{u0}	4.0	$[kPa]$
Shear Strength Rate	ρ	1.5	$[kPa/m]$
Angle of Friction	ϕ	26	$[^\circ]$

Table 4: The soil parameters of Kaolin clay (42) (25) (35).

5.3.2.2 Nkossa Clay

Housby and Byrne propose several examples in their calculation manual for suction caissons (25). One of these examples is the suction caisson research of J.L. Colliat (45). A normal consolidated clay is a clay where the effective overburden pressure p_0 that is currently present, is the maximum pressure to which the layer has been subjected at any point in history (46).

The location of interest in the research of Colliat, is the Nkossa field located in the Gulf of Guinea. The site where the suction caisson is deployed is slightly north of the Congo river, at the edge of the continental slope (45). Normal consolidated clays are a plastic type of clay just as kaolin clay (45). According to the article of Houlsby and Byrne, the effective soil weight (γ') of the normal consolidated clay is equal to $6kN/m^3$. The average shear strength at the mudline is equal to $5kPa$, whereas the rate of change in the shear strength is $1.67kPa/m$. The article states that an adhesion factor of 0.3 is suggested by Colliat is based on scale field tests and therefore an adhesion factor of 0.45 would be more suitable (25). The consolidated clay can be classified as a clay of high plasticity which is compacted, which results in a friction angle of 19° . The soil parameters of the Nkossa clay can be found in table 5.

Variable Name	Symbol	Value	Unit
Particle Diameter	D_{Nkossa}	0.002	$[mm]$
Effective Soil Weight	γ'	6.0	$[kN/m^3]$
Overburden Bearing Capacity	N_q	6.701	$[-]$
Self-Weight Bearing Capacity	N_γ	4.693	$[-]$
Cohesion Bearing Capacity	N_c	16.558	$[-]$
Lateral Earth Pressure Coefficient	K	0.8	$[-]$
Adhesion Factor	α	0.45	$[-]$
Mudline Shear Strength	s_{u0}	5	$[kPa]$
Shear Strength Rate	ρ	1.67	$[kPa/m]$
Angle of Friction	ϕ	19	$[^\circ]$

Table 5: The soil parameters of Nkossa clay (25) (45).

5.3.2.3 Qiantang River Silt Clay

In the thesis of N. van Dijken (35), the Qiantang river clay is given as an example for a silt type of clay. The Qiantang river silt is found, as the name states in the Qiantang river in China, near the city Hangzhou (47). This type of soil is often found in the offshore windfarm locations of Chinas coast (47). The properties of these types of clays are considered to be in between the sand and clay properties (47).

These type of silty clays, that are between the properties of sand an clay are seen in more harbor environments. The harbor muds are extremely plastic, organogenic silty clays that have a liquid to soft consistency (48). The values of the different parameters, are shown in table 6.

Variable Name	Symbol	Value	Unit
Particle Diameter	$D_{Qiantang}$	0.029	$[mm]$
Effective Soil Weight	γ'	8.823	$[kN/m^3]$
Overburden Bearing Capacity	N_q	50.351	$[-]$
Self-Weight Bearing Capacity	N_γ	61.390	$[-]$
Cohesion Bearing Capacity	N_c	66.695	$[-]$
Lateral Earth Pressure Coefficient	K	0.8	$[-]$
Adhesion Factor	α	0.5	$[-]$
Mudline Shear Strength	s_{u0}	6	$[kPa]$
Shear Strength Rate	ρ	1.35	$[kPa/m]$
Angle of Friction	ϕ	36.5	$[^\circ]$

Table 6: The soil parameters of Qiantang river silt clay (35) (47).

5.3.3 Cohesionless Soils

The sediment that is called a cohesionless soil is commonly type of sand. The main characteristics of a cohesionless soil is that it is a free-running type of soil, of which the strength depends on the friction angle (ϕ) (49). In contrast to the cohesive soils, the cohesionless soils do not have an adhering tendency. The particle sizes of these types of soils have a range from 0.063 up to 6.3 mm. Using the ISO standards, the cohesionless soils can be classified as coarse soils (39).

5.3.3.1 Silica sand

One of the most common sand like materials is silica sand. The silica (chemical formula SiO_2nH_2O) which are originating from the shells of microscopic marine organisms and organisms such as sponges (50). Silica sand is used throughout different industrial applications and is seen as a valuable mineral resource (51).

Variable Name	Symbol	Value	Unit
Particle Diameter	D_{silica}	0.322	[mm]
Effective Soil Weight	γ'	5.993	[kN/m ³]
Overburden Bearing Capacity	N_q	47.156	[—]
Self-Weight Bearing Capacity	N_γ	56.6545	[—]
Lateral Earth Pressure Coefficient	K	0.8	[—]
Angle of Friction	ϕ	36	[°]
Permeability ratio	k_f	1	[—]

Table 7: The soil parameters of Silica Sand (35).

5.3.3.2 Statoil Sand

The statoil sand is the soil found at the location where the Draupner E riser platform was installed, by the company Statoil, in the North Sea. The Statoil field is located to the southwest of the lower Norwegian coast. The Draupner E platform was installed in 1994, with a depth of 70 meters (25). In 1994 and 1995, the soil was investigated for the use of a foundation with a 12 meter diameter caisson in the research of Tjelta (52). In 1995 a second foundation structure was placed in the same field. This second foundation, called Sleipner T, enabled researchers Erbrich and Tjelta (53) to investigate and formulate a design methodology for these type of foundation structures (25). This second structure was designed with a 15 meter diameter caisson.

Variable Name	Symbol	Value	Unit
Particle Diameter	$D_{Statoil}$	0.1 - 1	[mm]
Effective Soil Weight	γ'	8.500	[kN/m ³]
Overburden Bearing Capacity	N_q	173.285	[—]
Self-Weight Bearing Capacity	N_γ	271.7170	[—]
Lateral Earth Pressure Coefficient	K	0.8	[—]
Angle of Friction	ϕ	45	[°]
Permeability ratio	k_f	3	[—]

Table 8: The soil parameters of Statoil Sand (25).

5.3.3.3 Redhill 110 Sand

In the research of F. Villalobos, two different types of sand are investigated with respect to the influence on a suction caisson (54). One of these sand types is the Redhill 110 sand, which is also used in the research of Blakeborough and Byrne (55). The Redhill 110 sand is a sand that

is found in the southeast of England (54). The sand itself is considered to be a high silica sand, which has a quartz content of 98.8% (54). This sediment is formed from the shallow water deposits from the cretaceous age (54). The sand itself is characterised as a fine sand (54).

The parameters for the Redhill 110 sand type are shown in table 9.

Variable Name	Symbol	Value	Unit
Particle Diameter	$D_{Redhill}$	0.1 - 1	$[mm]$
Effective Soil Weight	γ'	7.82	$[kN/m^3]$
Overburden Bearing Capacity	N_q	47.156	$[-]$
Self-Weight Bearing Capacity	N_γ	56.6545	$[-]$
Lateral Earth Pressure Coefficient	K	0.41	$[-]$
Angle of Friction	ϕ	36	$[^\circ]$
Permeability ratio	k_f	5	$[-]$

Table 9: The soil parameters of Redhill 110 Sand (54) (55).

5.3.3.4 Luce Bay Sand

In the same research of Villalobos, the Luce Bay sand is mentioned. This type of soil is found in the Luce Bay in Scotland, located north of the Isle of Man. The sand found in this bay is characterised as a dense type of sand (54). This type of soil is also used in a field research of Houlsby, Kelly and Byrne (56). In this research the different parameters are found through Cone Penetration Tests (CPT).

The parameters of the Luce Bay sand are shown in table 10

Variable Name	Symbol	Value	Unit
Particle Diameter	$D_{LuceBay}$	0.1 - 1	$[mm]$
Effective Soil Weight	γ'	10.3	$[kN/m^3]$
Overburden Bearing Capacity	N_q	173.285	$[-]$
Self-Weight Bearing Capacity	N_γ	271.717	$[-]$
Lateral Earth Pressure Coefficient	K	0.293	$[-]$
Angle of Friction	ϕ	45	$[^\circ]$
Permeability ratio	k_f	5	$[-]$

Table 10: The soil parameters of Luce Bay Sand (54) (56).

5.4 Welding of metals

Having discussed the different soil types that influence the behaviour of suction caissons, this section elaborates on the different welding processes that might influence the structure. Within the offshore industry, fatigue stress is a major reason for concern. The welding process has to be carefully selected in order to make sure that there are no undesirable changes in the weld joints (57).

The most common approach for joining two metals together nowadays is through the means of welding (58). Through the years different forms of welding were invented, starting with gas welding processes. In these type of processes, oxygen and acetylene are used to produce a flame that contains enough heat to be able to weld metal pieces to each other. Around the same time, resistance welding and arc welding were invented. These two processes use an electrical current to be able to weld pieces of metal together (58).

5.4.1 Welding processes

The main principle of welding is connecting two pieces of metal with each other by means of heating the material locally, to be able to form a bond between the metals on the desired location (59). Generally, the high energy dense heat sources are applied to prepared edges of the materials that have to be welded (59). There are several types that produce a heat source which is suitable for welding, such as fuel gases, electron beams, electric arc or friction heat (59). As there are different types of welding with different heat sources, the American Welding Society (AWS) developed a terminology for the welding engineering field, called the AWS A-3.0-94 'Standard Weld Terms and Definitions'. This terminology is used as a engineering standard and is used world wide (59).

Developing marine and offshore structures often need a welding process to weld components together. As there are many different welding processes, a few are commonly used for the construction of offshore structures (60). The commonly used welding processes in the offshore industry are shielded metal arc welding (SMAW), gas metal arc welding (GMAW), submerged arc welding (SAW), flux-cored arc welding (FCAW) and gas tungsten arc welding (GTAW) (60). All of these mentioned welding processes are in the same overarching category, namely all methods mentioned are examples of the arc welding process.

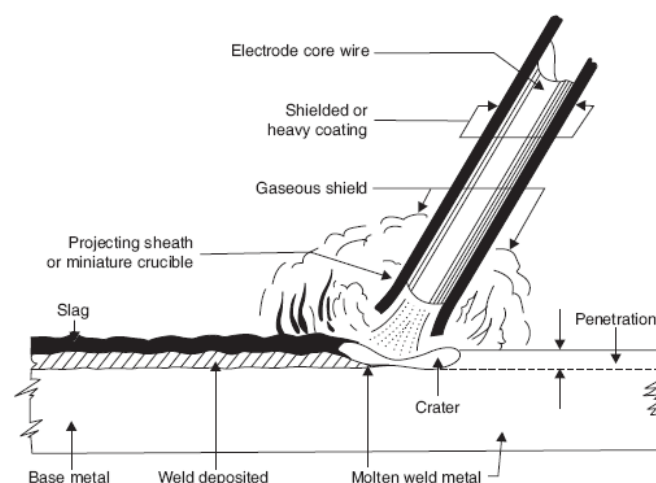


Figure 9: Schematic drawing of the Shielded Metal Arc Welding process (61)

The arc welding process is named for the melting process of the base material, as the melting of the base material is caused by an electrical heat source (62). A schematic drawing of the arc

welding process is given in figure 9 (61). The arc within this process is established between an electrode and the metal work piece (62). The arc forms a local crater where, when cooled down, the weld (or slag) is formed, as can be seen in figure 9. During the process welding material can be added. This welding material is, when used, meant to fill up the slag (62).

5.4.2 Welding joints

In the welding processes, there are different methods in joining the different metals by welding. With every welding process, different joints can be designed for the work piece (63). The five basic weld joints that are commonly used are the butt weld, the lap joint weld, the fillet weld, the edge weld and the corner weld. All these five basic welds are shown in figure 10. The fillet joint shown in the figure is also called a "T" joint, when welded on both sides.

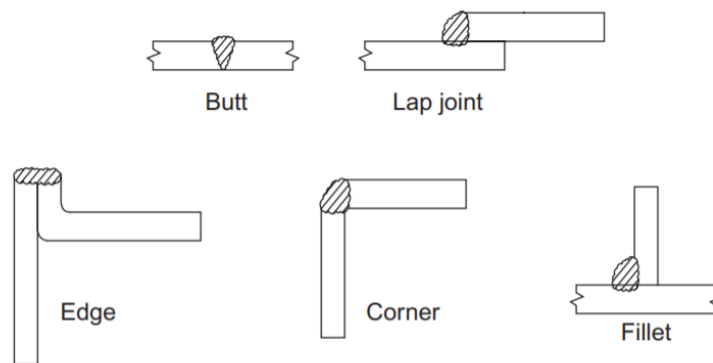


Figure 10: The five basic weld joints (63)

When designing the overall structure, the welds of the structure already have to be taken into account (57). A weld within a designed structure is often the the weakest part of the design. The reason for the weld being the weakest part is that the weld has a different metallurgical structure compared to the base material (57).

Stress concentrations in weld joints can cause devastating failure of the designed structure. During cyclic loading, fatigue failure can occur at stress levels that are normally not high enough to lead to a failure of the structure (57).

6 Model Setup

This section will discuss the model and how it is obtained in this research. The tools, strategy and assumption will each be discussed, after which the model will be thoroughly discussed. The results from the simulations will be discussed in the next chapter (Chapter 7).

6.1 Modeling Tools

Within the research, two different sets of software are used, Matlab and COMSOL. The first software package, Matlab, is used in this research as a calculation software package. The second software package, COMSOL, is mainly used for carrying out the simulations of the model and the analysis on the structural behaviour.

6.1.1 Matlab

The Matlab software is used to write a script which can be used for different designs that the Ocean Grazer company is currently engineering. Several complex equations are used to describe the Ocean Grazer system. The written script can be used to obtain quick insights in the outcomes of these equations.

One of the requirements of the script is that it should be adaptable to different designs on which the Ocean Grazer company is working. Therefore, the script should be written in such a way that, when different design parameters are changed, the code adapts all the calculations to the changed parameters.

Several physical elements of the system are calculated through this Matlab script, such as the forces acting on the system or the required suction. The outcomes of these physical elements can be translated to the COMSOL model to be able to analyse the structural behaviour that the system will display when subjected to these physical elements. The end result of the Matlab code for this research is added to appendix B.

6.1.2 COMSOL

As previously mentioned in the previous section, the simulation software that is used in this research is the COMSOL software package. The model that is derived is based on the existing CAD model of the second prototype (the 2x2 meter scale model). The design of the foundation of the battery system is analysed in COMSOL through different steps, which will be explained in the next section (section 6.2). The main reason to build the model through different steps is the complexity of the system.

The model mainly focuses on the structural mechanics of the system, as the stress and deformation are of interest within this research. Within the COMSOL model, the different sets of equations can be applied with analytic functions. These analytic functions can be plotted in the COMSOL software and be checked with the Matlab script.

The COMSOL model is split up in phases, which correspond to the phases discussed in section 5.2.1. Splitting the model up in phases makes it possible to analyze the structural behaviour of the system throughout the different phases.

6.2 Strategy

The model for the Ocean Grazers foundation is built in a step by step plan, where complexity is added per step. This is done to obtain more insight in the physics of the foundation, as well as obtaining a clear overview in adding the boundary conditions. Within the research, there is

a distinction of two cases for the results. The two cases are the single caisson case and the full system case. This distinction is used in both the MATLAB model as the COMSOL model.

The single caisson case is used to be able to analyse the behaviour of the suction caisson itself and the effect of soil (in terms of the frictional forces). First the single case is modelled in MATLAB. With the code formulated, the equations of Houslby and Byrne are used to calculate different parameters (frictional forces, required suction etc.) and give initial insights in the system. The calculated parameters from the code are then used within the COMSOL model. The COMSOL model provides insight in the structural behaviour of the design.

From the single caisson, insights can be obtained for the building of the models for the scaled system. This scaled version of the system is, just as the single caisson, first modelled in MATLAB from which several parameters are analysed. These parameters are again filled in the COMSOL model to investigate the structural behaviour. As the design of the company contains complex details in the foundation such as pipes and holes, the design is first recreated in the SolidWorks software. The SolidWorks model is saved as an .step file and imported into COMSOL. The scale model is divided into three subcases. This is done in order to be able to analyse the behaviour when the three combinations of suction caissons are activated.

The MATLAB model is made in two fold for each case, one for the cohesionless soils and one for the cohesive soils. At the end of the research a final code is obtained with the possibility for adjusting parameters. Through some prompt windows, the end user can adjust design parameters, but can also choose one of the soils specified in this research. The COMSOL model is built as one model, where different parameters can be filled in.

6.3 Assumptions

As mentioned in the previous section, the design of the company is rather complex. Therefore, several assumptions are made in order to simplify the model. When the model becomes more simple in certain places, the computer has less difficulty with the calculation procedures. However, when drawing conclusions from the outcomes, these assumptions have to be taken into consideration. The assumptions made for this research are stated below together with a brief explanation.

Assumption 1

The first assumption made is concerning the tips of the circular caissons. In the design of the Ocean Grazer company, these tips are slanting from the inside to the outside. This means that the thickness at the bottom is smaller than higher up the lower part of the caisson. This slanted edge is only for the first three centimeters in height.

Assumption 2

The second assumption made is concerning the calculation of the frictional terms when the plates enter the seabed. As the equations of Houslby and Byrne are not specified for other shapes than the circular shapes. As the equations of Houslby and Byrne can be rewritten in terms of circumference, there is an opportunity to use the circumferences of other shapes within the equations to obtain an estimation for the plates and other chambers.

Assumption 3

The next assumption that is made following from assumption 2 and corresponds to the calculation of the circumferences of the plates (when the non-circular caissons are inactive) and the non-circular caissons (when active). When the non-circular caissons are inactive, the circumferences are calculated through connecting the plates and form a square. With the thickness taken into account, the terms can be added.

In the case that the trapezoidal chambers are active, the circumference is calculated through

adding the separate distances. For the location where the circular caissons are connected to the trapezoidal chambers, the length is calculated with the formula for calculating a segment of a circle.

Assumption 4

The fourth assumption is made concerning the weight that is corresponding to each of the suction caissons. As the trapezoidal caissons are bigger than the other caissons, these caissons might have a bigger influence. However, as the specific distribution of the weight of the reservoir and bladder is difficult to determine, the assumption is made that the different caissons are taking each an equal amount of weight.

Assumption 5

The fifth assumption made is that each of the caissons apply an equal amount of suction. This means that the full system can gradually enter the seabed, and the critical suction holds for each of the caissons. As the area of the circular caissons are the smaller than the other chambers.

Assumption 6

The last important assumption made is concerning the welds of the full system model. In the CAD file of the Ocean Grazer company, the welds are not present. In the single caisson case, different sizes of fillet radii will be used to see the influence of the size of possible welds. For the full system model, the applied fillets are set to be 3 mm in radius. These fillets are applied to all the sharp corners in the design.

7 Simulation Results

This section shows the results obtained from both the MATLAB code and the COMSOL model. First the MATLAB results will be discussed, after which the COMSOL results are discussed. The results are split in the same distinction as was shown in section 5.2 for the different calculation sets. The distinction is made between the cohesive soils and cohesionless soils. The soils that are used in the simulations are the same soils which were discussed in section 5.3.

7.1 Matlab Results

The first results that will be discussed are the results from MATLAB, that show initial insights in the behaviour of the prototype. In appendix B, the final Matlab code is given. This code is adaptable to other design dimensions as well, through the use of prompts. For the MATLAB models, complexity is added through each iteration or case. The main and sub cases that are considered in the MATLAB models are the following:

1. The single caisson model.
2. The full system model
 - (a) Four chamber model.
 - (b) Five chamber model.
 - (c) Nine chamber model.

The sub cases that are found for the full system case, are due to the fact that the space between the skirts can be used as a suction chamber as well. This is useful for example if the four suction caissons on the corners cannot apply enough suction to completely be deployed or if piping occurs.

To be able to distinguish the different cases, the plots each contain a code in the description. This code denotes the case that is presented. The explanation of the different codes are found in table 11.

Code	Case description
SC	Single Caisson case.
FS4	Full System case with 4 chambers.
FS5	Full System case with 5 chambers.
FS9	Full System case with 9 chambers.

Table 11: Code explanation for Matlab results.

7.1.1 Cohesionless Soil Results

This section shows the results obtained from the MATLAB code for the cohesionless soil cases. The results are described for all cases and subcases, each in a corresponding section. The single caisson case will be discussed first after which the full system cases are discussed.

7.1.1.1 The single caisson model

The first model is the single suction caisson model. This model shows the behaviour of single circular suction caissons and can be used to see how the equation of Houlsby and Byrne work. Several plots can be obtained from the model, of which the total resistance forces plot, the required suction vs critical suction and the holding capacity are the most important plots to obtain the insights of the system. In figures 11 upto figure 14 the frictional forces in the suction caisson are shown for the four sand soils.

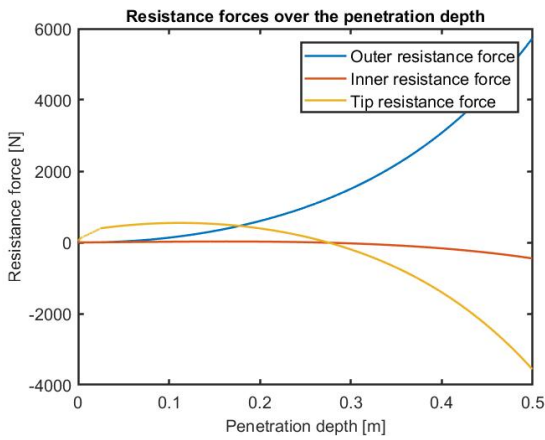


Figure 11: Friction Forces Statoil [SC]

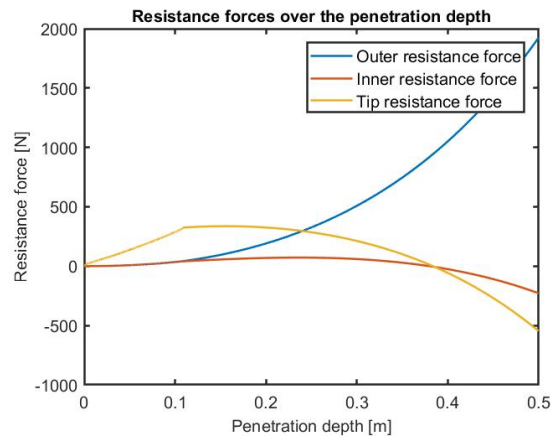


Figure 12: Friction Forces Silica [SC]

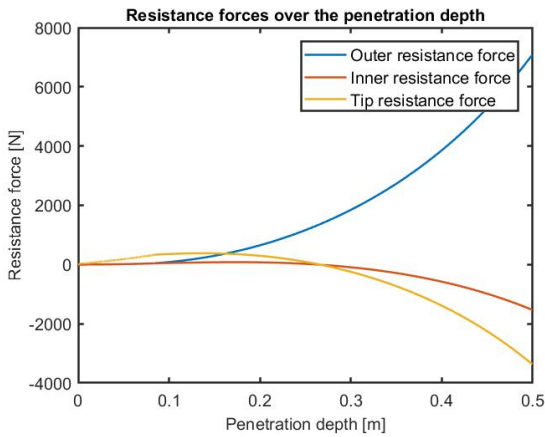


Figure 13: Friction Forces Redhill [SC]

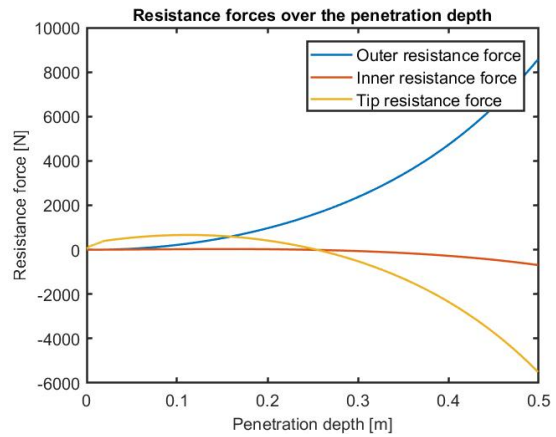


Figure 14: Friction Forces Luce Bay [SC]

Several insights can be obtained from these plots. In the line of the tip resistance, one can observe that the first part of the line is a somewhat more linear line than the later part of the line. Exactly this part "linear" part is the friction in the self-weight penetration phase. The self-weight penetration depths are shown in table 12.

Soil type	Self-Weight Penetration Depth [m]
Statoil Sand	0.0246
Silica Sand	0.1087
Redhill Sand	0.0834
Luce Bay Sand	0.0192

Table 12: Self-Weight Penetration Depths for the Single Caisson case.

From the plots it can also be observed that the frictional forces at the inside of the caisson and at the tips is at a certain point tending to drop. The meaning of the two frictional forces to drop is that the piping phenomenon occurs. The point where the suction caisson will no longer penetrate the soil, is the point where the applied suction is larger than the critical suction. Therefore, the suction plots are observed to see what the maximum penetration depth is of the caissons. The suction plots are shown in figure 15 up to 18.

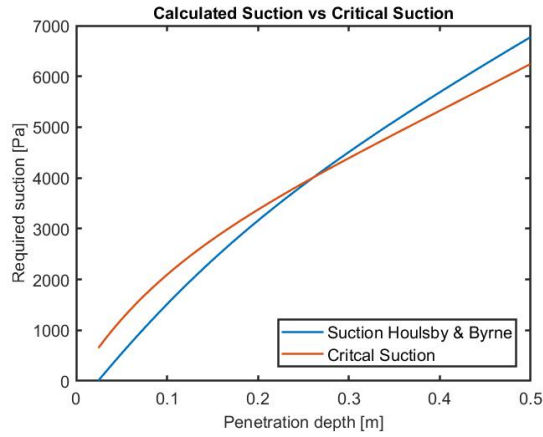


Figure 15: Required Suction Statoil [SC]

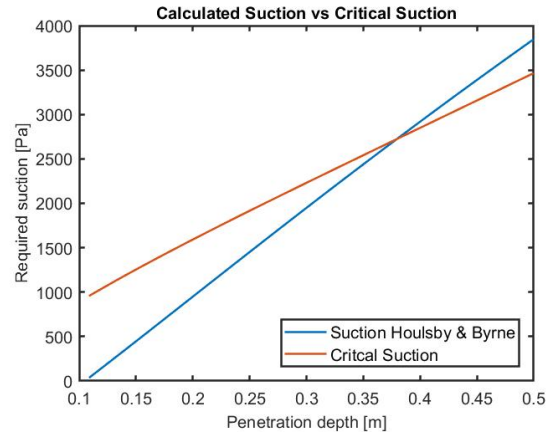


Figure 16: Required Suction Silica [SC]

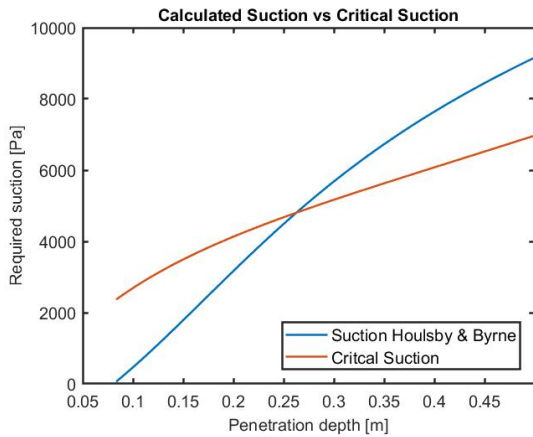


Figure 17: Required Suction Redhill [SC]

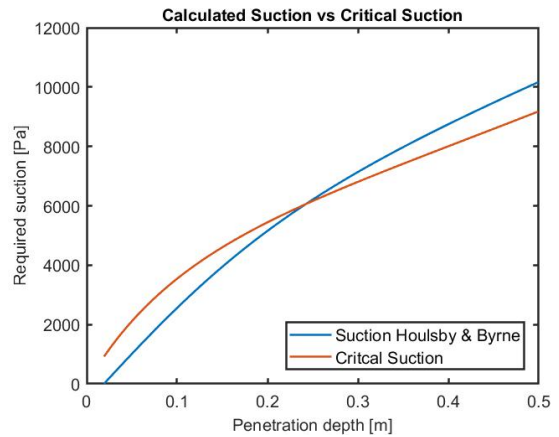


Figure 18: Required Suction Luce Bay [SC]

From these plots it can be observed that in three of the four cases, the maximum penetration depth lies between 0.23 and 0.3 meter. Only the silica sand soil enables a larger penetration depth. None of the single suction caissons are able to penetrate the seabed fully. In order for the suction caissons to be fully deployed, the dimensions of the suction caissons can be altered in order to let them be fully installed. The maximum penetration depths are shown in table 13.

Soil type	Maximum Penetration Depth [m]
Statoil Sand	0.2611
Silica Sand	0.3795
Redhill Sand	0.2627
Luce Bay Sand	0.2422

Table 13: Maximum Penetration Depths for the Single Caisson case.

To be able to see to what extent the suction caisson is able to withstand pull out loads, the holding capacity can be calculated. These holding capacities depend on the penetration depth of the caisson, which makes it possible to plot the holding capacity over the penetration depth. The holding capacity plots are shown in figure 19 up to 22.

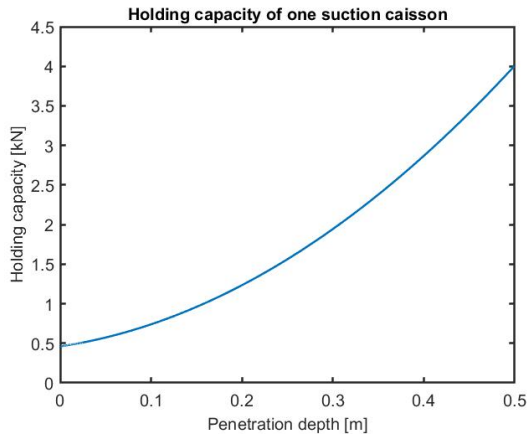


Figure 19: Holding Capacity Statoil [SC]

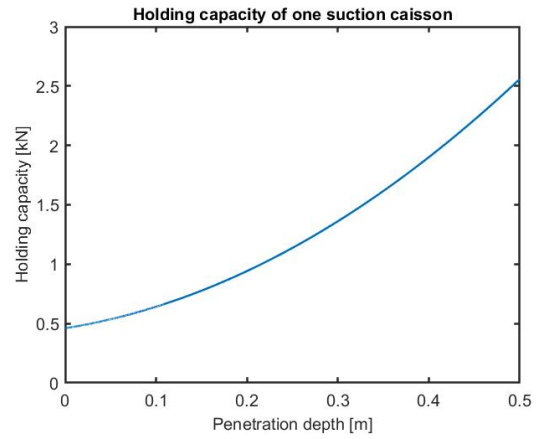


Figure 20: Holding Capacity Silica [SC]

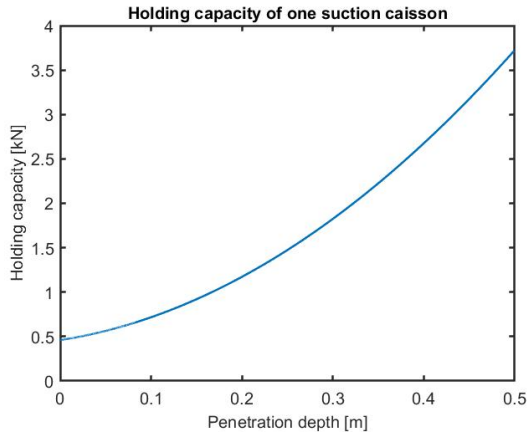


Figure 21: Holding Capacity Redhill [SC]

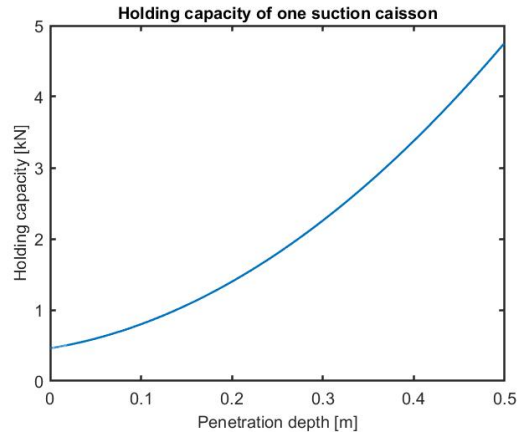


Figure 22: Holding Capacity Luce Bay [SC]

Looking at the plots, the quadratic relationship between the holding capacity and the penetration depth is clearly visible. The type of soil influences the final value of the holding capacity of the circular caissons.

7.1.1.2 The full system

For the full system the same plots are given, as was done for the previous case (single suction caisson). However, within this model several additional parts of the Ocean Battery foundation are added. In the case of the full system, all the relevant plating is taken into account, as well as the reservoir that rests on top of the system. All of these added parts are modelled through corresponding forces to the system. As mentioned previously in section 7.1, this main case is divided in three sub cases. These three sub cases will each be explained in this section.

The four chamber model

The four chamber model is built to see the behaviour when only the four circular suction caissons are activated. For this case the same plots can be obtained as was found for the single caisson system. The first plots obtained are the friction force plots, which are shown in figure 24 up to 27. The sequence of activation is schematically shown in figure 23. The numbers in this figure represent the order in which the caissons are activated. For the four chamber model, only the four corner caissons are used and activated simultaneously.

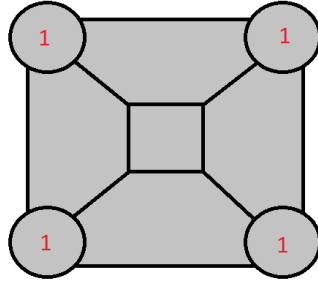


Figure 23: Activation sequence for the four chamber model.

What can be seen from these friction force plots is that the first phase (the self-weight penetration) is considerably deeper than for the single caisson. This is due to the fact that the caissons now each carry one fourth of the total system its weight, whereas for the single caisson case they only were subjected to their own weight. From the plots it can be observed that the all the soils will be subjected to piping, as the forces at the tips and the inside of the caisson are decreasing. However, as the forces of the inside and tips are not dropping below zero for the silica soil, the system is able to be fully installed. Besides the installation, one can see the influence of the plates in the plot for silica sand, as there is a drop for the inside and outside friction and an increase for the tip friction force.

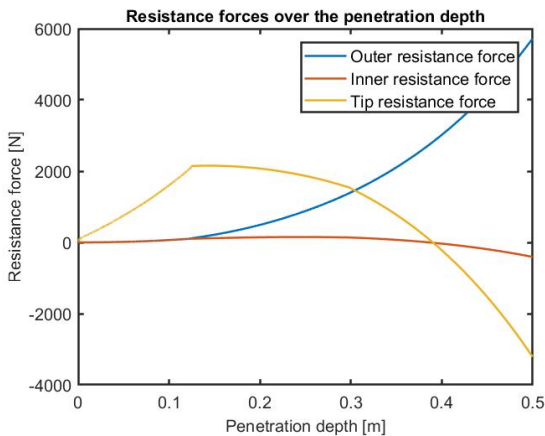


Figure 24: Friction Forces Statoil [FS4]

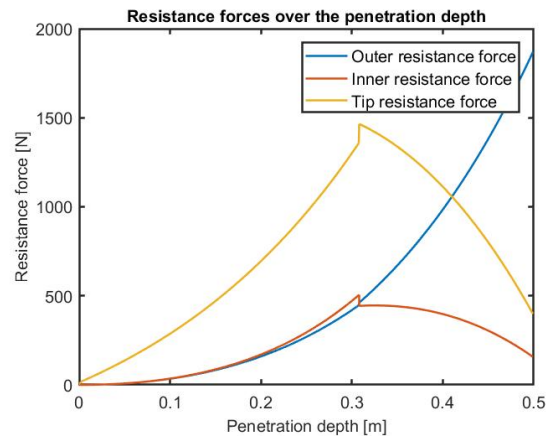


Figure 25: Friction Forces Silica [FS4]

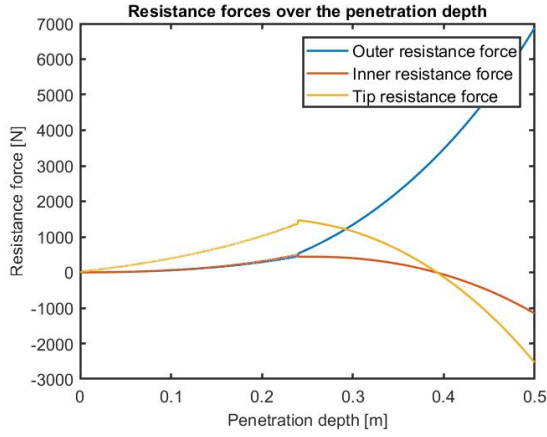


Figure 26: Friction Forces Redhill [FS4]

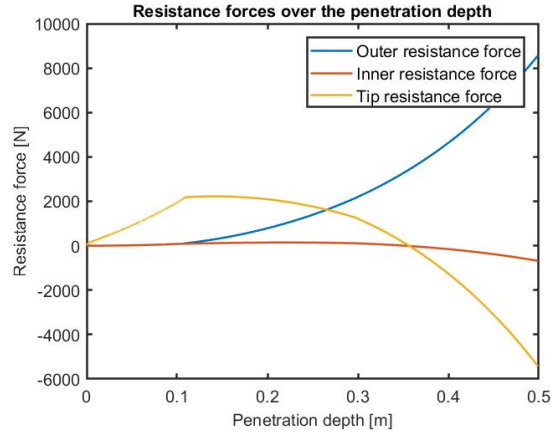


Figure 27: Friction Forces Luce Bay [FS4]

From the plots, the different self-weight penetration values can be obtained. The self-weight penetration phase ends at the point where the values of the tip friction forces and the inner friction forces start to decrease. Table 14 show the different values for the self-weight penetration depth obtained for the four different soils. The table shows that the highest self-weight penetration depth is obtained in the silica sand.

Soil type	Self-Weight Penetration Depth [m]
Statoil Sand	0.1247
Silica Sand	0.3080
Redhill Sand	0.2397
Luce Bay Sand	0.1081

Table 14: Self-Weight Penetration Depths for the Full System case.

Using the plots for the required suction vs the critical suction, it can be determined what the maximum penetration holds. When the calculated suction is larger than the critical suction, the piping will prevent the system from penetrating the seabed any further. The required suction plots are shown in figure 28 up to figure 31.

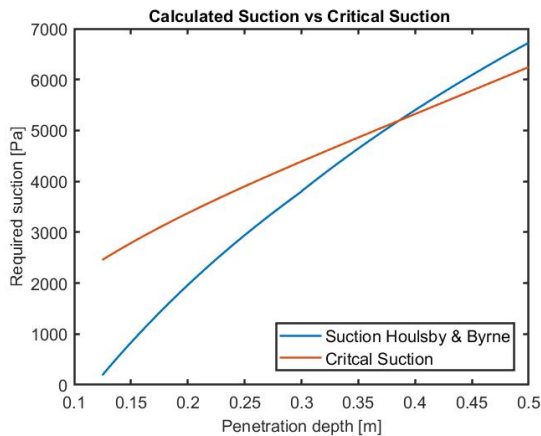


Figure 28: Required Suction Statoil [FS4]

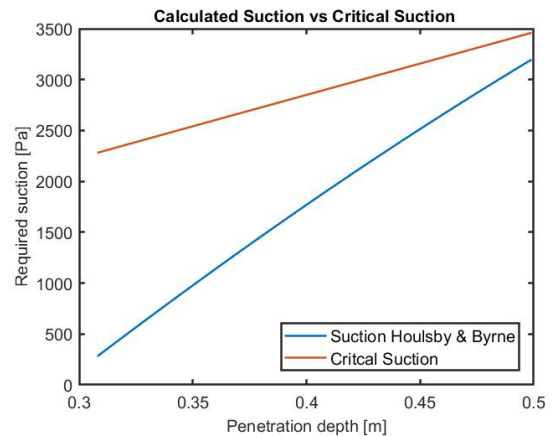


Figure 29: Required Suction Silica [FS4]

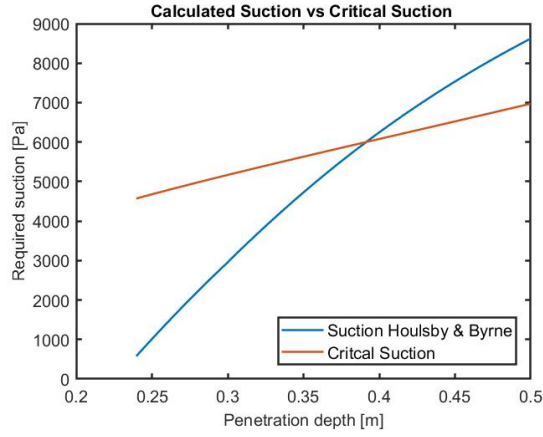


Figure 30: Required Suction Redhill [FS4]

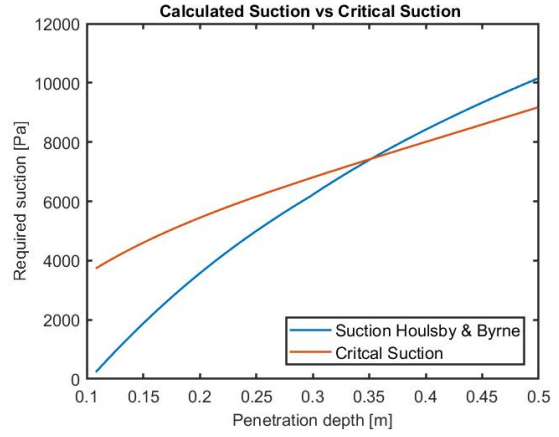


Figure 31: Required Suction Luce Bay [FS4]

From the required suction plots, it can be observed that the system can be fully deployed in the silica sand soil, whereas the other soils prevent the complete system to fully install. In table 15 the maximum penetrations of the full system in the four soils is shown.

Soil type	Maximum Penetration Depth [m]
Statoil Sand	0.3857
Silica Sand	0.5
Redhill Sand	0.3914
Luce Bay Sand	0.3520

Table 15: Maximum Penetration Depths for the Full System case with 4 chambers.

The holding capacity of the round caissons used within the system the holding capacity per suction caisson is plotted. These plots are shown in figure 32 up to figure 35. The holding capacity shows to which extend a suction caisson can withstand forces that will "pull out" the suction caisson.

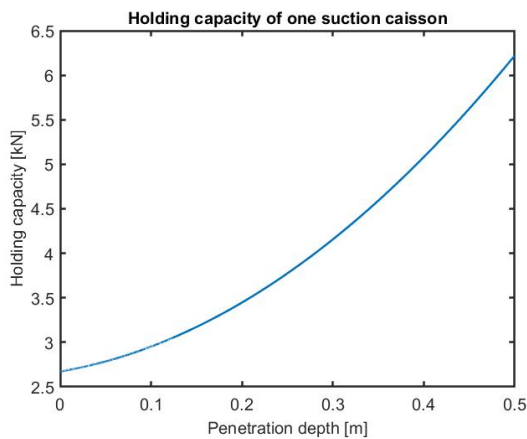


Figure 32: Holding Capacity Statoil [FS4]

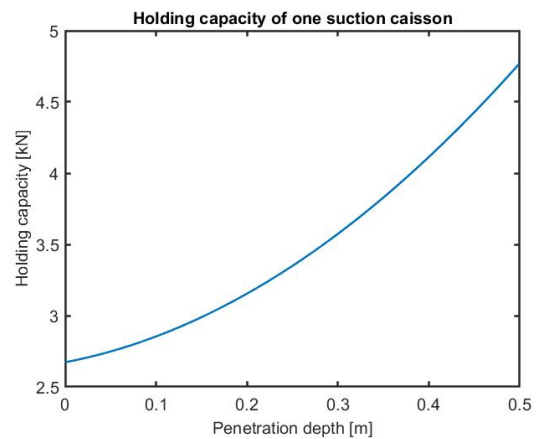


Figure 33: Holding Capacity Silica [FS4]

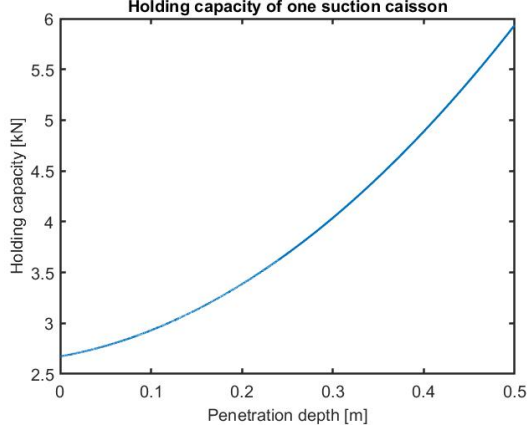


Figure 34: Holding Capacity Redhill [FS4]

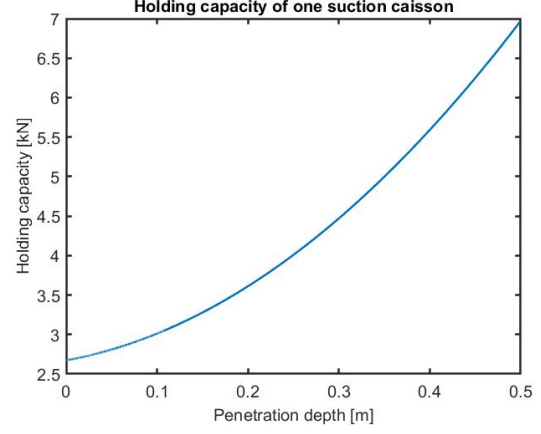


Figure 35: Holding Capacity Luce Bay [FS4]

From the holding capacity plots, one can clearly observe the quadratic response to the penetration depth.

The five chamber model

In the case where five chambers of the system are active, the square in the middle of the foundation will act as a suction chamber. The chamber will be activated when the required suction of the four circular becomes larger than the critical suction. As the four chamber model showed that the system is able to be fully deployed in silica sand, this type of soil will not be used in the five chamber model, as additional caissons are not needed.

The sequence of activation of the different caissons is schematically represented in figure 36 for the five chambered model. The numbers in the figure correspond with the sequence of activation. In the five chambered model, the four circular caissons are activated first. When the suction of the four caissons exceeds the critical suction, the square caisson in the middle of the foundation is activated.

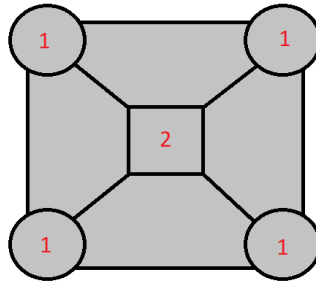


Figure 36: Activation sequence for the five chamber model.

The first plots obtained are the friction forces plots. Note that these frictional forces are the forces that act around the circular suction caissons. The frictional forces for the five chamber model are shown in figure 37 up to 39. As the system itself is the same as in the four chamber model, the self-weight penetration depths remain the same. The difference between the models lies in the second phase of the installation, namely the suction assisted phase.

From the friction force plots it can be observed that indeed the fifth suction caisson is turned on when the required suction will become larger than the critical suction. This results in a vertical jump in the values of the frictional forces. At this jump, the fifth caisson is turned on and the system can penetrate the soil further which leads to an increase in frictional forces.

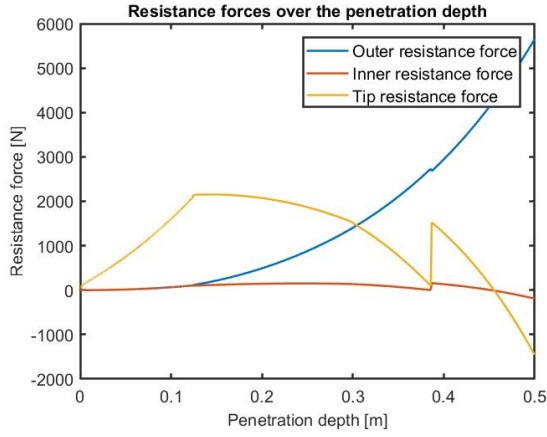


Figure 37: Friction Forces Statoil [FS5]

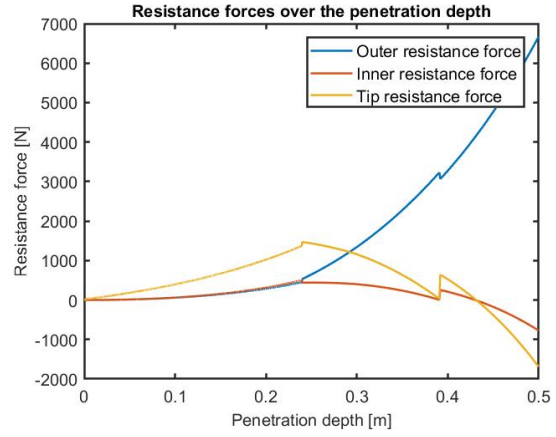


Figure 38: Friction Forces Redhill [FS5]

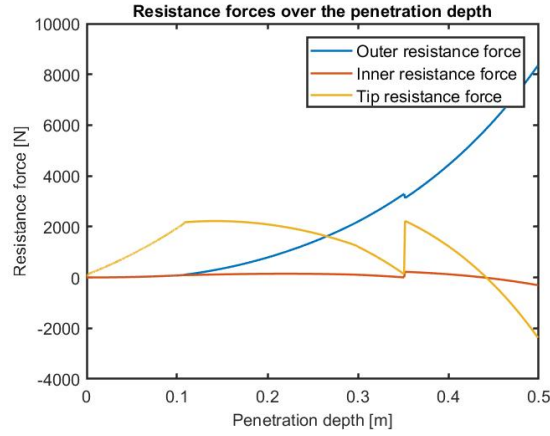


Figure 39: Friction Forces Luce Bay [FS5]

Although the system can penetrate the soil further than with only four caissons activated, still the piping phenomenon will take place as the frictional forces, at the inside and the tips, again tend to become negative. To be able to see the maximum penetration depth, the required suction vs critical suction plots can be investigated. These plots are shown in figure 40 up to 42.

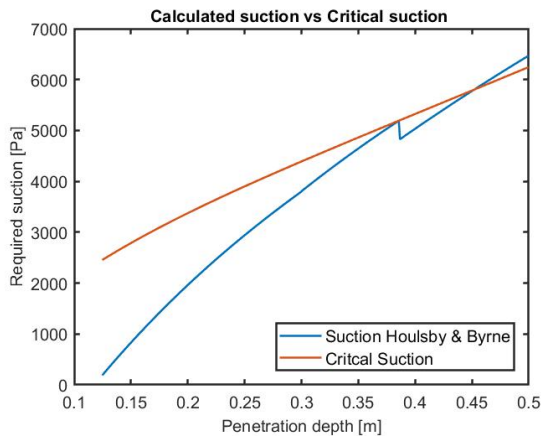


Figure 40: Required Suction Statoil [FS5]

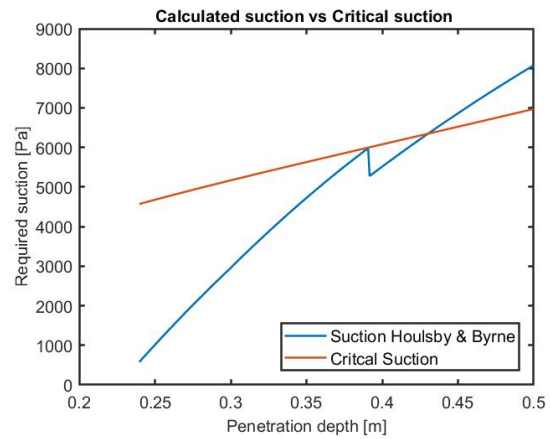


Figure 41: Required Suction Redhill [FS5]

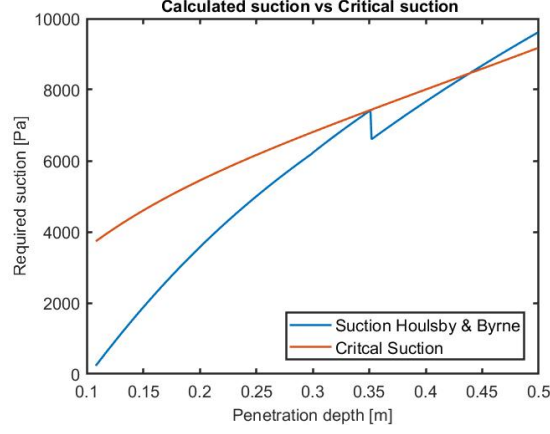


Figure 42: Required Suction Luce Bay [FS5]

From the required suction plots, the maximum penetration depth can be obtained. These penetration depths are shown in table 16. What can be seen from the table, is that the system is able to almost fully be deployed as the maximum penetration depths are close to 0.5 meter.

Soil type	Maximum Penetration Depth [m]
Statoil Sand	0.4518
Redhill Sand	0.4302
Luce Bay Sand	0.4386

Table 16: Maximum Penetration Depths for the Full System case with 5 chambers.

For this model, the holding capacities can be plotted over the penetration depth. In this case there are two lines, of which one indicates the holding capacity of a circular caisson and one line denotes the holding capacity of the square caisson. The holding capacity plots are shown in figure 43 up to 45.

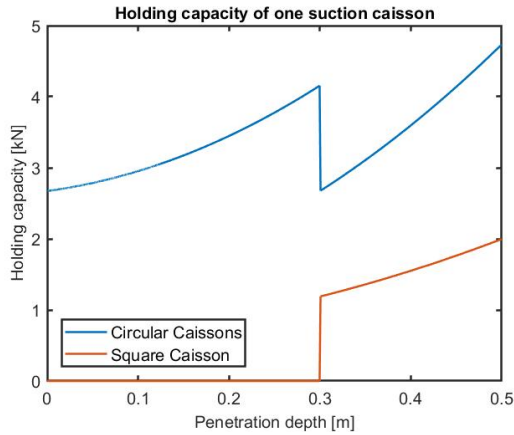


Figure 43: Holding Capacity Statoil [FS5]

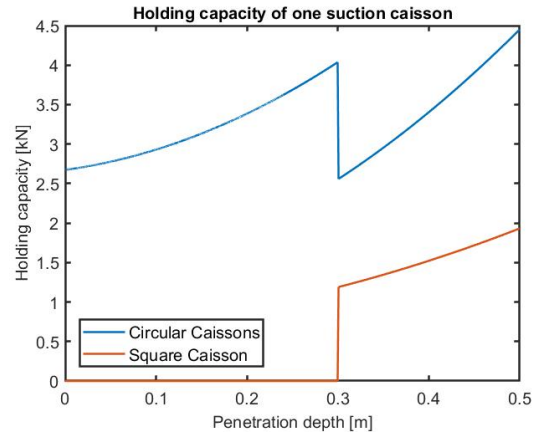


Figure 44: Holding Capacity Redhill [FS5]

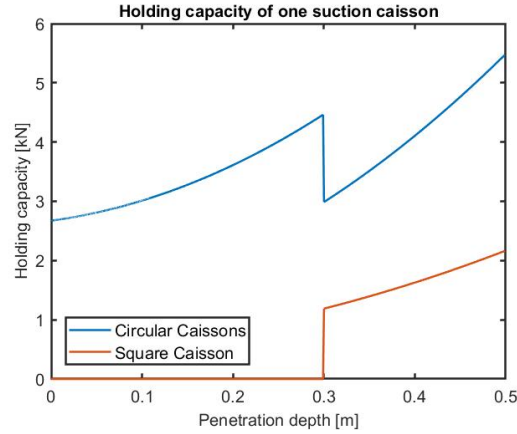


Figure 45: Holding Capacity Luce Bay [FS5]

In the plots, the holding capacity shows the quadratic behaviour of the holding capacity with respect to the penetration depth. Although the square caisson will be activated later than the moment it reaches the seabed, when the caisson is penetrating the seabed (without suction) it creates a holding capacity as the holding capacity does not depend on the suction. This also holds for the trapezoidal caissons. However, for each case of activated models, the caissons are plotted that are active. In the five chamber model this means that the square and cylindrical caissons are plotted.

The drop in the holding capacity of the cylindrical caisson is caused by the shift in the distribution of the weight of the system. When only the four cylindrical caissons are penetrating the soil, each of the caissons account for a quarter of the weight of the total system. When the square and trapezoidal caissons start penetrating the soil, each of the caissons accounts for one ninth of the total systems weight.

The nine chamber model

As can be seen from the plots of the five chamber model, the system cannot penetrate the seabed completely for the three soils (silica sand proved to penetrate the seabed with four chambers). In this nine chamber model, the spaces in the trapezoidal parts of the foundation are used as suction caissons. As was shown in the previous models, the first plots are the friction force plots. These plots are shown in figure 47 up to 49.

Figure 46 shows the sequence of activation of chambers for the nine chamber model. First the circular caissons at the corners are activated simultaneously. When the required suction exceeds the critical suction, the square caisson in the middle will activate. When again the required suction of the combination of caissons exceeds the critical suction, the four trapezoidal caissons will be activated simultaneously.

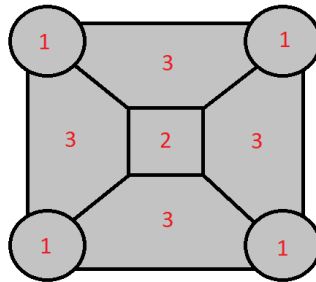


Figure 46: Activation sequence for the nine chamber model.

From these friction force plots it can be observed that the system can be fully deployed in the three soils when all nine chambers are activated. The plots show that there is room for a deeper penetration if necessary. For this system the limit lies at 0.5 meters, as the height of the design is 0.5 meter high. The same jumps are observed in these friction forces, as were shown in the five chamber model. However, with this model there is an additional jump that is observed when the trapezoidal chambers are activated.

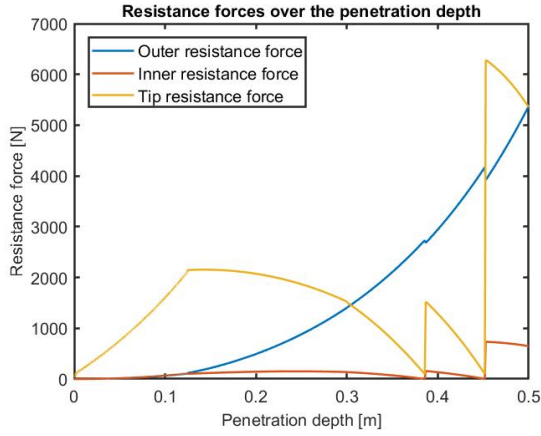


Figure 47: Friction Forces Statoil [FS9]

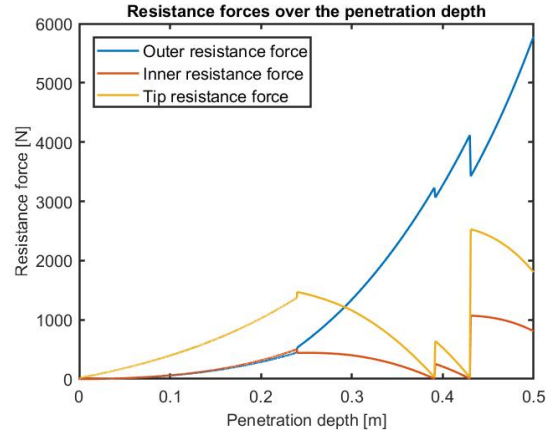


Figure 48: Friction Forces Redhill [FS9]

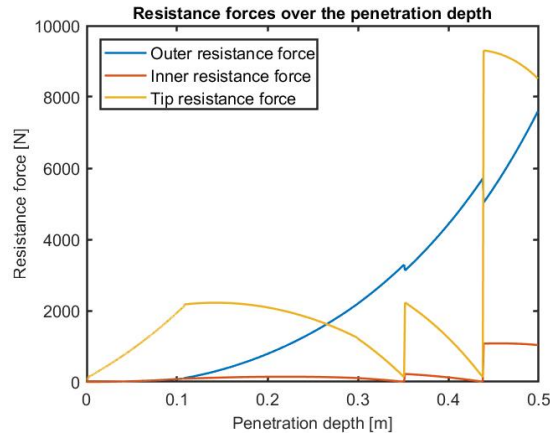


Figure 49: Friction Forces Luce Bay [FS9]

The required suction vs critical suction all show that the system can be fully installed in the seabed. As the friction forces plots showed as well, the suction plots show that there is room for further penetration if necessary. The required suction vs critical suction plots are shown in figure 50 up to 52. From the plots the activation of the trapezoidal and square caissons is clearly visible. The plots show that for the system has the ability to penetrate the soil further if it is necessary, which is especially the case for the Redhill sand.

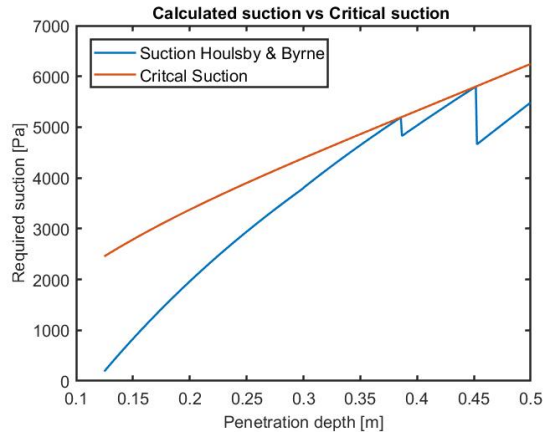


Figure 50: Required Suction Statoil [FS9]

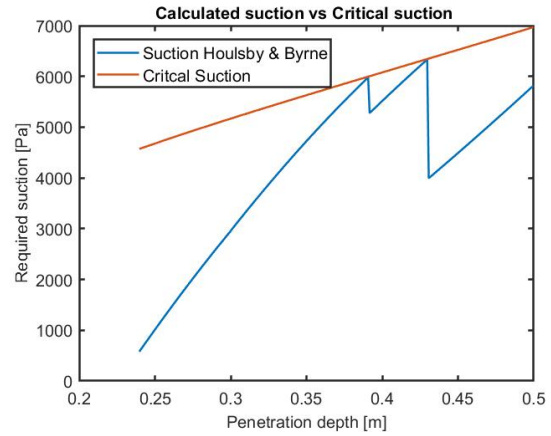


Figure 51: Required Suction Redhill [FS9]

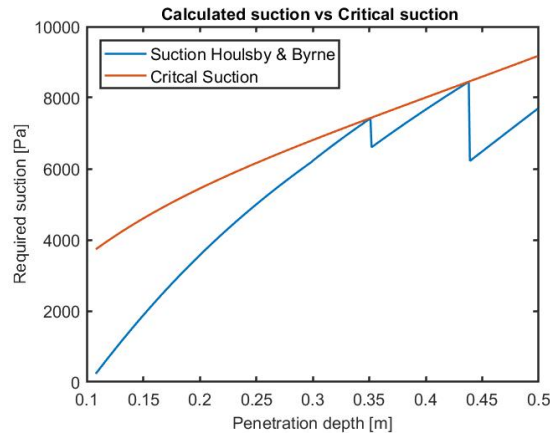


Figure 52: Required Suction Luce Bay [FS9]

The holding capacities of the different chambers is shown in figure 53 up to 55. As was explained for the case with 5 chambers, the trapezoidal and square caisson form a holding capacity starting at 0.3 meters in depth, as the holding capacity does not depend on the suction. The drop in the holding capacity for the cylindrical caissons is again caused by the change in distribution of weight, which corresponds to the number of chambers activated.

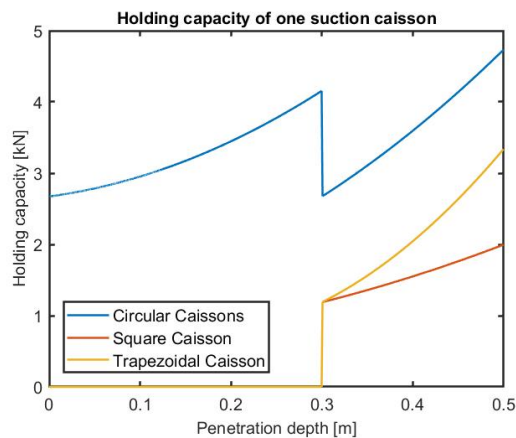


Figure 53: Holding Capacity Statoil [FS9]

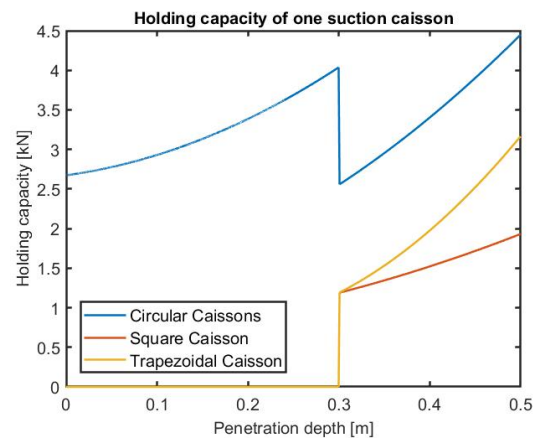


Figure 54: Holding Capacity Redhill [FS9]

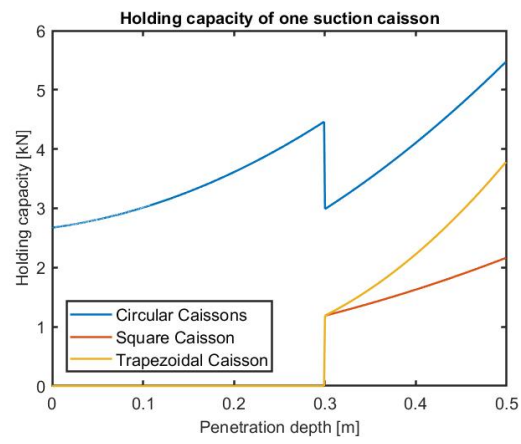


Figure 55: Holding Capacity Luce Bay [FS9]

7.1.2 Cohesive Soil Results

This section shows the results obtained from the MATLAB code for the cohesive soil case. The results are described for all cases and subcases, each in a corresponding section. The single caisson case will be discussed first after which the full system cases are discussed.

7.1.2.1 The single caisson model

This case shows how the single caisson is behaving in cohesive soils and what the relation is between this behaviour and the penetration depth. The first set of plots for the cohesive soils is set of plots with the frictional forces which are acting on the suction caisson. These plots are shown in figure 56 up to 58.

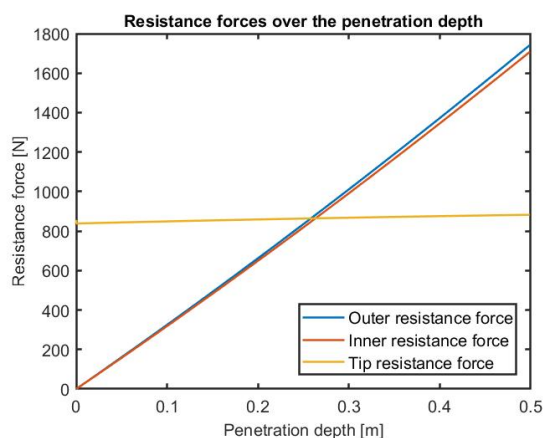


Figure 56: Friction Forces Kaolin [SC]

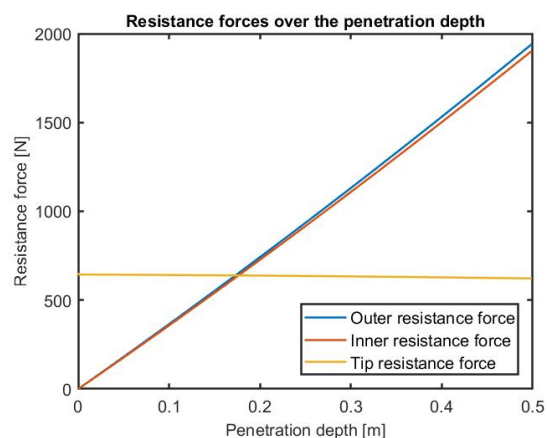


Figure 57: Friction Forces Nkossa [SC]

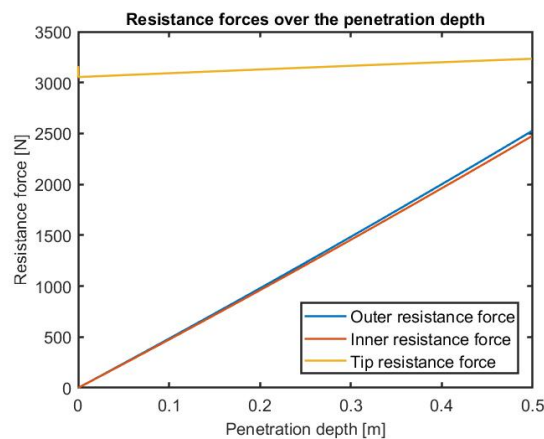


Figure 58: Friction Forces Qiantang [SC]

From the plots, it can be observed that the friction forces are rather different than the frictional forces in the cohesionless soil case. It can be observed that the relation of the frictional terms with respect to the penetration depth is a linear relationship. Another observation is that the friction force at the tip of the caisson is rather stable in comparison with the resistances on the inside and outside in the case of cohesive soils. Where the two clay soils, Kaolin and Nkossa, are behaving rather similarly, the silt soil is behaving different. For the Qiantang silt the friction forces at the top are rather high in comparison with the inside and outside friction forces.

The plots for the required suction are shown in figure 59 up to 61. From these plots the suction can be observed, but also the maximum penetration of the system can be seen.

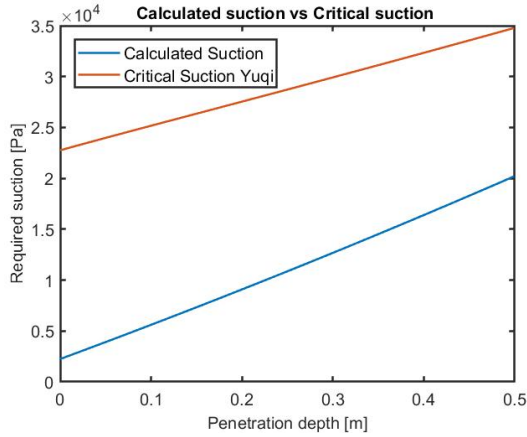


Figure 59: Required Suction Kaolin [SC]

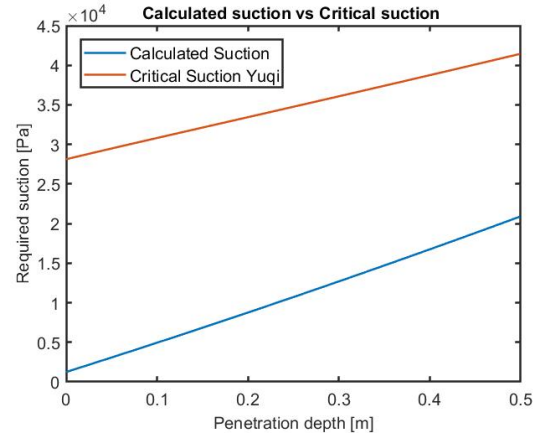


Figure 60: Required Suction Nkossa [SC]

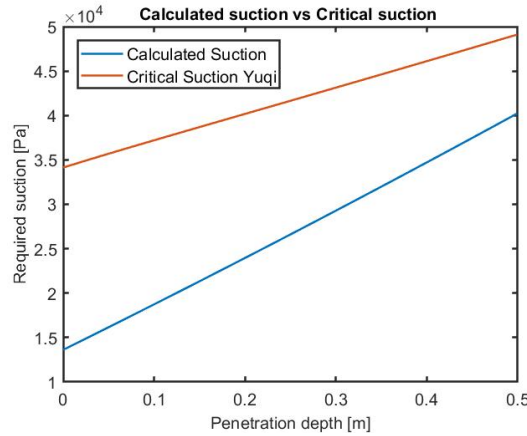


Figure 61: Required Suction Qiantang [SC]

From the required suction plots, it is observed that in all the soil cases the critical suction is not met. This means that the suction caissons are able to fully penetrate the seabed. Another remarkable observation is that the magnitude of the required suction for the cohesive soils is significantly higher than for the cohesionless soils.

The plots for the holding capacity are shown in figure 62 up to 64. As the required suction plots showed that the circular suction caissons are able to be fully installed, the holding capacity is maximized for this case. From the holding capacity plots, the linear relationship with the penetration depth can be clearly observed. The influence of the different soil types is observed in these plots as well. The Qiantang river silt provides the highest holding capacity with a value around 11.4 kN.

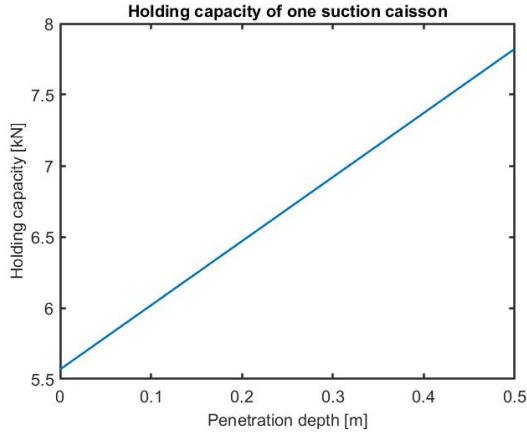


Figure 62: Holding Capacity Kaolin [SC]

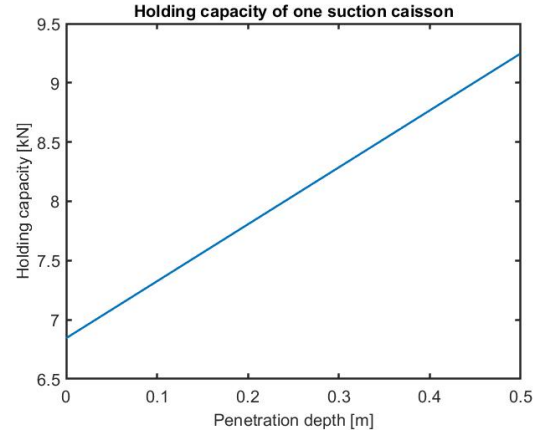


Figure 63: Holding Capacity Nkossa [SC]

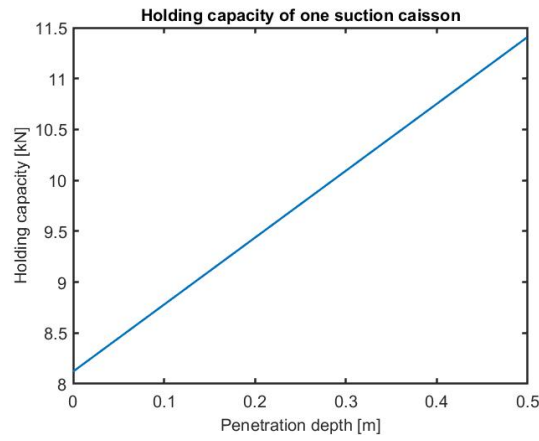


Figure 64: Holding Capacity Qiantang [SC]

7.1.2.2 The full system

The four chamber model

The first plots given for the four chamber model are, as in the previous cases, the three friction forces plots. The frictional plots are shown in figure 66 up to 68. The sequence of activation of chambers is the same as in the four chamber model for the cohesionless soil case and shown in figure 65. In this case only the four circular caissons are simultaneously.

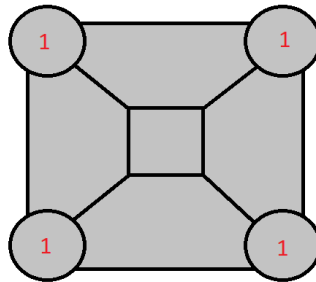


Figure 65: Activation sequence for the four chamber model.

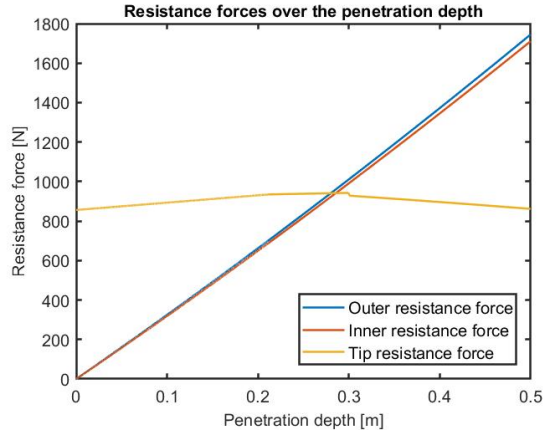


Figure 66: Friction Forces Kaolin [FS4]

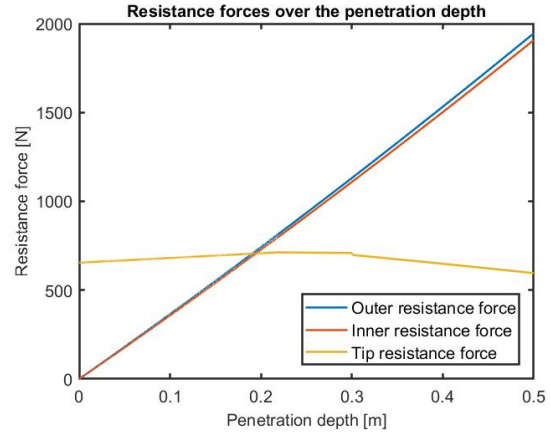


Figure 67: Friction Forces Nkossa [FS4]

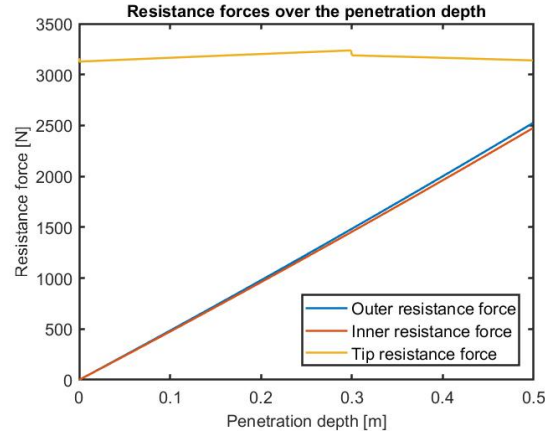


Figure 68: Friction Forces Qiantang [FS4]

Within these plots, the influence of the skirts of the foundation can be observed. When the skirts enter the seabed, a jump in the frictional forces can be detected. From the plots it can be seen that both the Kaolin clay and Nkossa clay behave similarly. However, for the Qiantang River silt, the tip resistance forces are significantly higher than the other two friction forces. This indicates, together with the fact that the magnitude of the tip friction forces is significantly higher, that a silt soil is harder to penetrate than clay type of soils. The self-weight penetration depths of the system in the three different soils is given in table 17. From this table, it can be seen that the Qiantang River silt prevents the system from penetrating through its own weight.

Soil type	Self-Weight Penetration Depth [m]
Kaolin Clay	0.2116
Nkossa Clay	0.2188
Qiantang Silt	0.0000

Table 17: Self-Weight Penetration Depths for the Full System case.

The required suction vs the critical suction plots, for the four chamber system, are given in figure 69 up to 71.

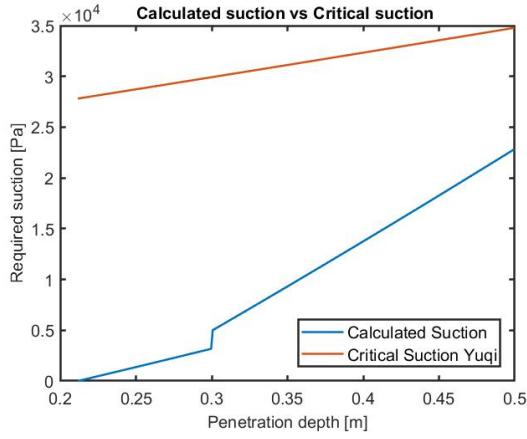


Figure 69: Required Suction Kaolin [FS4]

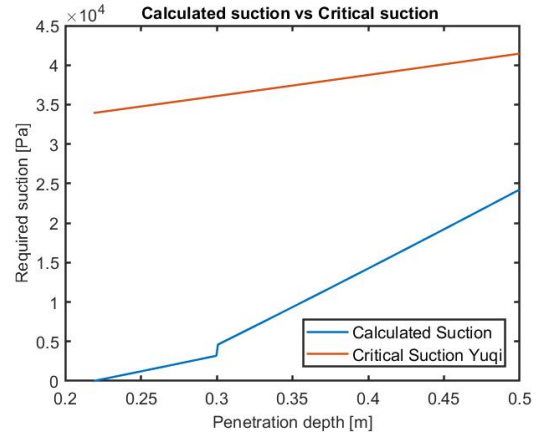


Figure 70: Required Suction Nkossa [FS4]

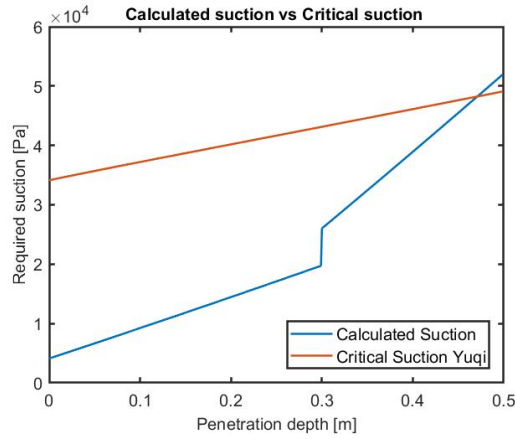


Figure 71: Required Suction Qiantang [FS4]

From these plots it can be observed that the Qiantang River silt prevents the system from a full installation. The maximum penetration that is reached for this soil type is given in table 18. As was observed in the single caisson case, the magnitude of the required suction is significantly higher than for cohesionless soils.

Soil type	Maximum Penetration Depth [m]
Qiantang	0.4708

Table 18: Maximum Penetration Depths for the Full System case in Qiantang River Silt.

The holding capacities of the suction caisson are given in figures 72 up to 74. In these plots, the linear dependency on the penetration depth can, again, be observed. Although the four chamber system cannot be fully deployed in the Qiantang silt, the holding capacity is for this maximum penetration higher than for the two clay soils.

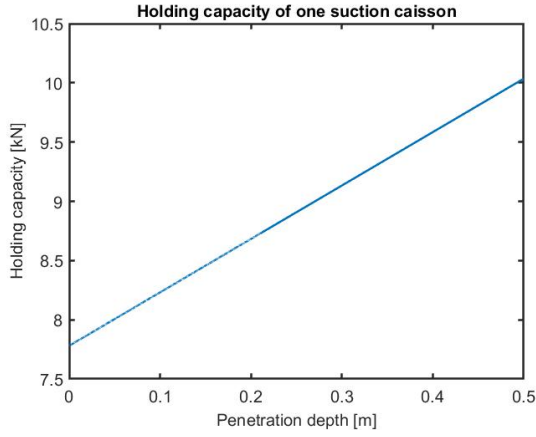


Figure 72: Holding Capacity Kaolin [FS4]

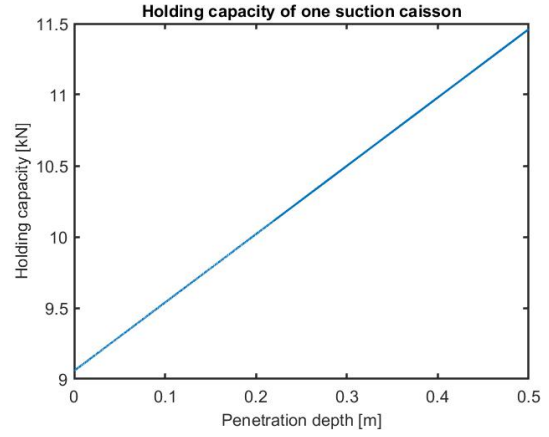


Figure 73: Holding Capacity Nkossa [FS4]

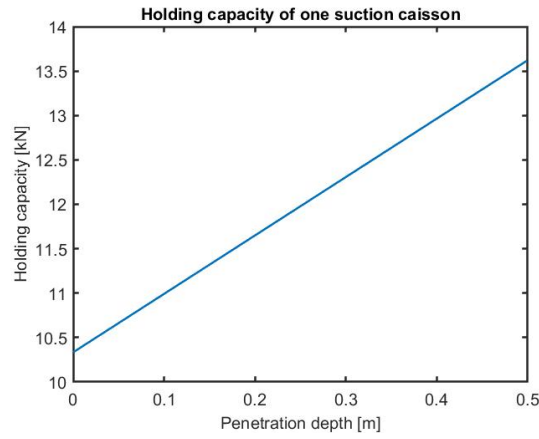


Figure 74: Holding Capacity Qiantang [FS4]

The five chamber model

As was observed in the four chamber model for the cohesive soils, the system is not able to fully install in the Qiantang River silt. Therefore, this soil type is investigated for the 5 chamber model. As only one soil type has to be investigated for the 5 chamber model, the plots are given all together for this model. figure 76 up to 78 show the friction forces, required suction vs critical suction and the holding capacity for the 5 chamber model in Qiantang River silt. The sequence of activating is shown in figure 75 for the five chamber model. First the four cylindrical caissons are activated simultaneously. When the required suction exceeds the critical suction, the square caisson in the middle of the foundation is activated.

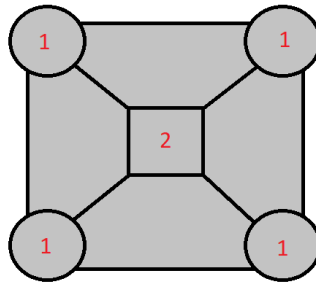


Figure 75: Activation sequence for the five chamber model.

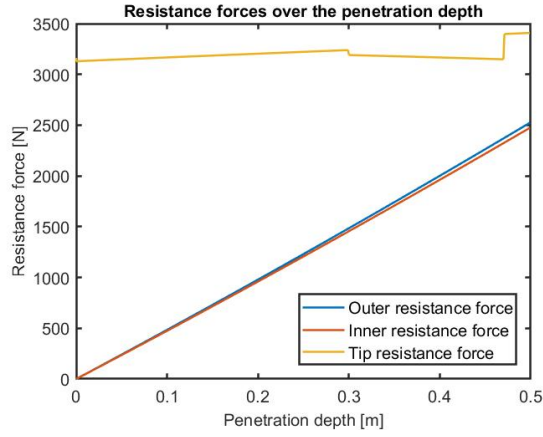


Figure 76: Friction Forces Qiantang [FS9]

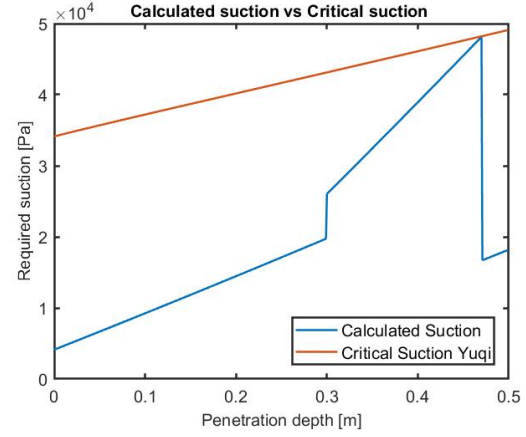


Figure 77: Required Suction Qiantang [FS9]

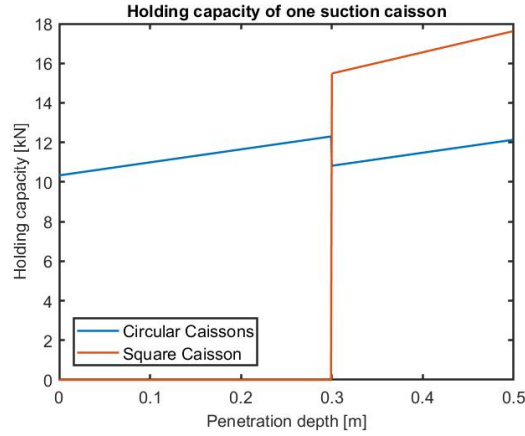


Figure 78: Holding Capacity Qiantang [FS9]

From these plots it is found that the system is able to be fully installed in the Qiantang River silt with the use of 5 suction caissons. In the frictional forces and suction plot, the activation of the square suction caisson is visible. From the required suction vs critical suction plot, it is observed that the square caisson has a large impact on the suction that is required. In the holding capacity, it can be observed that there is a drop in the holding capacity of the cylindrical caissons. This drop is caused by the same shift in the weight distribution that was mentioned for the cohesionless cases. When only the cylindrical caissons are penetrating the soil, each of the caissons accounts for a quarter of the total weight of the system. When the other caissons start penetrating the soil, each caisson accounts for one ninth of the total weight of the system.

7.1.3 Prediction Prototype 1 Results

With the models obtained for the full system and single caisson, it is possible to obtain a prediction for the existing prototype of the Ocean Grazer group. This prototype consists of a single caisson with a housing on top of it, which is produced by the company Eizinga. A isometric view of the design is shown in figure 79.

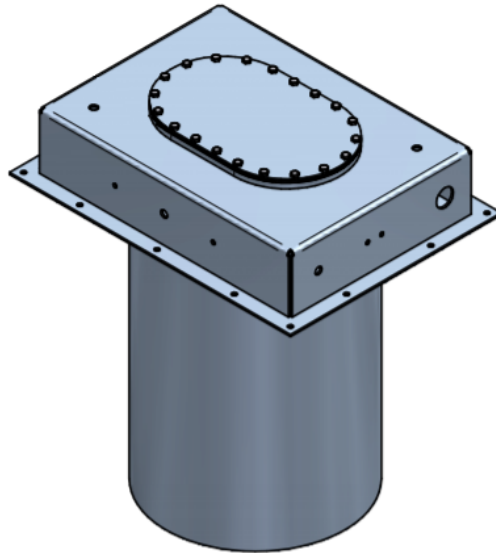


Figure 79: Existing prototype of the Ocean Grazer

The design shown will be the first prototype which will be installed and tested on location (Harbor of the Eemshaven). The CTO (M. van Rooij, MSc) of the Ocean Grazer company tested the soil on the location. This was done by using multiple connected tubes of PVC, forming one large tube, that was pushed in the soil figure 81. The tube is afterwards filled with water to prevent the soil from leaving the tube. It was found that the soil proved to be a type of harbor mud (figure 80).



Figure 80: Soil type that was found during testing on location (64)



Figure 81: The testing PVC tube set used during location tests (64)

From this test, it can be concluded that the soil within the harbor of the Eemshaven is a cohesive type of soil. As the exact composition of the Eemshaven soil is difficult to determine, the prediction is done for all three soil types. For the prediction of the first prototype, the

required suction vs critical suction plot is the most important outcome. This plot shows if the prototype can be fully installed or not. Figures 82 up to 84 show the suction plots for the three cohesive soil cases. Figure 85 shows the case when the first prototype would be installed in statoil sand. This plot is shown to be able to compare the situations for the first prototype.

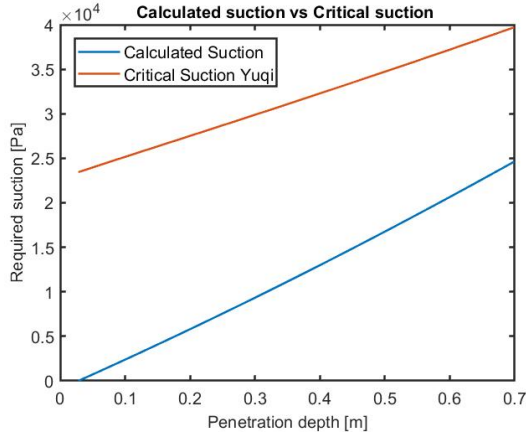


Figure 82: Prototype 1 suction Kaolin clay

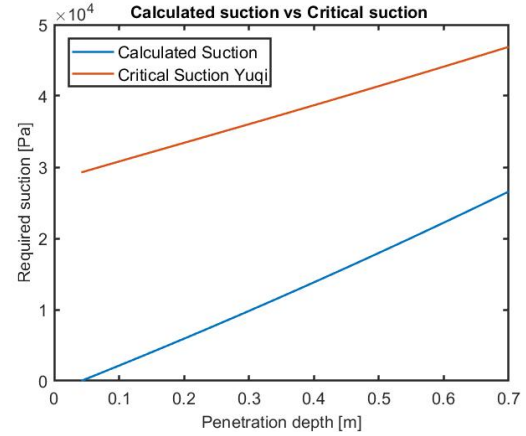


Figure 83: Prototype 1 suction Nkossa clay

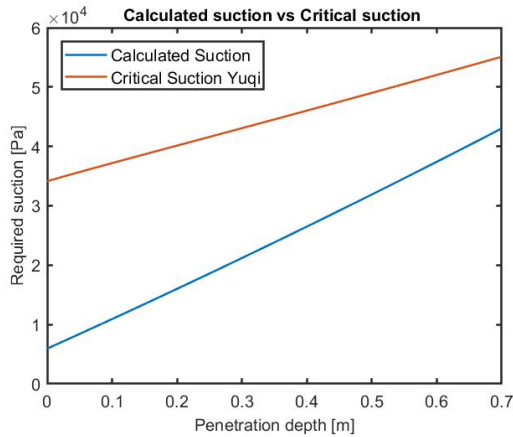


Figure 84: Prototype 1 suction Qiantang silt

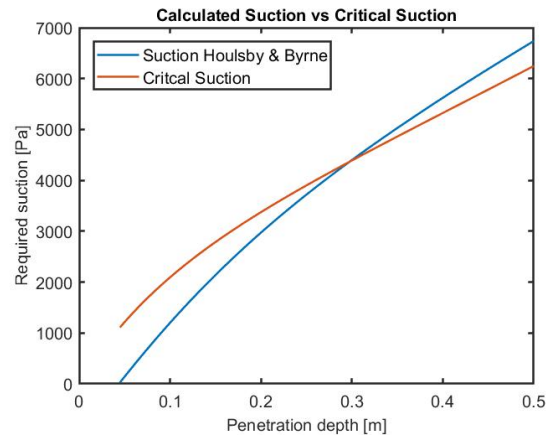


Figure 85: Prototype 1 suction Statoil sand

The first three plots show that the prototype can be installed in each of the three cohesive soils. The last plot (figure 85) shows the behaviour of the first prototype in a cohesionless soil. It can be observed that the behavior is different for the two categories of soils and the prototype cannot be fully installed in the statoil sand. The maximum penetration depth possible for the prototype in this case is 0.2974 meter.

7.2 COMSOL Results

The results of the COMSOL Multiphysics software are discussed in this chapter and show insights in the structural integrity of the design. The MATLAB model provides several of the values that can be plugged into the COMSOL model, such as suction variables and frictional variables. The COMSOL results are divided into two main cases and three sub cases (as was done for the MATLAB model). The cases are the following:

1. The single caisson model.
2. The full system model
 - (a) Four chamber model.
 - (b) Five chamber model.
 - (c) Nine chamber model.

As was done previously, the sub cases are the cases where the 5 middle compartments are used as suction caissons as well. This can be done when the required suction exceeds the critical suction. The results are splitted into two sections, one for the cohesionless soils and one for the cohesive soils (sections 7.2.1 and 7.2.2).

In the COMSOL model cases, several additional parameters have to be taken into account. Within a software package. Conditions that have to be taken into account is the accuracy of the model but also the complexity of the model. One can decide to make the model very complex, but when the model is computed it can take long amounts of time and can be not as accurate as one would want. However, the opposite is also possible. A highly accurate model can take a large amount of time to be computed. Therefore there should be an optimum in the accuracy that is needed and the complexity that is added.

The complexity can be reduced by stating several assumptions and making the model more simple. The accuracy can be increased or decreased by defining the mesh of the COMSOL model. Especially the mesh will be discussed in the results in the result sections 7.2.1 and 7.2.2. Table 19 shows the different settings for both the model and material.

Model settings	
Physics used	Solid Mechanics
Element type	Quadratic serendipity
Solver type	Stationary solver
Solver	MUMPS solver
Material properties	
Structural Steel	
Density (ρ)	7850 $[kg/m^3]$
Youngs Modulus (E)	200 $[GPa]$
Poisson ratio (ν)	0.30 $[-]$

Table 19: Model and Material settings in the COMSOL models.

7.2.1 Cohesionless Soil Results

7.2.1.1 The single caisson model

The first case considered in the COMSOL model is the single caisson case for the cohesionless (sand type) soils. The forces and suction values are obtained through the MATLAB script and used within the COMSOL model. Besides the forces and required suction, the model in COMSOL should contain variables to deal with the environment.

The prototype of the Ocean Battery should be able to be deployed to a depth of 10 meters. Therefore, the hydrostatic pressure can be calculated for a depth of 10 meters, which acts on the top and side of the structure. The structure is fixed on the line that is corresponding to the level of the seabed. When the complete areas are fixed, the influence of the frictional forces might not be accounted for. The material that is selected for the model is the structural steel built-in material of COMSOL. The material that the Ocean Grazer Company decided for the foundation is structural steel S355. The properties in the COMSOL model will therefore be similar to the chosen material by the company. The S355 denotes the yield strength of the material, which is 355 MPa. With this yield strength the safety factor of the structure can be calculated, which gives insight in the performance of the foundation.

The stress plots are shown in figures 86 up to 89. These are used to obtain insights in the locations and magnitudes of the stress locations. Afterwards, the results are investigated with a variation in mesh to obtain a more accurate result.

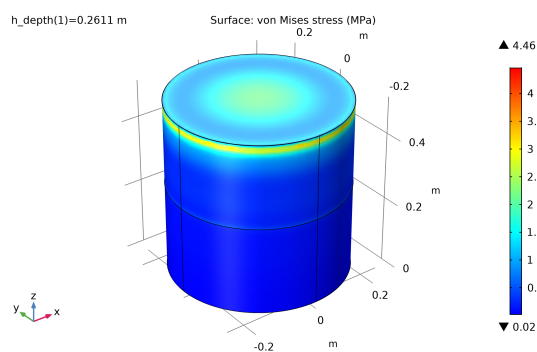


Figure 86: Stress plot Statoil sand

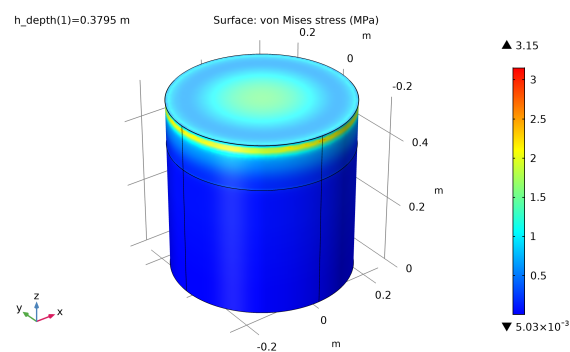


Figure 87: Stress plot Silica sand

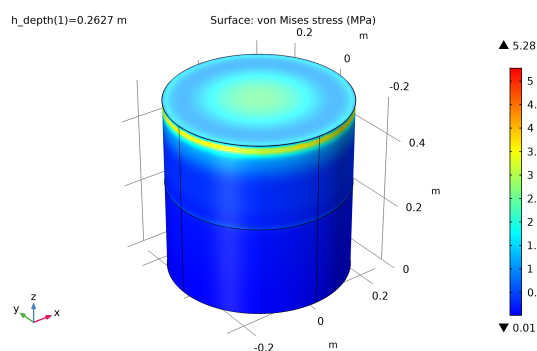


Figure 88: Stress plot Redhill sand

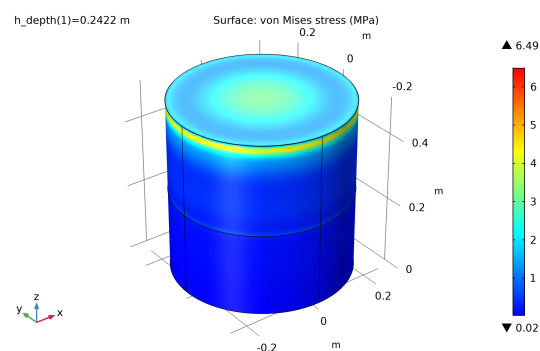


Figure 89: Stress plot Luce bay sand

From the plots of the different soils it can be observed that the location of the stress is equal in each case. The three main locations that have high stress concentrations are the top area of the caisson, the upper part of the skirts (near the sharp edge) at the inside and the same upper

part of skirts but on the inside of the caisson. The last stress concentration is not visible in figures 86 up to 89, but is shown in figure 90.

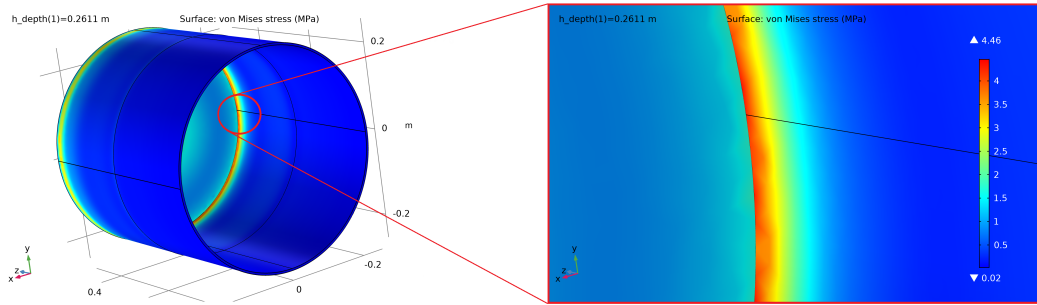


Figure 90: Inside of the caisson magnified for Statoil sand.

It can be seen from the plots (figures 86-89) that the difference in soil has a small influence on the total stress concentrations of the caissons, as the maximum values are relatively close to each other for the four soils. The highest stress concentration that can be found in the structure is located at the sharp corner on the inside part of the caisson, as can be seen in figure 90. The concentration around the sharp edge on the inside increases rather rapidly in a small length step. This can be seen in figure 91. This figure shows the stress at the inside in a straight line from the open part of the caisson to the closed upper part.

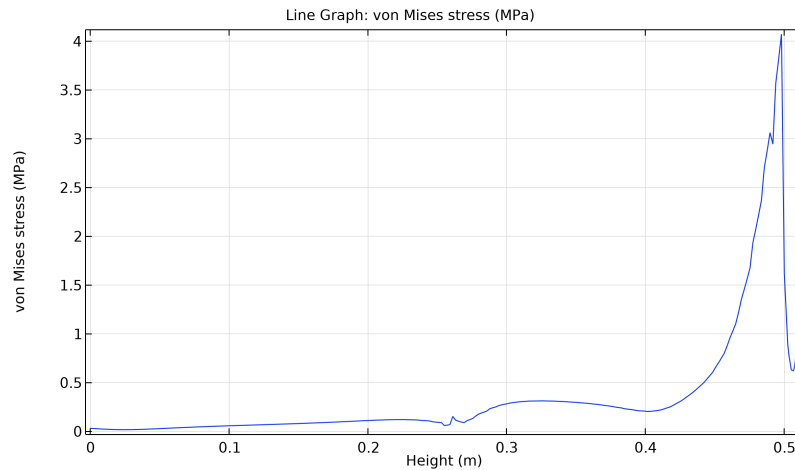


Figure 91: Stress over a straight line from bottom to the top in Statoil sand

From the figure it can be seen that at a height of 0.45 m the stress is increasing rapidly up to the point of the sharp corner. After this point is reached, the stress is decreasing. This shows that the sharp edge in the inside is a weak spot for this single caisson case. Another explanation for these high concentrations is that the sharp edge induces a singularity, which should be found when varying the mesh.

The influence of the hydrostatic pressure and the suction applied to the caisson can be seen in the displacement plots in figures 92 up to 95.

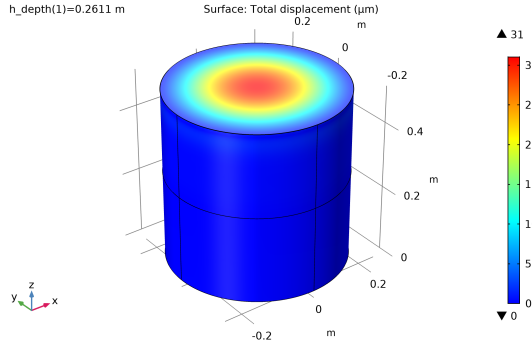


Figure 92: Displacement plot Statoil sand

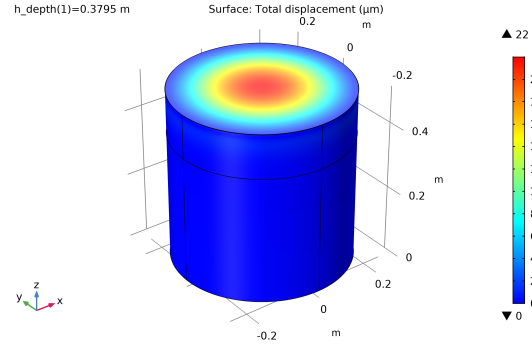


Figure 93: Displacement plot Silica sand

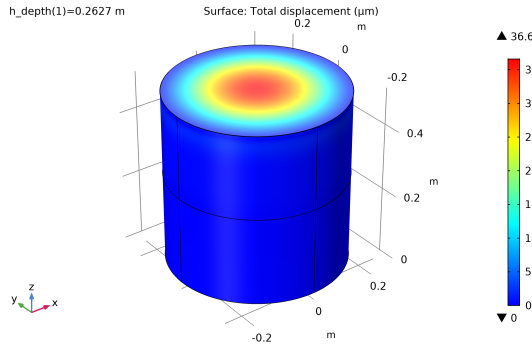


Figure 94: Displacement plot Redhill sand

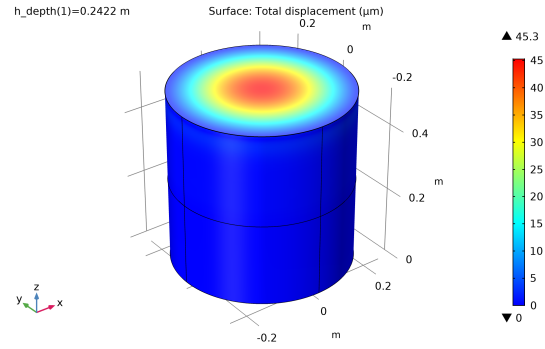


Figure 95: Displacement plot Luce bay sand

The plots show that the pressures acting on the structure will result in a rather small displacement of the structure. This displacement is the highest in the middle of the top part of the caisson and is in the range of 0.02 to 0.05 millimeter. Placing this in perspective, the complete thickness of the top part is one millimeter. Therefore, the plots show that for the single caisson case, the top part of the caisson does not deform significantly.

As stated previously in this section, the type of mesh is important for the results and their insights. Table 20 shows the variation in outcomes for different meshes used. Different mesh applications are used for obtaining an accurate result. However, as was described before, the highest stress concentrations are found near the sharp edge on the inside of the caisson. Within the COMSOL software, sharp corners often lead to singularities in the model (65). To overcome these singularities, a fillet is introduced in order to see the influence of the sharp corner and if there are indeed singularities introduced through the sharp corner.

From the first few entries (rows 1-3) in table 20, one can see that when the mesh is more refined, the maximum stress is increasing. This indicates that there are some singularities within the model. When the mesh is refined, combined with a fillet in the geometry, the maximum stress is decreasing. This is due to the fact that the software does not have to deal with a sharp corner anymore. One exception is the entry with a 0.0015 fillet radius. In this case the refinement placed on the fillet is unable to work and the software returns an error for this mesh application. The software returns an error and states a enormous value for the stress.

Max. element size	Corner refinement	Refine	fillet	Max. Stress	Max. Displacement
[m]	[-]	[-]	[m]	[MPa]	[μm]
0.0108	NO	NO	0	4.46	31
0.0108	YES	NO	0	7.09	31.4
0.0108	YES	Factor 2 *	0	11.1	31.7
0.0108	YES ***	NO	0.0015	ERROR	ERROR
0.0108	YES ***	NO	0.0030	5.32	30.6
0.0108	YES ***	NO	0.0040	5.04	30.1
0.0108	YES ***	NO	0.0050	4.73	29.5
0.0108	YES ***	NO	0.0100	3.68	26.8
0.0108	YES ***	Factor 2 **	0.0015	ERROR	ERROR
0.0108	YES ***	Factor 2 **	0.0030	5.53	30.6
0.0108	YES ***	Factor 2 **	0.0040	5.08	30.1
0.0108	YES ***	Factor 2 **	0.0050	4.79	29.6
0.0108	YES ***	Factor 2 **	0.0100	3.92	26.9
0.0108	YES ***	Factor 3 **	0.0030	5.55	30.6
0.0108	YES ***	Factor 3 **	0.0050	4.82	29.6

Table 20: Variations in result values with different meshes for the Statoil sand.

* Refinement in this case is added on the edge of the sharp corner.

** Refinement in this case is added on the fillet.

*** Corner refinement is applied on the fillet as well as the adjacent boundaries.

As there are no fillets present in the CAD model of the foundation of the Ocean Battery, the fillet added in the model becomes debatable. However, as the caisson needs to be welded, the sharp edge will not be a good representation. Therefore, the shape becomes more similar to a fillet. Therefore it possible to assume the presence of a fillet.

the final mesh chosen to compare the soils is chosen to be the mesh as specified in row 11 of table 20. This mesh consists of all the refinement applications and a fillet in the geometry of 3 mm. The results for the maximum stress and the maximum displacement are given for each type of cohesionless soil in table 21.

Soil Type	Max. Stress	Max. Displacement
[-]	[MPa]	[μm]
Statoil sand	4.46	31.0
Silica sand	3.93	21.6
Redhill sand	6.50	36.0
Luce bay sand	8.07	44.6

Table 21: Stress and displacement of the single caisson for the different cohesionless soils.

The table shows that there are no extremes present in the structure. The maximum stress is not exceeding the yield strength of the material, meaning that failure is not expected. The displacement is small in comparison to the thickness of the top plate, and therefore will not be a problem for the installation.

7.2.1.2 The full system

The full system model in COMSOL is used in the same approach as the single caisson case. The different parameters that are calculated through the MATLAB script are used in the COMSOL model. The COMSOL model contains similar variables to account for the environment of the ocean floor. For the full system, the same environmental conditions apply as for the single caisson case. The foundation is deployed at a depth of 10 meters. The material used for the full system model is the same material as was used for the single caisson case, structural Steel S355.

From the single caisson case, it was found that the sharp edges are introducing singularities within the model. Within the full system model, these sharp edges are rounded by fillets of a size of 3 mm. The reason to choose to fillet the edges before the first simulation is that the structure is assembled by means of welding. The joints of these welds are not perfectly a sharp corner and are mostly rounded. Therefore, for the full model it is chosen to account for these welding joints.

The four chamber model

From the matlab model, it is found that the full system is only able to be deployed in the silica sand when using four suction chambers in the case of cohesionless soils. The resulting penetration depths used in the COMSOL model are given in table 15. The penetration depth is simulated at 0.49 m depth for silica sand, to see the stress locations. If the depth would be set to 0.5 meter, the stresses across the fillets would not be visible. For the four chamber model, specific parameters from the MATLAB model are used. As the other chambers are not acting as suction caissons, the frictional terms of the plates will be used for all the connecting skirts of the foundation. Within the deactivated chambers, the water pressure will still be present as no suction is added to these five chambers. The stress plots are given in figures 96 up to 99.

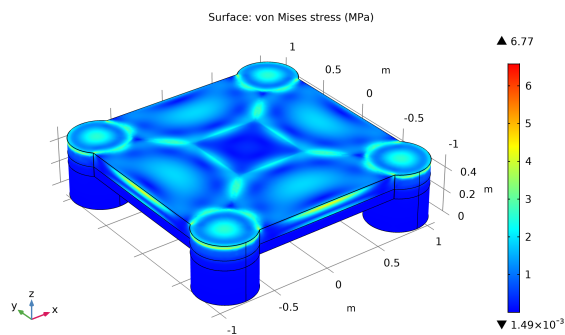


Figure 96: Stress plot Statoil sand

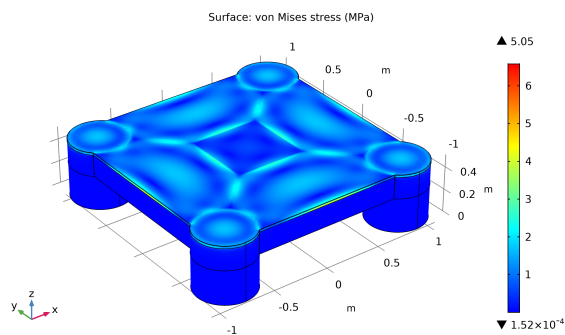


Figure 97: Stress plot Silica sand

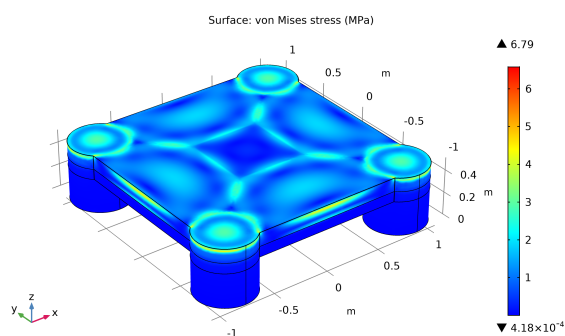


Figure 98: Stress plot Redhill sand

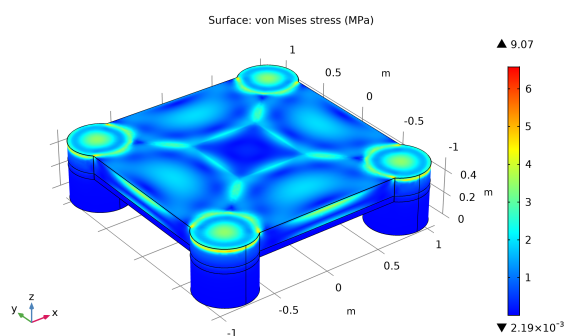


Figure 99: Stress plot Luce bay sand

The stress plots for the four chamber model show that the amount of stress is slightly higher than the stress found for the cohesionless single caisson case. One can see that the Luce Bay sand results in the highest stress found in the structure. The plot show that the concentrations are located mainly near to the welded edges, but also around the sharp edges at the outside of the structure. For the four circular suction caissons the location of the stress concentrations are similar to the locations found for the single caisson cases.

in figure 100 the stress locations are shown for the Statoil soil on the bottom side of the full system. The magnification shows that the stress concentrations are located near the welds that connect the skirts with each other.

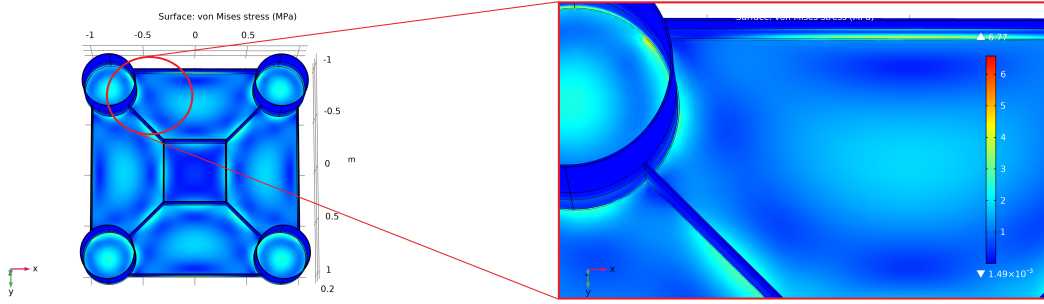


Figure 100: Magnification on stress locations for the full system with four active chambers for Statoil sand.

The plots shown in figures 101 up to 104 show the displacements in the four chamber system.

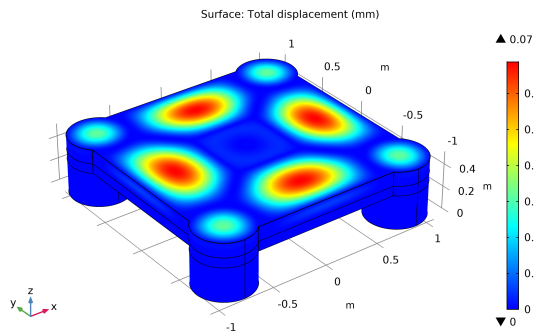


Figure 101: Displacement plot Statoil sand

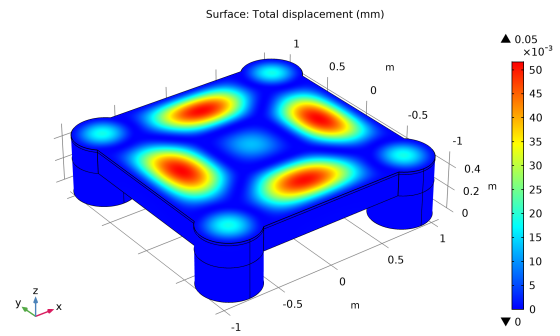


Figure 102: Displacement plot Silica sand

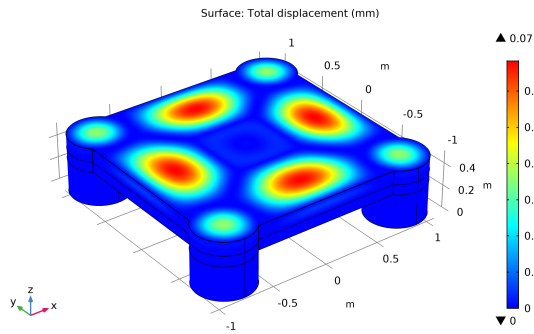


Figure 103: Displacement plot Redhill sand

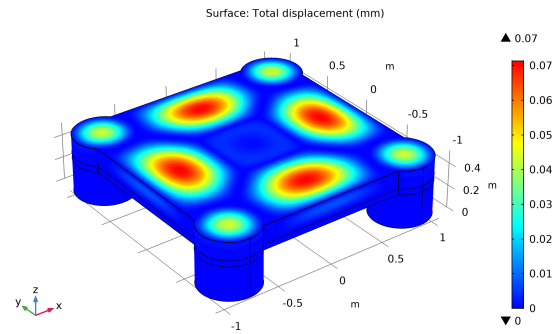


Figure 104: Displacement plot Luce bay sand

From the plots it can be observed that the displacements are rather small and do not exceed a value of 0.1 mm. The locations on the four round suction caissons are caused by the pressure difference between the outside and the inside. The locations formed at the platform plate are caused by the hydrostatic pressure that is acting on a smaller area due to the installation.

As was done in for the single caisson, the mesh is investigated. By reducing the maximum element size and adding both corner refinements and refinement factors, the accuracy of the solution of the model can be increased. The full model needs more elements than the single caisson case and will therefore need more computational power. Therefore, the mesh for the full system is more coarse in comparison with the single caisson model. The variations in mesh are shown in table 22.

The final mesh that will be chosen for the cohesionless four chamber model, will be used for the five chamber model and nine chamber model as well.

Max. element size	Min. element size	Corner refinement	Refine	Max. Stress	Max. Displacement
[m]	[-]	[-]	[m]	[MPa]	[mm]
0.172	0.0215	NO	NO	6.77	0.07
0.100	0.0215	NO	NO	6.73	0.07
0.090	0.0215	NO	NO	6.47	0.07
0.050	0.0215	NO	NO	5.68	0.07
0.172	0.0215	YES *	NO	8.67	0.07
0.100	0.0215	YES *	NO	7.85	0.07
0.090	0.0215	YES *	NO	6.56	0.07
0.050	0.0215	YES *	NO	5.94	0.07
0.172	0.0215	YES *	Factor 1 **	9.26	0.07
0.100	0.0215	YES *	Factor 1 **	8.39	0.07
0.090	0.0215	YES *	Factor 1 **	10.5	0.07
0.050	0.0215	YES *	Factor 1 **	7.55	0.07

Table 22: Variations in result values with different meshes for the Statoil sand for the four chamber model.

* Corner refinement is added on the boundaries where the hydrostatic pressure is acting.

** The refinement is added to all the fillets present in the model.

From table 22, the last mesh option is chosen for the four chamber model. As the maximum element size is as low as possible the accuracy is increased. Adding corner refinements and refinement factors on specified locations, enables the model to built fine meshes on specified locations within the model, while some locations can remain being defined by coarser meshes. Therefore, the last mesh has the finest mesh possible within the computational power. The result for the stress values, found with this chosen mesh, are found in table 23.

Soil Type	Max. Stress	Max. Displacement
[-]	[MPa]	[mm]
Statoil sand	7.55	0.07
Silica sand	4.94	0.05
Redhill sand	7.87	0.07
Luce bay sand	11.3	0.07

Table 23: Stress and displacement of the Full system for the different cohesionless soils with four active chambers.

The table shows that there are no extremes present in the structure for the four chamber model. The maximum stress is not exceeding the yield strength of the material, meaning that failure is not expected. The displacement is small in comparison to the thickness of the top plate, and therefore will not be a problem for the installation for all the soils.

The five chamber model

For the five chamber model, the same approach is taken as was done for the four chamber model. However, the mesh will not be varied for this case. The mesh used for the five chamber model is the same as the final mesh chosen for the four chamber model. The corner refinement is placed on the same boundaries as in the four chamber model. The same holds for the refinement factor. The stress plots for the five chamber model are shown in figure 105 up to 107. As the foundation can be fully installed in silica sand, this type of soil is not considered for this case.

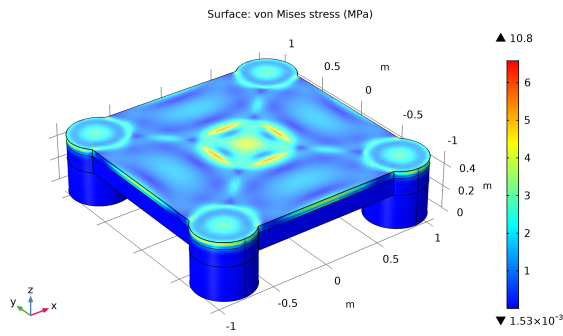


Figure 105: Stress plot Statoil sand

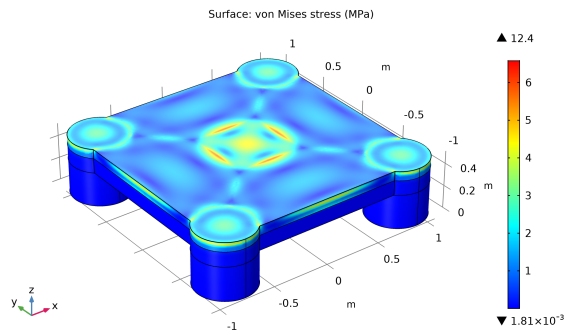


Figure 106: Stress plot Redhill sand

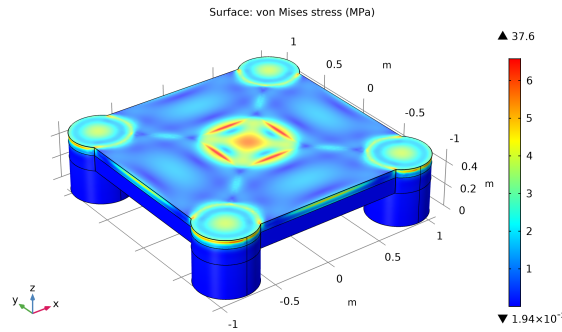


Figure 107: Stress plot Luce bay sand

The stress plots for the five chamber model show that the amount of stress increased significantly in comparison with the four chamber model. Especially the stress values for the Luce bay sand are significantly increased. The highest values for the stress are found along on the platform plate along the welded edges of the connecting skirts of the square caisson. In figure 108 the stress locations are shown for the Statoil soil on the bottom side of the full system.

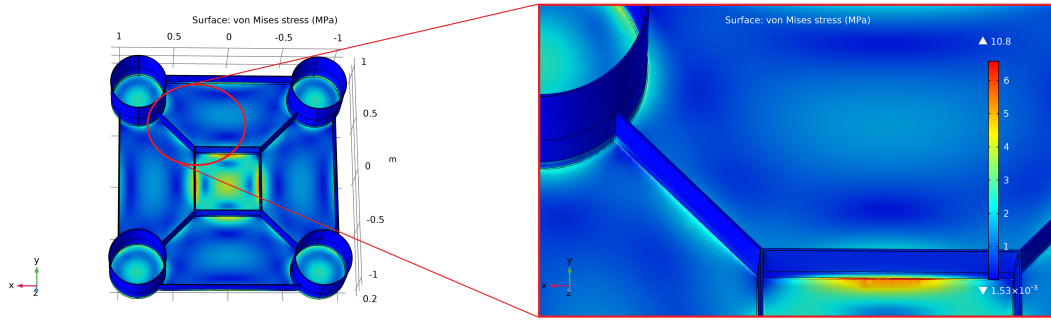


Figure 108: Magnification on stress locations for the full system with five active chambers for Statoil sand.

The magnification shows that the stress concentrations are located near the welds that connect the skirts with each other. The highest stress locations are located around the top parts of the four circular caissons around the fillet and the fillets of the connecting skirts of the square caisson. These locations are due to the difference in pressure between the outside and inside. The corresponding displacement plots of the five chamber model are shown in figure 109 up to 111.

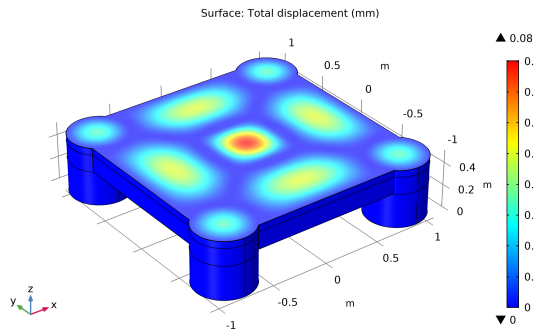


Figure 109: Displacement plot Statoil sand

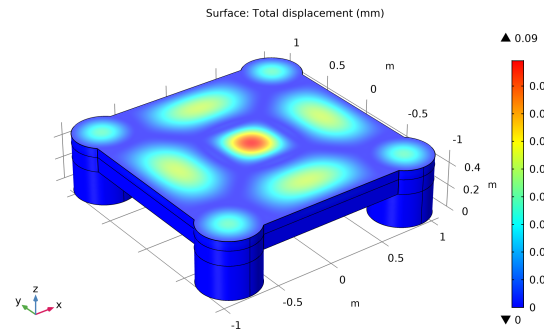


Figure 110: Displacement plot Redhill sand

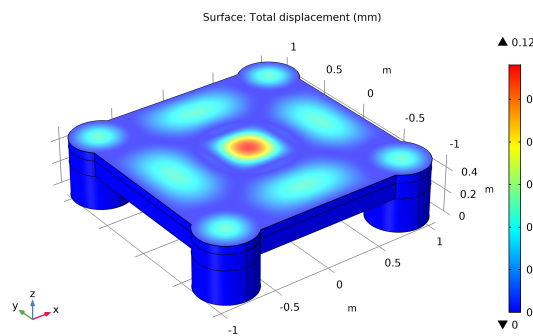


Figure 111: Displacement plot Luce bay sand

The plots show that the main location that deforms the most, is located in the middle of the square caisson. This is due to the pressure difference between the outside and the inside of the caisson. The same holds for the top plates of the circular caissons. The values of the displacement are similar to the values found for the four chamber model.

Using the specified mesh from the four chamber model in the previous section, the values for

the stresses found in the three soils considered for this case. The values of the stress and displacement are shown in table 24.

Soil Type	Max. Stress	Max. Displacement
[-]	[MPa]	[mm]
Statoil sand	10.8	0.08
Redhill sand	12.4	0.09
Luce bay sand	37.6	0.12

Table 24: Stress and displacement of the Full system for the different cohesionless soils with five active chambers.

The table shows that there are no extremes present in the structure for the five chamber model. The maximum stress is not exceeding the yield strength of the material, meaning that failure is not expected. The displacement is small in comparison to the thickness of the top plate, and therefore will not be a problem for the installation for all the soil types.

The nine chamber model

For the nine chamber model, the same approach is taken as was done for the four chamber model. However, the mesh will not be varied for this case. The mesh used for the nine chamber model is the same as the final mesh chosen for the four chamber model. The corner refinement is placed on the same boundaries as in the four and five chamber model. The same holds for the refinement factor. The stress plots for the five chamber model are shown in figure 112 up to 114. As the foundation can be fully installed in silica sand, this type of soil is not considered for this case. The penetration depth is simulated at 0.49 m depth, to see the stress locations. If the depth would be set to 0.5 meter, the stresses across the fillets would not be visible.

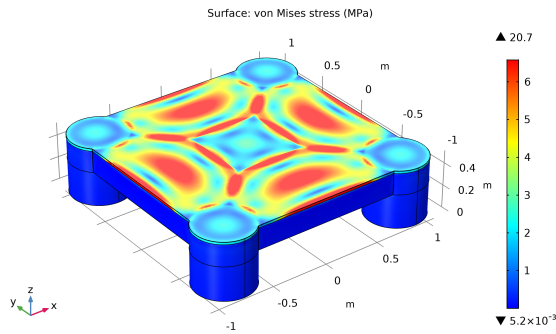


Figure 112: Stress plot Statoil sand

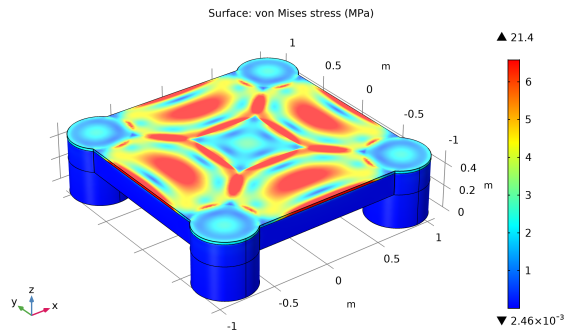


Figure 113: Stress plot Redhill sand

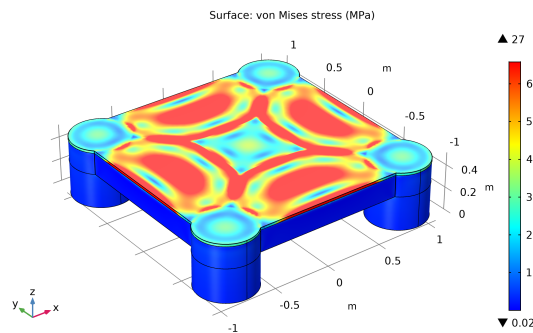


Figure 114: Stress plot Luce bay sand

The stress plots for the nine chamber model show that the amount of stress again increased significantly in comparison with the five chamber model. It is important to note that the range of the maximum and minimum stress for the Luce Bay sand is different than the other two soil cases. As was the case in the five chamber model, the highest increase is found in the Luce bay sand case. The highest values for the stress are found along the top surface of the trapezoidal caissons. The stress concentrates especially around the connecting skirts (inside and outside), dividing the chambers. In figure 115 the stress locations are shown for the Statoil soil on the bottom side of the full system.

The magnification shows that the stress concentrations are located near the welds that connect the skirts with each other. The highest stress locations are located around the top parts of the four circular caissons around the fillet, and the fillets of the connecting skirts dividing the five chambers (inside and outside). These locations are due to the difference in pressure between the outside and inside.

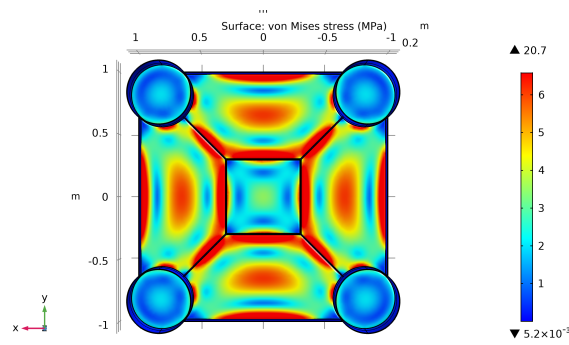


Figure 115: Magnification on stress locations for the full system with nine active chambers in Statoil sand

The corresponding displacement plots of the five chamber model are shown in figure 116 up to 118. It can be observed from the plots that the displacement locations mainly focus at the top surface of the trapezoidal suction caissons. The main cause of the deformation is the difference in pressure between the inside of the chamber and the outside. The middle of these trapezoidal chambers are the locations that have no near reinforcement through a connecting skirt. Therefore the displacement is maximized at the middle of the trapezoidal caissons

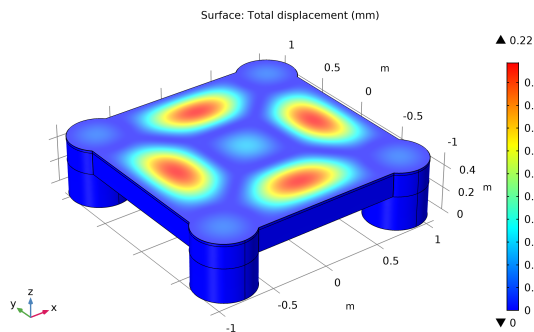


Figure 116: Displacement plot Statoil sand

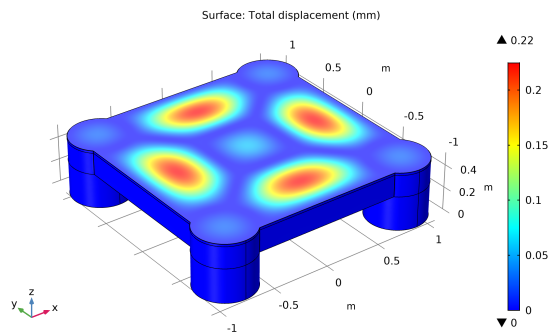


Figure 117: Displacement plot Redhill sand

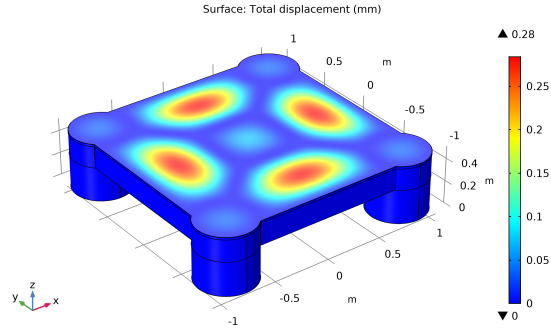


Figure 118: Displacement plot Luce bay sand

Using the specified mesh from the four chamber model, the values for the stresses found in the three soils considered for this case. The values of the stress and displacement are shown in table 25.

Soil Type	Max. Stress	Max. Displacement
[-]	[MPa]	[mm]
Statoil sand	20.7	0.22
Redhill sand	21.4	0.22
Luce bay sand	27.0	0.28

Table 25: Stress and displacement of the Full system for the different cohesionless soils with nine active chambers.

The table shows that there are no extremes present in the structure for the nine chamber model. The maximum stress is not exceeding the yield strength of the material, meaning that failure is not expected. The displacement is small in comparison to the thickness of the top plate, and therefore will not be a problem for the installation for all soil types.

7.2.2 Cohesive Soil Results

7.2.2.1 The single caisson model

The first case for the cohesive (clay type) soils is the same as for the cohesionless soils, namely the single caisson model. The conditions for the caisson are the same, meaning that it is deployed on 10 meters depth and the chosen material is S355 structural steel. The values for the forces and required suction are again taken from the MATLAB model and added to the COMSOL model. As the MATLAB model showed, the caisson can be fully installed in the cohesive soils. Therefore it is chosen to take the penetration depth of 0.49 meter depth, in order to apply the same variation in mesh. Another reason to place the penetration depth at 0.49 meter is to see if the stress location will act on the same places as was the case with the cohesionless soils. The stress plots for the cohesive soils are shown in figures 119 up to 121.

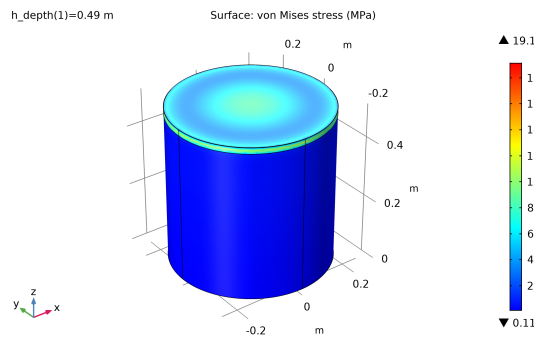


Figure 119: Stress plot Kaolin clay

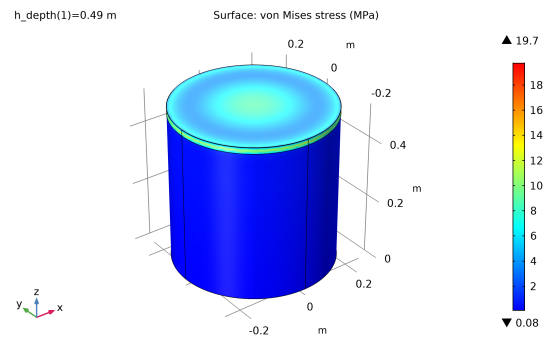


Figure 120: Stress plot Nkossa clay

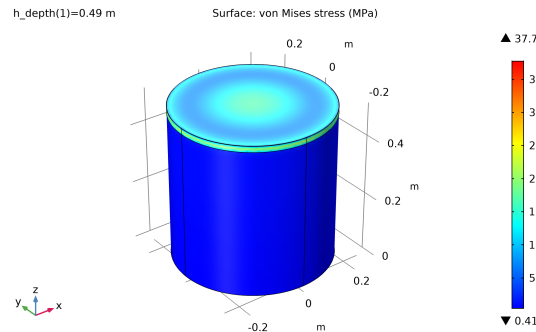


Figure 121: Stress plot Qiantang silt

The plots in figure 119 up to 121 show that there is a higher influence on the type of soil when compared to cohesionless soils. The Qiantang river silt induces a higher stress on the caisson than the two clay soils. The clay soils itself show that there is a small difference between the maximum stresses. The locations of the stress concentration show to be similar to the locations found for cohesionless soils, namely at the top, and the area around the sharp edge both on the outside and inside. The concentration is not visible in the plots above, but is shown in figure 122.

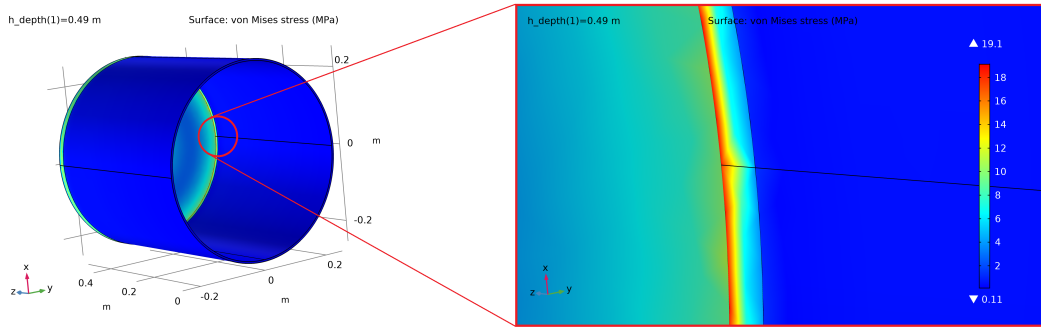


Figure 122: Inside of the caisson magnified for Kaolin clay.

In figure 122 it can be observed that the stress concentration is located at the same sharp edge as was found for cohesionless soils. The figure shows that the stress increases rather rapidly in a relatively small step in length. This is shown in figure 123, which shows the stress over a straight line over the inside of the caisson. As the caissons are able to be fully deployed, the stress concentration has a smaller area on which it acts in comparison with the cohesionless soils.

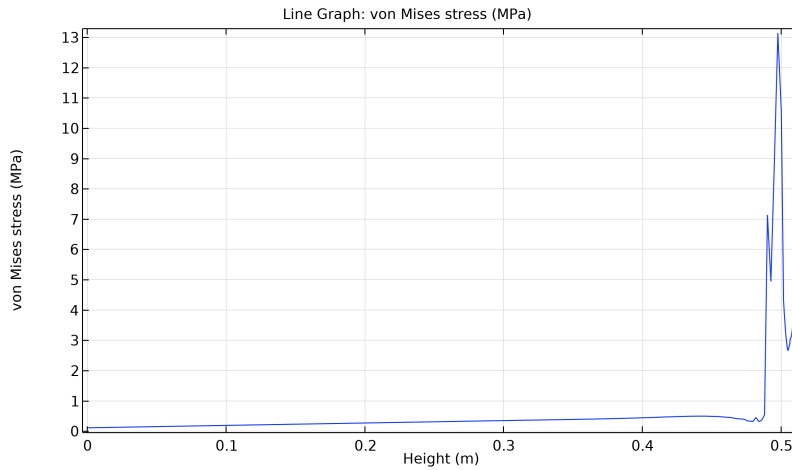


Figure 123: Stress over a straight line from bottom to the top in Kaolin clay

The graph in figure 123 shows that starting from 0.49 meter the stress increases rapidly up to the maximum and afterwards decreases again. Therefore the edge within the inside of the caisson is considered to be a weak spot in the caisson. The edge can also be a singularity that is induced by the sharp edge. A variation in mesh sizes has to be analysed in order to see if the sharp edge indeed induces a singularity. The corresponding displacement of the caisson throughout the three cohesive soils are shown in figures 124 up to 126.

The displacement plots show that for the cohesive soils similar observations can be made for the caisson. The displacements itself are rather small for the design of the single caisson. However, compared with the cohesionless soils, the displacements are higher for the cohesive case. When compared to the thickness of the top plate of the caisson, the displacements are rather small. This means that for the installation the displacement is not inducing a problem.

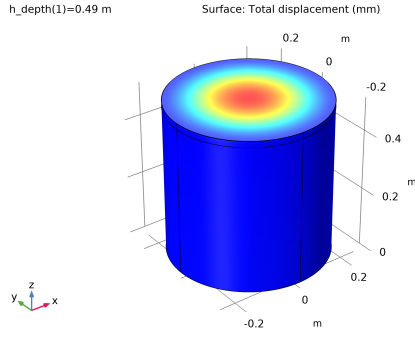


Figure 124: Displacement plot Kaolin clay

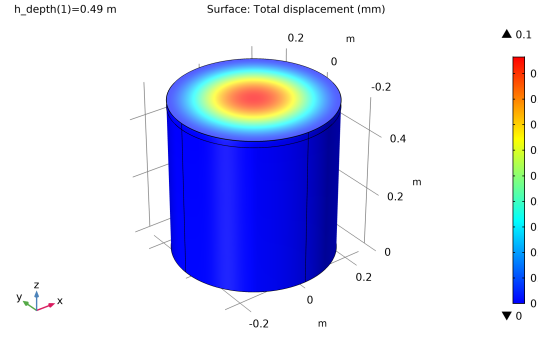


Figure 125: Displacement plot Nkossa clay

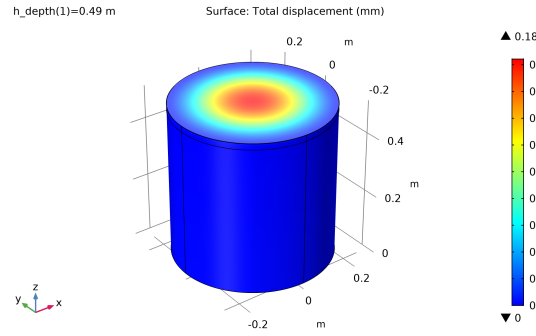


Figure 126: Displacement plot Qiantang silt

As was done for the cohesionless soils, the accuracy of the model is important. Therefore, the same variations in mesh are applied to the cohesive soil case. The result of these variations in mesh are given in table 26.

Max. element size	Corner refinement	Refine	fillet	Max. Stress	Max. Displacement
[m]	[-]	[-]	[m]	[MPa]	[mm]
0.0108	NO	NO	0	19.1	0.09
0.0108	YES	NO	0	27.5	0.09
0.0108	YES	Factor 2 *	0	42.8	0.10
0.0108	YES ***	NO	0.0015	Error	Error
0.0108	YES ***	NO	0.0030	21.7	0.09
0.0108	YES ***	NO	0.0040	18.5	0.09
0.0108	YES ***	NO	0.0050	16.4	0.09
0.0108	YES ***	NO	0.0090 ****	10.8	0.08
0.0108	YES ***	Factor 2 **	0.0015	Error	Error
0.0108	YES ***	Factor 2 **	0.0030	22.0	0.09
0.0108	YES ***	Factor 2 **	0.0040	19.0	0.09
0.0108	YES ***	Factor 2 **	0.0050	16.6	0.09
0.0108	YES ***	Factor 2 **	0.0090 ****	11.2	0.08
0.0108	YES ***	Factor 3 **	0.0030	22	0.09
0.0108	YES ***	Factor 3 **	0.0050	16.8	0.09

Table 26: Variations in result values with different meshes for the Kaolin clay.

* Refinement in this case is added on the edge of the sharp corner.

** Refinement in this case is added on the fillet.

*** Corner refinement is applied on the fillet as well as the adjacent boundaries.

**** The dimension of this radius is different from the cohesionless soils as otherwise the software will have difficulties in meshing.

In the case of the cohesive soils, the same mesh is chosen for the caisson. The mesh applied is the mesh with the corner refinement and refinement factor of 2 applied. The fillet applied on the sharp edge is equal to 3 mm. With this mesh, the values for stress and displacement for the three different cohesive soils can be obtained. These results are shown in table 27.

Soil Type	Max. Stress	Max. Displacement
[-]	[MPa]	[μm]
Kaolin clay	22.0	0.09
Nkossa clay	22.7	0.09
Qiantang silt	43.4	0.18

Table 27: Stress and displacement of the single caisson for the different cohesive soils.

The table shows that there are no extremes present in the structure. The maximum stress is not exceeding the yield strength of the material, meaning that failure is not expected. The displacement is small in comparison to the thickness of the top plate, and therefore will not be a problem for the installation.

7.2.2.2 The full system

The four chamber model

From the MATLAB model, it is found that the full system is able to be deployed in the two of the three cohesive soils when using four suction chambers. The resulting penetration depth for Qiantang silt used in the COMSOL model is given in table 18. For the other two soil types, the penetration depth is set to 0.49 meters in order to investigate where the stress concentrations will built up. The same was done for the single caisson case for cohesive soils. The penetration depth is simulated at 0.49 m depth for the Kaolin and Nkossa clays, to see the stress locations. If the depth would be set to 0.5 meter, the stresses across the fillets would not be visible.

For the four chamber model, specific parameters from the MATLAB model are used. As the other chambers are not acting as suction caissons, the frictional terms of the plates will be used for all the connecting skirts of the foundation. Within the chambers, the water pressure will still be present as no suction is added to these five chambers. The stress plots are given in figures 127 up to 129.

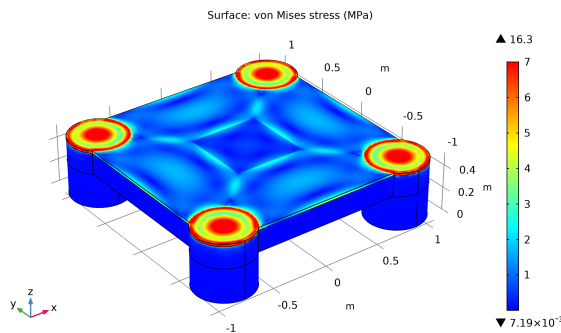


Figure 127: Stress plot Kaolin clay.

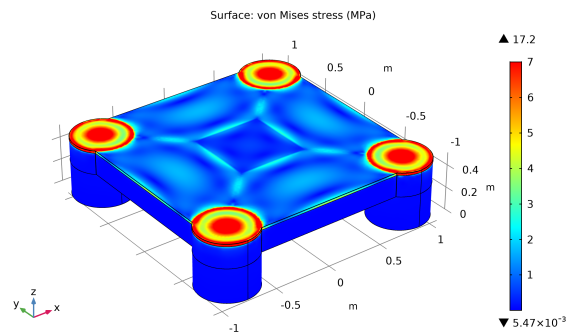


Figure 128: Stress plot Nkossa clay

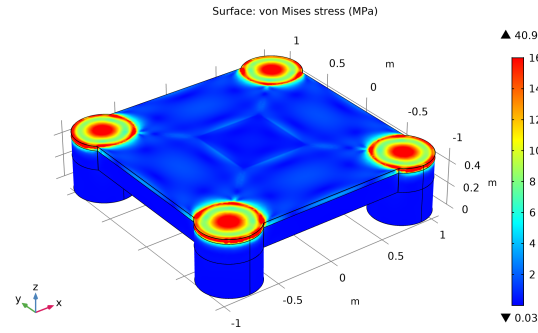


Figure 129: Stress plot Qiantang silt

The stress plots show that the maximum stress is significantly higher than the stresses found for the cohesionless soils. As was found in the single caisson case for the cohesive soils, the Qiantang silt soil induces a significant higher stress than the two clay soils. The highest stresses are found at the top of the four circular suction caissons. The highest stresses are induced at the edges of the caisson as well as the middle of the top plate of these circular caisson.

Figure 130 shows the stress locations at the bottom side of the structure. The figure shows that on the bottom part the stress locations are mainly located at the fillets of the connecting skirts. However, the highest concentrations are located at the four circular caissons as mentioned previously.

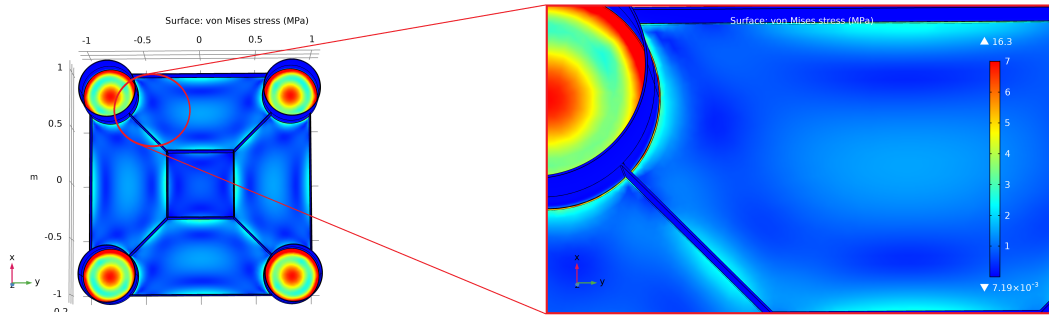


Figure 130: Magnification on stress locations for the full system with four active chambers in Kaolin clay.

The corresponding displacement plots for the four chamber model for cohesive soils are shown in figures 131 and 133. These displacements are induced due to the same reason as the stresses, the difference in pressure.

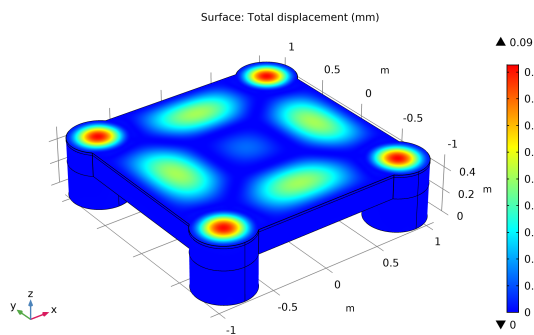


Figure 131: Displacement plot Kaolin clay.

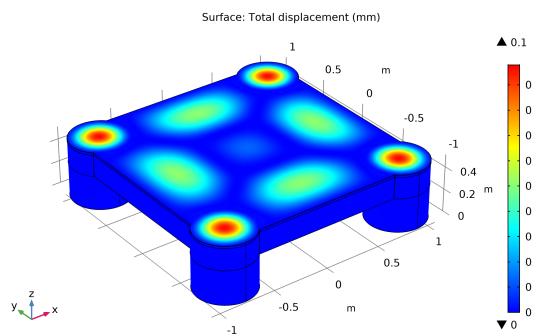


Figure 132: Displacement plot Nkossa clay

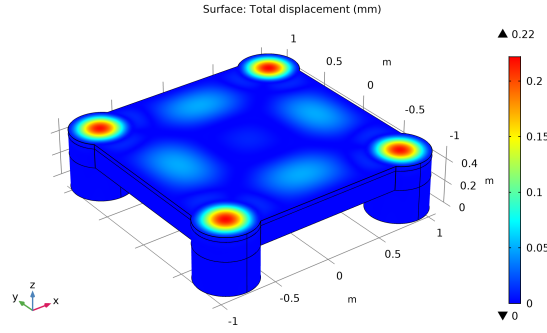


Figure 133: Displacement plot Qiantang silt

The values of the displacements are significantly higher for the Qiantang silt than for the two clay soils. Besides the four caissons having a displacement field, the trapezoidal top surface is also displaced. The displacement is due to the pressure differences deforming the circular caissons which will displace the material at the trapezoidal chambers as well. However, the magnitude of these displacements are lower than the displacements at the circular caissons.

As was done in the single caisson case for cohesive soils, the mesh is investigated. By reducing the maximum element size and adding both corner refinements and refinement factors, the accuracy of the solution of the model can be increased. The full model needs more elements than the single caisson case and will therefore need more computational power. Therefore, the mesh for the full system is more coarse in comparison with the single caisson model. The variations in mesh are shown in table 28.

Max. element size	Min. element size	Corner refinement	Refine	Max. Stress	Max. Displacement
[m]	[-]	[-]	[m]	[MPa]	[mm]
0.172	0.0215	NO	NO	16.3	0.09
0.100	0.0215	NO	NO	17.6	0.09
0.090	0.0215	NO	NO	17.2	0.09
0.050	0.0215	NO	NO	14.3	0.09
0.172	0.0215	YES	NO	16.6	0.09
0.100	0.0215	YES	NO	18.1	0.09
0.090	0.0215	YES	NO	17.1	0.09
0.050	0.0215	YES	NO	17.1	0.09
0.172	0.0215	YES	YES	50.8	0.09
0.100	0.0215	YES	YES	50.3	0.09
0.090	0.0215	YES	YES	21.8	0.09
0.050	0.0215	YES	YES	24.7	0.09

Table 28: Variations in result values with different meshes for the Kaolin clay for the four chamber model.

From table 28, the last mesh option is chosen for the four chamber model. As the maximum element size is as low as possible the accuracy is increased. Adding corner refinements and refinement factors on specified locations, enables the model to built fine meshes on specified locations within the model, while some locations can remain being defined by coarser meshes. Therefore, the last mesh has the finest mesh possible within the computational power. The result for the stress values, found with this chosen mesh, are found in table 29.

Soil Type	Max. Stress	Max. Displacement
[-]	[MPa]	[mm]
Kaolin clay	24.7	0.09
Nkossa clay	26.2	0.10
Qiantang silt	89.8	0.22

Table 29: Stress and displacement of the Full system for the different cohesive soils with four active chambers.

The table shows that there are no extremes present in the structure for the four chamber model for the cohesive soils. The maximum stress is not exceeding the yield strength of the material, meaning that failure is not expected. The displacement is small in comparison to the thickness of the top plate, and therefore will not be a problem for the installation for all soil types.

The five chamber model

For the five chamber model, the same approach is taken as was done for the four chamber model. However, the mesh will not be varied for this case. The mesh used for the five chamber model is the same as the final mesh chosen for the four chamber model. The corner refinement is placed on the same boundaries as in the four and five chamber model. The same holds for the refinement factor. From the MATLAB results, it was found that only the Qiantang River silt prevented the complete system with four active suction chambers to fully be deployed. The penetration depth is simulated at 0.49 m depth, to see the stress locations. If the depth would be set to 0.5 meter, the stresses across the fillets would not be visible.

The stress plot and displacement plot for the five chamber model are shown in figure 134 and 135.

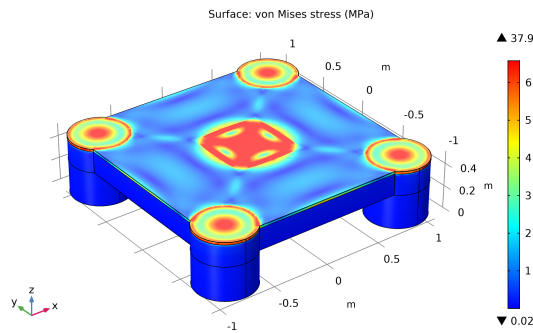


Figure 134: Stress plot Qiantang silt

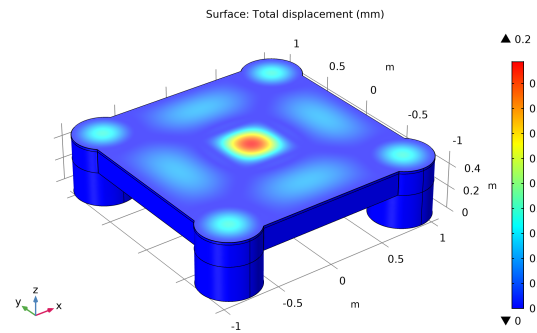


Figure 135: Displacement plot Qiantang silt

The stress plot shows that when the square suction caisson is activated, the stress does not increase. what can be seen from the plot is that an additional stress concentration is found along the surface of the square caisson. This stress concentration is formed by the pressure difference between the inside of the caisson and the outside of the caisson. The displacement that is resulting from the loads is also focused around the square caisson, with in the middle the largest deformation.

The stresses for the bottom side of the structure are shown in figure 136. From this plot, it is observed that there are some stress concentrations at the fillets of the connecting skirts, but their magnitude is significantly lower than the main stress concentrations at the inside of the square suction caisson and the four circular suction caissons.

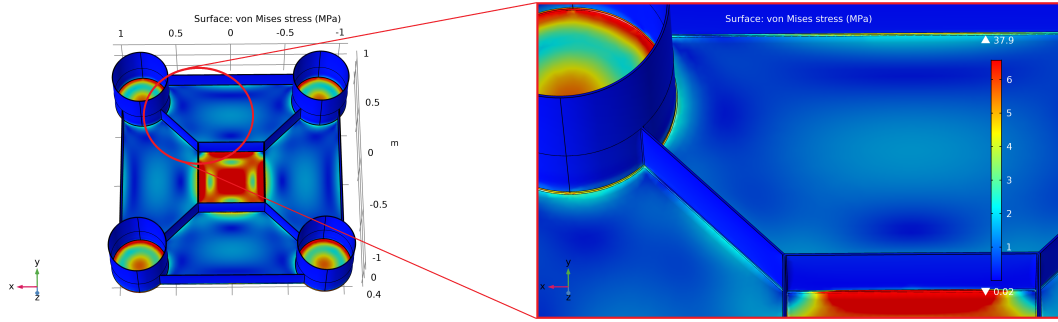


Figure 136: Magnification on stress locations for the full system with five active chambers in Qiantang silt

Using the specified mesh from the four chamber model in the previous section, the values for the stresses found in the three soils considered for this case. The values of the stress and displacement are shown in table 30.

Soil Type	Max. Stress	Max. Displacement
[-]	[MPa]	[mm]
Qiantang silt	37.9	0.20

Table 30: Stress and displacement of the Full system for the different cohesive soils with five active chambers.

The table shows that there are no extremes present in the structure for the five chamber model. The maximum stress is not exceeding the yield strength of the material, meaning that failure is not expected. The displacement is small in comparison to the thickness of the top plate, and therefore will not be a problem for the installation for the Qiantang silt.

8 Discussion

The results found in 7.1 and 7.2 show that the foundation of the second ocean grazer prototype is able to be fully deployed in the different soils discussed in section 5.3. The structure shows that the forces are not causing significantly high stress concentrations that would lead to a failure of the design. The MATLAB model and COMSOL model show to present useful insights for the structural behaviour of the Ocean Battery foundation of the Ocean Grazer company.

The strategy, discussed in section 6.2, used in the research, starting with the single caissons and finishing with the full system, proves to be a useful strategy in analysing the behaviour of the foundation of the Battery System. The models of the single caisson case showed initial insights in how suction caissons interact with the seabed and how the stress will be distributed in the design.

The equations of Houlsby and Byrne show that there is a large amount of variables that have to be taken into account when analysing the interaction with the soil. This large amount of variables, both variables of the design (for example dimensions) as environment variables (for example soil parameters), make that the equations are rather complex. Besides the equations being rather complex, the equations given are solely designed for each type of soil (cohesive and cohesionless). As soils can be layered, the equations are not able to describe the behaviour in layered materials. The authors indicate that for layered soils, the researches of Senpere and Auvergne (66) or or Tjelta (67) provide more reference.

The complexity with a high number of variables in the equations caused a difficulty in finding values for the required soil parameters. Especially for the soils commonly found in the North Sea and Eemshaven. It proved to be rather difficult to find specified values for the soil parameters of these locations. The available soils that were discussed in 5.3 provide different cases that give an insight in how the behaviour of the foundation is in different soil types. However, the MATLAB code provided able to cope with new soil types if necessary. If the values for a specific desired location are know, the values can be used in the MATLAB code to analyse the behaviour in the soil of the desired location.

The assumptions stated in section 6.3 have made the modelling of the design of the second prototype of the Ocean Grazer less complex. Each of these assumptions have an implication on the end result of the simulation outcome. Several of these assumptions can be validated through a validation test at the test location in the Eemshaven. The first assumption mentioned in the assumption list should result in an over estimation of the frictional terms in the circular caisson. As the frictional force at the tips of the caisson is dependent on the area, the real friction term will have a lower value due to the smaller area.

Furthermore, the equations proposed by Houlsby and Byrne are formulated for the case of circular caissons. As the design of the Ocean Grazer consist of circular, square and trapezoidal suction caissons, the latter two are estimated through rewriting the equations of Houlsby and Byrne. As the research from K. van de Loo concluded, the square caisson has a higher vulnerability to the piping phenomenon due to the sharp corners in the design (68). However, by applying a more controlled installation, the caisson proved to be able to deploy in the lab tests (68). Full scale test should provide insight and validation for the MATLAB model obtained. During the research it is assumed that the rewritten equations could be used to describe the behaviour of the non-circular suction caissons (Assumption 2 in section 6.3).

When the circumferences of the trapezoidal and square caissons are calculated, it is observed that these circumferences have overlapping parts. Therefore, some parts of the circumferences of the non-circular suction caissons are accounted for twice. This leads to an over estimation of the results of the forces and stresses on these plates.

Furthermore, the suction is assumed to be equal in all the suction chambers. This assumption is made due to the fact that the weight distribution, needed for the calculation, is not exactly known. When the required suction is slightly different from the calculated suction, the distribution in stresses will slightly differ in their distribution. However, the locations of the stress concentration will remain on the same places in the design, whereas their magnitude might differ.

The fillet that has been assumed for the full system model was set to 3 mm. As the single caisson case showed, the size of the fillet in the design has a rather high influence on the stress. As the size of the fillet increases, the value of the stress decreases and the singularities in the sharp edges can be avoided. The assumption made for the full system, of applying a radius of 3 mm, denotes that the welds in the system will have a size of 3 mm. The company TWI, a consultancy company providing expert advice, knowhow for engineering, materials and joining technologies, has stated an advice for the welding size of fillet joints based on the thickness of the base material (69). For a base material with a thickness smaller than 6 mm (which is the case for the Ocean Grazer Battery Foundation), a fillet weld with the size of 3 mm is advised (70).

Although the welds are not directly modeled in COMSOL, the implications can be discussed. The weld metal strength is defined as the yield and tensile strength of the deposited weld material (or filler material) (71). Depending on the filler material that is used to create the weld, the weld has a certain strength. The weld metal, or filler material, is tried to match the minimum strength properties of the base metal. When the weld material is unmatched, the strength properties of the weld are lower than the ones of the base metal. For overmatching, the weld strength properties are higher than the properties of the base metal (71). Commonly, welds are as strong or even stronger than the base metal that is being welded (72). According to the Welding Process Handbook (58) the acceptable stress that a weld joint can withstand is based on both the ultimate tensile strength of the base metal and the filler material. Besides these two parameters, the acceptable stress is also dependent on the weld class (denoting the desired quality level) and the safety factor of the design. Different assumptions on the match of the weld material might lead to different conclusions on the welds behavior.

As the two models, MATLAB and COMSOL, are made in different software packages, they are not directly linked to each other. This means that the values from MATLAB have to be added manually to the COMSOL model. This takes up more time and increases the risk of mistakes. However, for this research, the different values from the MATLAB model needed for the COMSOL model are structured in an EXCEL sheet to obtain more oversight in the variables. In the MATLAB model, a manual accuracy is set for the calculations (i.e. the step size in penetration depth). This means that a critical value might just be in between a step size, and the number leads to a result in the COMSOL model that might not be an accurate representation of the situation.

The accuracy of the COMSOL model can be manually adjusted by creating an user defined mesh. In the results given in sections 7.1 and 7.2, these manually defined mesh sizes are given. During the simulations the aim was to get an accurate results while remaining within the boundaries of the computational power of the system. Given the current situation, it was not possible to run simulations on a system with more computational power. However, through several refinements the accuracy of the solution of the simulations is increased and, especially in the single caisson case, showed that certain singularities can be found and avoided (through fillets) in the model.

9 Conclusion

The aim of the project was to formulate an answer to the research question, formulated at the beginning of this report:

How does the foundation of the second prototype, of the Ocean Grazers battery system, behave under different loads and in different soil types in terms of stress and displacement?

Through modelling different complex sets of equations in MATLAB and using the outcomes in the COMSOL software, the research showed that the structural behaviour of the Ocean Grazer its battery foundation system can be analysed through these two software packages. The models obtained showed different sets of results that identify the behaviour of the Battery foundation through seven different soil cases as discussed in 5.3.

The results given in the sections 7.1 and 7.2 show to be promising for the Ocean Grazer company. With the required suction calculated, the system is able to be fully deployed. This full installation can be done through different combinations of active suction caissons, which is different for each of the seven investigated soils.

The behaviour of the soils is quite similar within their own soil classes (cohesionless and cohesive). The two classes compared give different behaviours in the frictional forces, the required suction and the holding capacity. This difference in behaviour is caused through the dependency on the penetration depth in the equations provided by Houlsby and Byrne. Where the cohesionless soils are quadratically dependent on the penetration depth, the cohesive soils are only linearly dependent on this variable. These equations proved to be useful in determining the behaviour of the system, even though the equations proved to be complex and dependent on many different variables.

Testing the soil in the Eemshaven showed that the test location consisted mainly of harbor mud. Therefore, for the first prototype (single caisson with pump housing) a simulation could be run for the required suction. However, as the exact composition of the mud and the required variables were not exactly known, the system was tested for the three cohesive soils mentioned in section 5.3. The suction plots showed that the system was able to fully be deployed in all three soils.

The structural behaviour modelled through the COMSOL model showed that in each case of the seven soil types, no extremely high values were found for both the stress and displacement in the full system model. From the COMSOL results, it was concluded that both the Luce Bay sand for the cohesionless case and the Qiantang silt for the cohesive case caused the highest stress concentrations in the structure. The values found for the stresses and displacement showed to not be high enough to cause failure within the design of the foundation.

Both models, in both MATLAB and COMSOL, that were formulated and created during the research showed to be useful tools for the analysis of the structural behaviour of the foundation of the Battery System Foundation of the Ocean Grazer.

10 Recommendations and Limitations

There are several limitations and recommendations that can be formulated from the research.

As mentioned in the discussion, there is a limitation in the means of the computing power of to compute the solutions for the full system model in COMSOL. If more accurate calculations are required, the recommendation would be to run the model with a finer mesh than specified in the research and on a system that has more computational power.

A second recommendation can be formulated through the limitation of known variables of the Eemshaven soil. Further research can be done to investigate the soil of the Eemshaven, in order to be able to obtain the variables needed for the equations provided by Houlsby and Byrne. This is also recommended for any test locations that might follow. To fully predict the behavior on the test location, these variables have to be investigated.

Further research can be done to explore the case where the soil consists of layered sand and clay. As the equations provided by Houlsby and Byrne are designed for either cohesionless or cohesive soils (as discussed previously), the layered soils might lead to a limitation of the models. Further research can extend the code obtained in this research to account for layered soils as well.

Another investigation that can be done following up this research is to include the reservoir and add the movement of the working fluid within the reservoir. The movement of the working fluid moving from the reservoir to the bladder might lead to additional stresses within the foundation of the Battery System. This also holds for the stress concentrations that might be induced in the powerhouses, as there will act a higher pressure difference between the inside and outside of the powerhouses.

As this research focuses on the second prototype of the Battery system, further research can be done to analyse the third prototype. As this prototype is still being developed in CAD software, investigating this prototype was rather difficult as exact measurements were not yet fully clear. The MATLAB code obtained in this research is written such that it is possible to scale the model and the end user is able to analyse the third prototype as well.

Another recommendation is to add a method of modelling the welds within the COMSOL model. The current model does not have specific conditions to model these welds apart from the fillet within the geometry. An extension can be made to incorporate a method of modelling these welds to be able to give insight in the weld behavior.

The last recommendation would be to investigate the connection points of the reservoir and the foundation for the third prototype. As the third prototype will be built with different materials, these connection points become important in the overall integrity of the battery system.

11 Bibliography

- [1] C. Taylor, “Un urges global emissions cuts and warns of ‘bleak’ climate change outlook,” (Online) 2019 [Accessed: 30-8-2020]. Available at: <https://www.cnn.com/2019/11/26/un-urges-global-emissions-cuts-warns-of-bleak-climate-change-outlook.html>.
- [2] Tesla, “website of tesla,” (Online) 2020 [Accessed: 10-3-2020]. Available at: https://www.tesla.com/nl_nl/energy.
- [3] J. Titcomb, “Elon musk says he will fix south australia’s power in 100 days - or do it for free,” The Telegraph, (Online) 2017 [Accessed: 10-3-2020]. Available at: <https://www.telegraph.co.uk/technology/2017/03/10/elon-musk-makes-audacious-twitter-bet-fix-south-australias-power/>.
- [4] E. Clowes, “Tesla’s big australian battery about to get even bigger,” The Telegraph, (Online) 2019 [Accessed: 10-3-2020]. Available at: <https://www.telegraph.co.uk/business/2019/11/19/teslas-big-australia-battery-get-even-bigger/>.
- [5] B. Fung, “Tesla’s enormous battery in australia, just weeks old, is already responding to outages in ‘record’ time,” The Washington Post, (Online) 2017 [Accessed: 10-3-2020]. Available at: <https://www.washingtonpost.com/news/the-switch/wp/2017/12/26/teslas-enormous-battery-in-australia-just-weeks-old-is-already-responding-to-outages-in-record-time/>.
- [6] Ocean Grazer BV, “Ocean energy for a sustainable future,” (Online) 2020 [Accessed: 10-3-2020]. Available at: <https://oceangrazer.com/>.
- [7] European Commission, “Horizon 2020, work programme 2016-2017. general annexes,” (Online) 2020 [Accessed: 9-3-2020]. Available at: <https://ec.europa.eu/info/funding-tenders/opportunities/portal/screen/support/faq/2890>.
- [8] COMSOL multiphysics, “The finite element method (fem),” (Online) 2016 [Accessed: 17-4-2020]. Available at: <https://www.comsol.com/multiphysics/finite-element-method>.
- [9] H. Hu, *Fluid Mechanics*. Elsevier Science, 2012. Chapter 10 - Computational Fluid Dynamics.
- [10] M. Zeinoddini, S. Mousavi, and M. Abdi, “Simulation of suction caisson penetration in seabed using an adaptive mesh technique,” *Procedia Engineering*, no. 14, 2011.
- [11] S. Nielsen, “Finite element modeling of the tensile capacity of suction caissons in cohesionless soil,” *Applied Ocean Research*, no. 90, 2019.
- [12] Z. Guo, D. Jeng, W. Guo, and R. He, “Simplified approximation for seepage effect on penetration resistance of suction caissons in sand,” *Ships and Offshore Structures*, no. 12, 2016.
- [13] A. Alluqmani, M. Naqash, and O. Harireche, “A standard formulation for the installation of suction caissons in sand,” *Journal of Ocean Engineering and Science*, no. 4, pp. 395–405, 2019.
- [14] COMSOL Multiphysics, “Expand structural analyses for geotechnical applications with the geomechanics module,” (Online) 2020 [Accessed: 6-4-2020]. Available at: <https://www.comsol.com/geomechanics-module>.

- [15] Unknown, “Dassault systèmes acquisition of abaqus — affirming the importance of analysis and simulation (commentary),” (Online) 2005 [Accessed: 5-4-2020]. Available at: <https://www.cimdata.com/de/news/item/36-dassault-systemes-acquisition-of-abaqus-affirming-the-importance-of-analysis-and-simulation-commentary>.
- [16] Simuleon, “Simuleon industries,” (Online) 2020 [Accessed: 5-4-2020]. Available at: <https://www.simuleon.com/nl/industrie-oplossingen/>.
- [17] Bentley software company, “Plaxis geotechnical finite element analysis software,” (Online) 2020 [Accessed: 5-4-2020]. Available at: <https://www.bentley.com/en/products/brands/plaxis>.
- [18] S. Chakrabarti, *Handbook of Offshore Engineering*. Elsevier Science, 2005. Chapter 1.
- [19] M. Randolph and S. Gourvenec, *Offshore Geotechnical Engineering*. CRC Press LLC, 2011. Chapter 1.
- [20] A. Kaynia, “Seismic considerations in design of offshore wind turbines,” *Soil Dynamics and Earthquake Engineering*, no. 124, pp. 399–407, 2019.
- [21] M. Esteban, J. López-Gutiérrez, and V. Negro, “Gravity-based foundations in the offshore wind sector,” *Marine Science and Engineering*, no. 7, 2019.
- [22] B. Byrne, G. Houlsby, C. Martin, and P. Fish, “Suction caisson foundations for offshore wind turbines,” *Wind Engineering*, no. 3, pp. 145–155, 2002.
- [23] W. Guo and J. Chu, “Suction caisson installation in shallow water: Model tests and prediction,” in *Proceedings of the 18th International Conference on Soil Mechanics and Geotechnical Engineering*, pp. 1999–2002, 2013.
- [24] S. Chakrabarti, *Handbook of Offshore Engineering*. Elsevier Science, 2005. Chapter 14.
- [25] G. Houlsby and B. Byrne, “Calculation procedures for installation of suction caissons,” Report No. OUEL 2268/04, University of Oxford, Parks Road, Oxford, 2004.
- [26] M. Senders, “Suction caissons in sand as tripod foundations for offshore wind turbines,” Master’s thesis, The University of Western Australia, School of Civil and Resource Engineering, 2008.
- [27] W. Yuqi, L. Dayong, Z. Yukun, and C. Fuquan, “Determination of maximum penetration depth of suction caissons in sand,” *KSCE Journal of Civil Engineering*, no. 22, 2017.
- [28] M. Iskander, S. El-Gharbawy, and R. Olson, “Performance of suction caissons in sand and clay,” *Canadian Geotech*, no. 39, 2002.
- [29] L. Hung, S. L. an N. Xuan Tran, and S. Kim, “Experimental investigation of the vertical pullout cyclic response of bucket foundations in sand,” *Applied Ocean Research*, no. 68, 2017.
- [30] D. Coduto, *Foundation design: principles and practices*. Upper Saddle River, New Jersey, USA: Prentice Hall, 2 ed., 2001.
- [31] A. Altarriba I Subirana, “Stresses and deformation analysis of the storage system structure of the ocean grazer,” Master’s thesis, University of Groningen, Faculty of Science and Engineering, 2020.
- [32] D. van Tongeren, “Analytical calculations on the nine-chambered suction anchor,” Bachelor’s Thesis, University of Groningen, Faculty of Science and Engineering, 2020.

- [33] B. Das, *Principles of Foundation Engineering*. Toronto, Ontario, Canada: Thomson, 5 ed., 2007.
- [34] W. Yuqi, Z. Yu, and L. Dayong, "Solution to critical suction pressure of penetrating suction caissons into clay using limit analysis," *Applied Ocean Research*, no. 101, 2020.
- [35] N. van Dijken, "Seabed conditions and its relation to suction anchor operation," Bachelor's Thesis, University of Groningen, Faculty of Science and Engineering, 2020.
- [36] EMODnet, "Central portal," (Online) 2016 [Accessed: 4-7-2020]. Available at: <https://www.emodnet.eu/>.
- [37] EMODnet, "Geology," (Online) 2016 [Accessed: 4-7-2020]. Available at: <https://www.emodnet-geology.eu/map-viewer/>.
- [38] EMODnet, "Bathymetry," (Online) 2016 [Accessed: 4-7-2020]. Available at: <https://portal.emodnet-bathymetry.eu/>.
- [39] International Organization for Standardization, "Geotechnical investigation and testing - identification and classification of soil," *ISO*, 2017.
- [40] P. Bobrowsky and B. Marker, *Encyclopedia of Engineering Geology*. Encyclopedia of Earth Sciences Series, Springer, 2018.
- [41] A. Tikkanen, "Kaolin, clay," (Online) 2016 [Accessed: 5-7-2020]. Available at: <https://www.britannica.com/science/kaolin>.
- [42] H. Zhou and M. Randolph, "Large deformation analysis of suction caisson installation in clay," *Canadian Geotechnical Journal*, no. 12, 2006.
- [43] E. Napolitano, "Hydrological and stability modelling of initial landslides triggering debris flows in ash-fall deposits covering hillslopes surrounding somma-vesuvius (southern italy).," 2011. Doctoral Dissertation, University of Napels, Faculty of Science.
- [44] Geotechdata, "Angle of friction," (Online) 2013 [Accessed: 5-7-2020]. Available at: <http://geotechdata.info/parameter/angle-of-friction>.
- [45] J. Colliat, P. Boisard, P. Sparrevik, and J. Gramet, "Design and installation of suction anchor piles at soft clay site," *Journal of Waterway, Port, Coastal and Ocean Engineering*, no. 4, 1998.
- [46] V. Murthy, *Geotechnical Engineering: Principles and Practices of Soil Mechanics and Foundation Engineering*. Madison Avenue, New York, USA: Marcel Dekker, Inc., 1 ed., 2003.
- [47] L.Wang, Z. Wang, and Z.Guo, "Seepage induced soil failure and its mitigation during suction caisson installation in silt," *Journal of Offshore Mechanics and Arctic Engineering*, no. 136, 2014.
- [48] B. Schlue and S. Kreiter, "Undrained shear strength properties of organic harbor mud at low consolidation stress levels," *Canadian Geotechnical Journal*, no. 48, 2011.
- [49] H. Niroumand and A. Kassim, *Design and Construction of Soil Anchor Plates*. Butterworth-Heinemann, 2016. Chapter 3 - Horizontal Anchor Plates in Cohesionless Soil.
- [50] D. Abel and R. McConnell, *Environmental Oceanography: Topics and Analysis*. Mississauga, Ontario, Canada: Jones and Bartlett Publishers, 1 ed., 2010.

- [51] M. van der Meulen et al, “Silica sand resources in the netherlands,” *Netherlands Journal of Geosciences — Geologie en Mijnbouw*, 2009.
- [52] T. Tjelta, “Geotechnical aspects of bucket foundations replacing piles for the europipe 16/11-e jacket,” *Offshore Technology Conference*, 1994.
- [53] T. Tjelta and C. Erbrich, “Installation of bucket foundations and suction caissons in sand – geotechnical performance,” *Offshore Technology Conference*, 1999.
- [54] F. Villalobos, ed., *Installation of Suction Caissons in Sand*, 2007.
- [55] A. Blakeborough and B. Byrne, “Pipe uplift in saturated sand: Rate and density effects,” *Géotechnique*, 2013.
- [56] G. Houlsby, R. Kelly, J. Huxtable, and B. Byrne, “Field trials of suction caissons in sand for offshore wind turbine foundations,” *Géotechnique*, no. 56, 2013.
- [57] R. Singh, *Applied Welding Engineering: Processs, Codes and Standards*. Elsevier Science, 2 ed., 2015. Chapter 5.
- [58] K. Weman, *Welding Processes Handbook*. Stockholm, Sweden: Woodhead Publishing, 2 ed., 2012.
- [59] R. Singh, *Applied Welding Engineering: Processs, Codes and Standards*. Elsevier Science, 2 ed., 2015. Chapter 2.
- [60] P. Jukes, “Fabrication welding processes,” *Encyclopedia of Maritime and Offshore Engineering*, 2017.
- [61] Unkown, “Arc welding,” (Online) [Accessed: 31-8-2020]. Available at: <http://4mechtech.blogspot.com/2011/11/arc-welding.html>.
- [62] H. Kals, *Industriële productie*. Den Haag, Netherlands: Sdu Uitgevers, 5 ed., 2012. Chapter 8.
- [63] R. Singh, *Applied Welding Engineering: Processs, Codes and Standards*. Elsevier Science, 2 ed., 2015. Chapter 3.
- [64] M. van Rooij, “Pictures of the tests of the eemshaven soil,” 2020.
- [65] W. Frei, “How to identify and resolve singularities in the model when meshing,” (Online) 2013 [Accessed: 20-8-2020]. Available at: <https://www.comsol.com/blogs/how-identify-resolve-singularities-model-meshing/>.
- [66] D. Senpere and G. Auvergne, “Suction anchor piles – a proven alternative to driving or drilling,” *Offshore Technology Conference*, 1982.
- [67] T. Tjelta, “Suction piles: their position and application today,” *Proc. 11th Int. Symp. on Offshore and Polar Eng*, 2001.
- [68] K. van de Loo, “Laboratory experiments on the technical feasibility of the ocean battery suction foundation in sand,” Bachelor’s Thesis, University of Groningen, Faculty of Science and Engineering, 2020.
- [69] T. company, “Who we are,” (Online) 2020 [Accessed: 02-9-2020]. Available at: <https://www.twi-global.com/who-we-are>.

- [70] T. company, “How do you determine the minimum size of a fillet weld?,” (Online) 2020 [Accessed: 02-9-2020]. Available at:
<https://www.twi-global.com/technical-knowledge/faqs/faq-how-do-you-determine-the-minimum-size-of-a-fillet-weld>.
- [71] D. Miller, “Use undermatching weld metal where advantageous,” *Welding Innovation*, vol. 14, no. 1, 1997.
- [72] S. Merek, “When brazing beats welding,” (Online) 2004 [Accessed: 25-9-2020]. Available at:
<https://www.machinedesign.com/fastening-joining/article/21832464/when-brazing-beats-welding>.

12 Appendices

12.1 Appendix A: Unified Soil Classification System

Major Division			Group Symbol	Description
Coarse Grained Soils	Gravels	Clean Gravels	GW	Well graded gravels, gravel-sand mixtures, little or no fines
			GP	Poorly graded gravels, gravel-sand mixtures, little or no fines.
		Gravels with Fines	GM	Silty gravels, gravel-sand-silt mixtures.
			GC	Clayey gravels, gravel-sand-clay mixtures
	Sands	Clean Sands	SW	Well graded sands, gravelly sands, little or no fines.
			SP	Poorly graded sands, gravelly sands, little or no fines.
		Sands with Fines	SM	Silty sands, sand-silt mixtures.
			SC	Clayey sands, sand-clay mixtures.
Fine Grained Soils	Silts and Clays Liquid Limit less than 50		ML	Inorganic silts and very fine sands, silty or clayey fine sands, clayey silts.
			CL	Inorganic clays of low to medium plasticity, lean clays.
			OL	Organic clays of low to medium plasticity, lean clays.
	Silts and Clays Liquid Limit greater than 50		MH	Inorganic silts, fine sand or silty soils, elastic silts.
			CH	Inorganic clays of high plasticity, fat clays.
			OH	Organic clays of medium to high plasticity, organic silts.
Highly Organic Soils			PT	Peat and other highly organic soils.

Table 31: The Unified Classification System of soils (43)

12.2 Appendix B: Matlab code

```
%% Master Thesis %% Ocean Grazer's second prototype %%
% Author: Lennard Hut (S2718960)
% Year: 2020

% About this script:
% This script calculates the different load factors that are used within
% the COMSOL model. Each Calculation set provides a different parameter
% that is calculated in order to check the COMSOL determination or to
% calculate parameters needed in the simulations.

% Case: Full functioning model for predicting penetration behaviour.

% The model determines through parameters set in the prompt which type of
% soil is used and the corresponding parameters.

close all
clear all
clc

%% Designing the prompts %%
% These prompts will request different parameters of the user, which will
% be coupled to their appropriate matlab parameters.

%-----
% Save the values in their own variable name for the Caisson
%-----

% Calling a prompt for the design parameters of the caissons
prompt = {'Inner diameter of the Suction Caisson [m] :', ...
        'Outer diameter of the Suction Caisson [m]:', ...
        'Inner height of the Suction Caisson [m]:', ...
        'Outer height of the Suction Caisson [m]:'};
dlg_title = 'Design Parameters Suction Caisson';
num_lines = 1;
defaultans = {'0.498', '0.508', '0.50', '0.51'};
answer = inputdlg(prompt, dlg_title, [1 70], defaultans);

for i = 1:(size(answer))
    data(i) = str2num(answer{i});
end

D_inner = data(1);           % Inner diameter of the caisson [m]
D_outer = data(2);           % Outer diameter of the caisson [m]
H_inner = data(3);           % Inner height of the caisson [m]
H_outer = data(4);           % Outer height of the caisson [m]

%-----
% Save the values in their own variable name for the skirts
%-----
```

```

% Calling a second prompt for the design parameters of the skirts
prompt2 = {'Length of the Caisson Connecting Skirts [m]:', ...
    'Length of the Middle Skirts [m]:', ...
    'Length of the Diagonal Connecting Skirts [m]:',...
    'Height of the Skirt [m]:','Thickness of the Skirt [m]:', ...
    'Length of the Platform Plate [m]:','Width of the Platform Plate [m]:'...
    ', 'Thickness of the Platform Plate [m]:'};
dlg_title2 = 'Design Parameters Skirts';
num_lines = 1;
defaultans2 = {'1.28','0.61','0.48','0.21','0.005','1.998',...
    '1.998','0.01'};
answer2 = inputdlg(prompt2,dlg_title2,[1 80],defaultans2);

for i = 1:(size(answer2))
    data2(i) = str2num(answer2{i});
end

L_plate_outerskirts      = data2(1);      % Length of the outerskirts [m]
L_plate_innerskirts      = data2(2);      % Length of the inner skirts [m]
L_plate_diagonalskirts   = data2(3);      % Length of the diagonal skirts [m]
H_plates                 = data2(4);      % Height of the skirts [m]
t_plates                 = data2(5);      % Thickness of the skirts [m]
L_plate_platform         = data2(6);      % Length of the platform [m]
W_plate_platform         = data2(7);      % Width of the platform [m]
t_plate_platform         = data2(8);      % Thickness of the platform [m]

%-----
% Save the values in their own variable name for the remaining
% parameters
%-----

% Calling a third prompt for other needed parameters
prompt3 = {'Density of the Foundation Material [kg/m^3]:', ...
    'Density of the Sea Water [kg/m^3]', ...
    'Total Weight of the Complete Structure [kg]',};
dlg_title3 = 'Additional Parameters';
num_lines = 1;
defaultans3 = {'7850','1020','1089.9'};
answer3 = inputdlg(prompt3,dlg_title3,[1 80],defaultans3);

for i = 1:(size(answer3))
    data3(i) = str2num(answer3{i});
end

rho_mat = data3(1);          % Density of the foundation [kg/m^3]
rho_wat = data3(2);          % Density of the water [kg/m^3]
Total_system_Weight=data3(3); % Weight of the Ocean Battery [kg]

%-----

```



```

% Save the values in their own variable name for the remaining
% parameters
%-----

list = {'Silica Sand','Statoil Sand','Redhill 110 Sand',...
        'Luce Bay Sand','Kaolin Clay','Nkossa Clay', 'Qiantang River Silt'};
[indx,tf] = listdlg('PromptString',{'Select a soil type.',...
    'Only select one of the soils.'},'SelectionMode','single',...
    'ListString', list, 'ListSize', [300, 300], 'Name', ...
    'Select a soil type');

if indx == 1          % For Silica Sand
    y_komma          = 5993;      % Effective soil weight [kN/m^3]
    Ktandelta        = 0.63;      % [-]
    phi              = 36;        % Angle of friction [degree]
    k_f              = 1;        % Permeability ratio [-]

elseif indx == 2      % For Statoil Sand
    y_komma          = 8500;      % Effective soil weight [kN/m^3]
    Ktandelta        = 0.8;      % [-]
    phi              = 45;        % Angle of friction [degree]
    k_f              = 3;        % Permeability ratio [-]

elseif indx == 3      % For Redhill 110 Sand
    y_komma          = 7820;      % Effective soil weight [kN/m^3]
    Ktandelta        = 0.8;      % [-]
    phi              = 36;        % Angle of friction [degree]
    k_f              = 5;        % Permeability ratio [-]

elseif indx == 4      % For Luce Bay Sand
    y_komma          = 10300;     % Effective soil weight [kN/m^3]
    Ktandelta        = 0.8;      % [-]
    phi              = 45;        % Angle of friction [degree]
    k_f              = 5;        % Permeability ratio [-]

elseif indx == 5      % For Kaolin Clay
    y_komma          = 6500;      % Effective soil weight [kN/m^3]
    Ktandelta        = 0.8;      % [-]
    phi              = 26;        % Angle of friction [degree]
    alpha            = 0.5;      % Adhesion factor [-]
    s_u0             = 4000;      % Mudline shear strength [Pa]
    rate_change       = 1500;     % Shear strength rate [Pa]

elseif indx == 6      % For Nkossa Clay
    y_komma          = 6000;      % Effective soil weight [kN/m^3]
    Ktandelta        = 0.8;      % [-]
    phi              = 19;        % Angle of friction [degree]
    alpha            = 0.45;     % Adhesion factor [-]
    s_u0             = 5000;      % Mudline shear strength [Pa]
    rate_change       = 1670;     % Shear strength rate [Pa]

```

```

elseif indx == 7    % For Qiantang River Silt
    y_komma          = 8823;    % Effective soil weight [kN/m3]
    Ktandelta         = 0.8;    % [-]
    phi               = 36.5;    % Angle of friction [degree]
    alpha             = 0.5;    % Adhesion factor [-]
    s_u0              = 6000;    % Mudline shear strength [Pa]
    rate_change       = 1350;    % Shear strength rate [Pa]
else
end

% Calculating the bearing capacity factors
% Bearing capacity factor overburden [-] (Houlsby and Byrne)
Nq = (exp(2*pi*(0.75-(phi/360))*tand(phi)))/...
    (2*(cosd(45+(phi/2))^2));
% Bearing capacity factor self-weight [-] (Houlsby and Byrne)
Ny = (2*(Nq+1)*tand(phi))/(1+0.4*sind(phi));
% Bearing capacity factor cohesion [-]
Nc = (Nq-1)/tand(phi);

%% Calculating different basis parameters
gravity      = 9.81;    % Gravity acceleration constant [m/s^2]
m_SW         = 1.5;    % Multiple of the diameter for enhanced stress [-]

% Calculation of parameters of the suction caissons
% Thickness of the suction caisson walls [m]
t            = ((D_outer-D_inner)/2);
% Average Diameter of the suction caisson [m]
D_av         = ((D_outer+D_inner)/2);
% Height difference between plates and caisson
H_split      = H_outer - H_plates;
% Volume calculation of the suction caisson [m^3]
Vol_SC       = (pi*((D_outer/2)^2)*H_outer)-(pi*((D_inner/2)^2)*H_inner);
% Weight calculation of the suction caisson [kg]
Weight_SC    = Vol_SC*rho_mat;
% Vertical load due to the weight of the suction caisson [N]
WeightForce_SC = gravity*Weight_SC;
% Buoyancy force of the submerged suction caisson [N]
Fbuoy_SC     = Vol_SC*rho_wat*gravity;

%-----
% Calculating the circumferences of the plates
%-----

% The plates connecting the caissons
% Calculating the outer circumference of the plates between the caissons [m]
C_o_outskirts = 0.25*((2*L_plate_outskirts)+2*(L_plate_outskirts...
    +(2*t_plates)));
% Calculating the inner circumference of the plates between the caissons [m]
C_i_outskirts = 0.25*((2*L_plate_outskirts)+2*(L_plate_outskirts...
    -(2*t_plates)));
% Calculating the average circumference of the plates between the caissons [m]

```

```

C_av_outerskirts = 0.25*((C_o_outerskirts+C_i_outerskirts)/2);

% The plates that form a square in the middle
% Calculating the outer circumference of the plates in the middle [m]
C_o_innerskirts = 0.25*(2*L_plate_innerskirts + 2*(L_plate_innerskirts...
    +(2*t_plates)));
% Calculating the inner circumference of the plates in the middle [m]
C_i_innerskirts = 0.25*(2*L_plate_innerskirts + 2*(L_plate_innerskirts...
    -(2*t_plates)));
% Calculating the average circumference of the plates in the middle [m]
C_av_innerskirts = 0.25*((C_o_innerskirts+C_i_innerskirts)/2);

% The diagonal plates connecting the middle plates to the skirts
% Calculating the outer circumference of the diagonal plates [m]
C_o_diagonalskirts = 0.25*(2*L_plate_diagonalskirts + ...
    2*(L_plate_diagonalskirts+(2*t_plates)));
% Calculating the inner circumference of the diagonal plates [m]
C_i_diagonalskirts = 0.25*(2*L_plate_diagonalskirts + ...
    2*(L_plate_diagonalskirts-(2*t_plates)));
% Calculating the average circumference of the diagonal plates [m]
C_av_diagonalskirts = 0.25*((C_o_diagonalskirts+C_i_diagonalskirts)/2);

%-----
% Calculating the remaining parameters of the plates and the system
%-----

% Calculation of parameters of the plates
% Volume calculation of the skirts considered for 1 caisson [m^3]
Vol_tot_plates = (4*(L_plate_outerskirts*H_plates*t_plates)) + ...
    (4*(L_plate_innerskirts*H_plates*t_plates))+...
    (4*(L_plate_diagonalskirts*H_plates*t_plates));
% Weight calculation of the skirt [kg]
Weight_plates = Vol_tot_plates*rho_mat;
% Vertical load due to the weight of the plate [N]
WeightForce_plates = Weight_plates*gravity;
% Buoyancy force of the submerged plate [N]
Fbuoy_plates = Vol_tot_plates*rho_wat*gravity;
% Volume calculation of the platform plate [m^3]
Vol_plate_platform = (L_plate_platform*W_plate_platform)*t_plate_platform;
% Weight calculation of the platform plate [kg]
Weight_plate_platform = Vol_plate_platform*rho_mat;
% Vertical load due to the weight of the platform plate [N]
WeightForce_platform = Weight_plate_platform*gravity;
% Buoyancy force of the submerged platform plate [N]
Fbuoy_platform = Vol_plate_platform*rho_wat*gravity;

% Calculation of the reservoir weight
Reservoir_weight = Total_system_Weight-Weight_plate_platform-...
    Weight_plates-(4*Weight_SC);
Reservoir_weight_force = Reservoir_weight*9.81;
Fbouy_Reservoir = (Reservoir_weight/rho_mat)*rho_wat*gravity;

```

```

% Calculation of total forces
% Total Vertical load [N]
WeightForce_total = WeightForce_SC + 0.25*WeightForce_plates + ...
    0.25*WeightForce_platform + 0.25*Reservoir_weight_force;
% Total buoyancy load [N]
Fbuoy_total = Fbuoy_SC + 0.25*Fbuoy_plates + ...
    0.25*Fbuoy_platform + 0.25*Fbouy_Reservoir;

%-----
% Calculating the parameters of square caisson
%-----

% Calculating the area of the square caisson
A_SQ_inner = L_plate_innerskirts*(L_plate_innerskirts - (2*t_plates));
A_SQ_outer = L_plate_innerskirts*(L_plate_innerskirts + (2*t_plates));
A_SQ_tip = (A_SQ_inner-A_SQ_outer);

%-----
% Calculating the parameters of trapezoidal caissons
%-----

% Calculating dimensions of the trapezoidal shapes
h_trap = sqrt(((L_plate_diagonalskirts)^2-((L_plate_outerskirts - ...
    L_plate_innerskirts)/2)^2);
h_rect = (L_plate_platform/2)-(L_plate_innerskirts/2)-h_trap;
angle_skirtcaisson = 45; %degrees

% Calculating the areas of the trapezoidal shapes
A_circsegouter = 0.5*(((pi/180)*angle_skirtcaisson)-sind ...
    (angle_skirtcaisson))*((D_inner/2)^2);
A_circseginner = 0.5*(((pi/180)*angle_skirtcaisson)-sind ...
    (angle_skirtcaisson))*((D_outer/2)^2);

A_trap_outer = ((L_plate_outerskirts+L_plate_innerskirts)/2)*h_trap;
A_rect_outer = (L_plate_outerskirts*h_rect)-(2*A_circseginner);
A_outer_trapC = A_trap_outer + A_rect_outer;

A_trap_inner = (((L_plate_outerskirts-2*t_plates)+...
    (L_plate_innerskirts-2*t_plates))/2)*(h_trap-t_plates);
A_rect_inner = ((L_plate_outerskirts-2*t_plates)*(h_rect-t_plates))...
    -(2*A_circsegouter);
A_inner_trapC = A_trap_inner + A_rect_inner;

% Calculating the circumferences of the trapezoidal shapes
arc_inner = (angle_skirtcaisson/360)*2*pi*(D_outer/2);
arc_outer = (angle_skirtcaisson/360)*2*pi*(D_inner/2);

C_outer_trap = L_plate_outerskirts+(2*arc_outer)+(2*...
    L_plate_diagonalskirts)+L_plate_innerskirts;
C_inner_trap = (L_plate_outerskirts-2*t_plates)+(2*arc_inner)+(2*...

```

```

        (L_plate_diagonalskirts-2*t_plates))+ (L_plate_innerskirts-2*t_plates);
C_av_trap = (C_outer_trap + C_inner_trap)/2;

% Specifying the equations that need to be solved.
if indx == 1 || indx == 2 || indx == 3 || indx == 4;
%% Calculations for the self weight penetration depth (h_Self_Weight)

%-----
% Calculating the Self-Weight penetration phase (Cohesionless case)
%-----

Z_inner_SW = (D_inner)/(4*Ktandelta);
Z_outer_SW = ((D_outer)*((m_SW^2)-1))/(4*Ktandelta);

% The next while loop is based on the equations given by Houlsby and Byrne.
% Behind every equation an explanation is given. The obtained self weight
% penetration depth will be used in a for loop to determine all the
% resistances.

% Initializing the values for all intermediate steps
Q_outer_SW = 0;
Q_inner_SW = 0;
Q_tip_SW = 0;
h_Self_Weight = 0;
Qtot_SW = 0;

while Qtot_SW < WeightForce_total;
% Updating the depth for every step of the loop [m]
h_Self_Weight= h_Self_Weight+0.00000001;

%% If the plates not reach the seabed in the first phase
if h_Self_Weight < (H_split)
Q_outer_plates_SW = 0;
Q_inner_plates_SW = 0;
Q_tip_plates_SW = 0;

% Calculating the inner and outer resistance forces

% Calculating the outer resistance force [N]
Q_outer_SW = y_komma*(Z_outer_SW^2)*((exp(h_Self_Weight/Z_outer_SW))...
-1-(h_Self_Weight/Z_outer_SW))*(Ktandelta*pi*D_outer);
% Calculating the inner resistance force [N]
Q_inner_SW = y_komma*(Z_inner_SW^2)*((exp(h_Self_Weight/Z_inner_SW))...
-1-(h_Self_Weight/Z_inner_SW))*(Ktandelta*pi*D_inner);

% Calculating the stresses in order to set the end term
% Determining the stress at the inside of the caisson [MPa]
sigma_vikom = y_komma*Z_inner_SW*((exp(h_Self_Weight/Z_inner_SW))-1);
% Determining the stress at the outside of the caisson [MPa]
sigma_vokom = y_komma*Z_outer_SW*((exp(h_Self_Weight/Z_outer_SW))-1);
% Factor for the inequality

```

```

Fac = (2*t*Ny)/Nq;
% Specification of the variable x
x = (t/2)+(((sigma_vokom - sigma_vikom)*Nq)/(4*y_komma*Ny));
% Initialization of sigma_end
sigma_end = 0;

if (sigma_vikom-sigma_vikom) < Fac
    sigma_end = sigma_vokom*Nq + y_komma*(t-((2*(x^2))/t))*Ny;
else
    sigma_end = sigma_vokom*Nq + y_komma*t*Ny;
end

% Calculating the resistance forces at the tips and the total
% resistance force
% Calculation of the resistance force at the tip [N]
Q_tip_SW = sigma_end*pi*D_av*t;
% Calculating the total resistance force [N]
Qtot_SW = Q_outer_SW + Q_inner_SW + Q_tip_SW + Q_outer_plates_SW + ...
    Q_inner_plates_SW + Q_tip_plates_SW + Fbuoy_total;

%%% If the plates reach the seabed in the first phase. The same
%%% approach is used as before.

else
% Calculating the inner and outer resistance forces
Q_outer_SW = y_komma*(Z_outer_SW^2)*((exp(h_Self_Weight/Z_outer_SW))...
    -1-(h_Self_Weight/Z_outer_SW))*(Ktandelta*pi*D_outer);
Q_inner_SW = y_komma*(Z_inner_SW^2)*((exp(h_Self_Weight/Z_inner_SW))...
    -1-(h_Self_Weight/Z_inner_SW))*(Ktandelta*pi*D_inner);

% Calculating the stresses in order to set the end term
sigma_vikom = y_komma*Z_inner_SW*((exp(h_Self_Weight/Z_inner_SW))-1);
sigma_vokom = y_komma*Z_outer_SW*((exp(h_Self_Weight/Z_outer_SW))-1);
Fac = (2*t*Ny)/Nq;
x = (t/2)+(((sigma_vokom - sigma_vikom)*Nq)/(4*y_komma*Ny));
sigma_end = 0;

if (sigma_vikom-sigma_vikom) < Fac
    sigma_end = sigma_vokom*Nq + y_komma*(t-((2*(x^2))/t))*Ny;
else
    sigma_end = sigma_vokom*Nq + y_komma*t*Ny;
end

% Calculating the resistance forces at the tips and the total
% resistance force
% Calculation of the resistance force at the tip [N]
Q_tip_SW = sigma_end*pi*D_av*t;

% Calculating the frictional terms of the plates combined
Q_outer_plates_SW = ((y_komma*((h_Self_Weight-H_split))^2)/2)*...
    Ktandelta*(C_o_outerskirts + C_o_innerskirts + C_o_diagonalskirts);

```

```

Q_inner_plates_SW = ((y_komma*((h_Self_Weight-H_split))^2)/2)*...
    Ktandelta*(C_i_outerskirts + C_i_innerskirts + C_i_diagonalskirts);
Q_tip_plates_SW = ((y_komma*(h_Self_Weight-H_split)*Nq)+...
    (y_komma*(t_plates/2)*Ny))*((C_av_outerskirts+C_av_innerskirts...
    +C_av_diagonalskirts)*t_plates);

% Calculating the total resistance force [N]
Qtot_SW = Q_outer_SW + Q_inner_SW + Q_tip_SW + Q_outer_plates_SW + ...
    Q_inner_plates_SW + Q_tip_plates_SW + Fbuoy_total;
end
end

%% For loop for the Self-Weight penetration to determine force per depth
%Initializing all arrays, to be able to store the data.
h_depth = [0:0.00001:h_Self_Weight];

for i = 1:length(h_depth)
%% If the plates not reach the seabed in the first phase
if h_depth < (H_split)
V_Q_outer_plates_SW(i) = 0;
V_Q_inner_plates_SW(i) = 0;
V_Q_tip_plates_SW(i) = 0;

% Calculating the inner and outer resistance forces [N]
V_Q_outer_SW(i) = y_komma*(Z_outer_SW^2)*((exp((h_depth(i)/Z_outer_SW)))...
    -1-(h_depth(i)/Z_outer_SW))*(Ktandelta*pi*D_outer);
V_Q_inner_SW(i) = y_komma*(Z_inner_SW^2)*((exp(h_depth(i)/Z_inner_SW))...
    -1-(h_depth(i)/Z_inner_SW))*(Ktandelta*pi*D_inner);

% Calculating the stresses at the inside and outside of the caisson [MPa]
V_sigma_vikom(i) = y_komma*Z_inner_SW*((exp(h_depth(i)/Z_inner_SW))-1);
V_sigma_vokom(i) = y_komma*Z_outer_SW*((exp(h_depth(i)/Z_outer_SW))-1);

Fac = (2*t*Ny)/Nq;
V_x(i) = (t/2)+(((V_sigma_vokom(i) - V_sigma_vikom(i))*Nq)/(4*y_komma*Ny));
V_sigma_end(i) = 0;

% Checking the stresses against the inequality factor
if (V_sigma_vikom(i)-V_sigma_vokom(i)) < Fac

V_sigma_end(i) = V_sigma_vokom(i)*Nq + y_komma*(t-((2*(V_x(i)^2))/t))*Ny;
else
V_sigma_end(i) = V_sigma_vokom(i)*Nq + y_komma*t*Ny;
end

% Calculating the resistance force at the tip and the total upward forces [N].
V_Q_tip_SW(i) = V_sigma_end(i)*pi*D_av*t;
V_Qtot_SW(i) = V_Q_outer_SW(i) + V_Q_inner_SW(i) + V_Q_tip_SW(i) + ...
    V_Q_outer_plates_SW(i) + V_Q_inner_plates_SW(i) + ...
    V_Q_tip_plates_SW(i) + Fbuoy_total;

```

```

% Holding Capacity Cylindrical Caisson
R_sos_SW(i) = ((y_komma*h_depth(i))/2)*Ktandelta*pi*D_av*h_depth(i);
R_sis_SW(i) = R_sos_SW(i);
W_c_SW(i) = WeightForce_total;
W_s_SW(i) = (((pi*(D_outer)^2)/4)*h_depth(i))*(y_komma);

H_c_SW(i) = R_sos_SW(i)+R_sis_SW(i)+W_c_SW(i)+W_s_SW(i);
H_c2_SW(i) = H_c_SW(i)/1000;

% Holding Capacity Square Caisson
H_c2_SQ_SW(i) = 0;

% Holding Capacity Trapezoidal Caisson
H_c2_trap_SW(i) = 0;

%% If the plates reach the seabed in the first phase
else

% Calculating the inner and outer resistance forces [N]
V_Q_outer_SW(i) = y_komma*(Z_outer_SW^2)*((exp((h_depth(i)/Z_outer_SW)))-1-(h_depth(i)/Z_outer_SW))*(Ktandelta*pi*D_outer);
V_Q_inner_SW(i) = y_komma*(Z_inner_SW^2)*((exp(h_depth(i)/Z_inner_SW)))-1-(h_depth(i)/Z_inner_SW))*(Ktandelta*pi*D_inner);

% Calculating the stresses at the inside and outside of the caisson [MPa]
V_sigma_vikom(i) = y_komma*Z_inner_SW*((exp(h_depth(i)/Z_inner_SW))-1);
V_sigma_vokom(i) = y_komma*Z_outer_SW*((exp(h_depth(i)/Z_outer_SW))-1);

Fac = (2*t*Ny)/Nq;
V_x(i) = (t/2)+(((V_sigma_vokom(i) - V_sigma_vikom(i))*Nq)/(4*y_komma*Ny));
V_sigma_end(i) = 0;

% Checking the stresses against the inequality factor
if (V_sigma_vikom(i)-V_sigma_vokom(i)) < Fac

V_sigma_end(i) = V_sigma_vokom(i)*Nq + y_komma*(t-((2*(V_x(i)^2))/t))*Ny;
else
V_sigma_end(i) = V_sigma_vokom(i)*Nq + y_komma*t*Ny;
end

% Calculating the resistance force at the tip and the total upward forces [N].
V_Q_tip_SW(i) = V_sigma_end(i)*pi*D_av*t;

% Calculating the frictional terms of the plates combined
V_Q_outer_plates_SW(i) = ((y_komma*((h_depth(i)-H_split))^2)/2)*...
    Ktandelta*(C_o_outerskirts + C_o_innerskirts + C_o_diagonalskirts);
V_Q_inner_plates_SW(i) = ((y_komma*((h_depth(i)-H_split))^2)/2)*...
    Ktandelta*(C_i_outerskirts + C_i_innerskirts + C_i_diagonalskirts);
V_Q_tip_plates_SW(i) = ((y_komma*(h_depth(i)-H_split)*Nq)+...
    (y_komma*(t_plates/2)*Ny))*((C_av_outerskirts+C_av_innerskirts+...
    C_av_diagonalskirts)*t_plates);

```



```

V_Qtot_SW(i) = V_Q_outer_SW(i) + V_Q_inner_SW(i) + V_Q_tip_SW(i) + ...
    V_Q_outer_plates_SW(i) + V_Q_inner_plates_SW(i) + ...
    V_Q_tip_plates_SW(i) + Fbuoy_total;

% Holding Capacity Cylindrical Caisson
R_sos_SW(i) = ((y_komma*h_depth(i))/2)*Ktandelta*pi*D_av*h_depth(i);
R_sis_SW(i) = R_sos_SW(i);
W_c_SW(i) = (4*WeightForce_total)/9;
W_s_SW(i) = (((pi*(D_outer)^2)/4)*h_depth(i))*(y_komma);

% Holding Capacity Square Caisson
R_sos_SQ_SW(i) = ((y_komma*(h_depth(i)-H_split))/2)*Ktandelta*...
    (4*C_av_innerskirts)*(h_depth(i)-H_split);
R_sis_SQ_SW(i) = R_sos_SQ_SW(i);
W_c_SQ_SW(i) = (4*WeightForce_total)/9;
W_s_SQ_SW(i) = (A_SQ_outer)*(h_depth(i)-H_split)*(y_komma);

H_c_SQ_SW(i) = R_sos_SQ_SW(i)+R_sis_SQ_SW(i)+W_c_SQ_SW(i)+W_s_SQ_SW(i);
H_c2_SQ_SW(i) = H_c_SQ_SW(i)/1000;

% Holding Capacity Trapezoidal Caisson
R_sos_trap_SW(i) = ((y_komma*(h_depth(i)-H_split))/2)*Ktandelta*...
    (C_av_trap)*(h_depth(i)-H_split);
R_sis_trap_SW(i) = R_sos_trap_SW(i);
W_c_trap_SW(i) = (4*WeightForce_total)/9;
W_s_trap_SW(i) = (A_inner_trapC)*(h_depth(i)-H_split)*(y_komma);

H_c_trap_SW(i) = R_sos_trap_SW(i)+R_sis_trap_SW(i)+W_c_trap_SW(i)+...
    W_s_trap_SW(i);
H_c2_trap_SW(i) = H_c_trap_SW(i)/1000;
end

end

%% Parameters for suction assisted penetration phase

%-----
% Calculating the Suction Assisted penetration phase (Cohesionless case)
%-----

c_0 = 0.45;          % coefficient 1 for term a1 (Houlsby & Byrne)
c_1 = 0.36;          % coefficient 2 for term a1 (Houlsby & Byrne)
c_2 = 0.48;          % coefficient 3 for term a1 (Houlsby & Byrne)

% Calculation of flow factor parameters (a and a1)
% maximum penetration depth of the suction caisson [m]
h_max = H_inner;
a1 = c_0 - c_1*(1-exp((-1)*(h_max/(c_2*D_av))));
% Flow factor form outside to inside of the caisson [-]
a = (a1*k_f)/((1-a1)+a1*k_f);

```

```

%% Calculation of the maximum suction to be applied for 0.5m penetration
% Multiple of the diameter for enhanced stress [-] (A. Altarriba)
m_SA = 1.5;

Z_inner_SA = (D_inner)/(4*Ktandelta);
Z_outer_SA = ((D_outer)*((m_SA^2)-1))/(4*Ktandelta);

%% For loop for the Suction Assisted penetration to determine force per depth
h_depth_SA = [h_Self_Weight:0.001:h_max];

for i = 1:length(h_depth_SA)
% Initializing for the flow factors
a1_SA(i) = c_0 - c_1*(1-(exp((-1)*(h_depth_SA(i)/(c_2*D_av)))));
a_SA(i) = (a1_SA(i)*k_f)/((1-a1_SA(i))+a1_SA(i)*k_f);
a2_SA = 0.5;

% Calculating the critical suction
s_crit(i) = (y_komma*h_depth_SA(i))/(1-a_SA(i));

if h_depth_SA(i) < (H_split)
% Part where the plate does not yet reach the seabed
% Initializing the factors as done in the maximization before
V_x1(i) = ((Z_outer_SA)^2)*((exp(h_depth_SA(i)/Z_outer_SA))-1-...
    (h_depth_SA(i)/Z_outer_SA))*(Ktandelta)*(pi*D_outer);
V_x2(i) = ((Z_inner_SA)^2)*((exp(h_depth_SA(i)/Z_inner_SA))-1-...
    (h_depth_SA(i)/Z_inner_SA))*(Ktandelta)*(pi*D_inner);
V_x3(i) = (Z_inner_SA*((exp(h_depth_SA(i)/Z_inner_SA))-1)*Nq);
V_x4(i) = (y_komma*t*Ny);
V_x5(i) = (pi*D_av*t);
V_x6(i) = ((pi*(D_inner^2))/4);

% Initializing the friction forces at the plate
V_outer_plates(i) = 0;
V_inner_plates(i) = 0;
V_tip_plates(i) = 0;

% Calculating the variable s [Pa]
syms p2
eqn = p2*(V_x6(i)) + WeightForce_total == (y_komma + ((a_SA(i)*p2)/...
    h_depth_SA(i)))*V_x1(i) + (y_komma - (((1-a_SA(i))*p2)/h_depth_SA(i)))...
    *V_x2(i)+ (((y_komma - (((1-a_SA(i))*p2)/h_depth_SA(i)))*V_x3(i))+...
    V_x4(i))*V_x5(i)) + V_outer_plates(i)+ V_inner_plates(i)+...
    V_tip_plates(i) + Fbuoy_total;

s2(i) = double (solve(eqn,p2));

% Calculating the forces acting within the system
V_Force_SA(i) = WeightForce_total + s2(i)*(V_x6(i));
V_Q_outer_SA(i) = (y_komma + ((a_SA(i)*s2(i))/h_depth_SA(i)))*V_x1(i);
V_Q_inner_SA(i) = (y_komma - (((1-a_SA(i))*s2(i))/h_depth_SA(i)))*V_x2(i);

```

```

V_Q_tip_SA(i) = (((y_komma - (((1-a_SA(i))*s2(i))/h_depth_SA(i)))...
    *V_x3(i))+V_x4(i))*V_x5(i));
V_Qtot_SA(i) = V_Q_outer_SA(i) + V_Q_inner_SA(i) + V_Q_tip_SA(i) ...
    + V_outer_plates(i) + V_inner_plates(i) + V_tip_plates(i)...
    + Fbuoy_total;

% Holding Capacity Cylindrical Caisson
R_sos_SA(i) = ((y_komma*h_depth_SA(i))/2)*Ktandelta*pi*D_av*h_depth_SA(i);
R_sis_SA(i) = R_sos_SA(i);
W_c_SA(i) = WeightForce_total;
W_s_SA(i) = (((pi*(D_outer)^2)/4)*h_depth_SA(i))*(y_komma);

H_c_SA(i) = R_sos_SA(i)+R_sis_SA(i)+W_c_SA(i)+W_s_SA(i);
H_c2_SA(i) = H_c_SA(i)/1000;
H_c2_SQ_SA(i) =0;
H_c2_trap_SA(i) =0;

else
% Part where the plate does reach the seabed

% Initializing the factors as done in the maximization before
V_x1(i) = ((Z_outer_SA)^2)*((exp(h_depth_SA(i)/Z_outer_SA))-1-...
    (h_depth_SA(i)/Z_outer_SA))*(Ktandelta)*(pi*D_outer);
V_x2(i) = ((Z_inner_SA)^2)*((exp(h_depth_SA(i)/Z_inner_SA))-1-...
    (h_depth_SA(i)/Z_inner_SA))*(Ktandelta)*(pi*D_inner);
V_x3(i) = (Z_inner_SA)*((exp(h_depth_SA(i)/Z_inner_SA))-1)*Nq;
V_x4(i) = (y_komma*t*Ny);
V_x5(i) = (pi*D_av*t);
V_x6(i) = ((pi*(D_inner^2))/4);

% Calculating the friction terms for the plate
V_outer_plates(i) = ((y_komma*((h_depth_SA(i)-H_split))^2)/2)*Ktandelta*...
    (C_o_outerskirts+C_o_innerskirts+C_o_diagonalskirts);
V_inner_plates(i) = ((y_komma*((h_depth_SA(i)-H_split))^2)/2)*Ktandelta*...
    (C_i_outerskirts+C_i_innerskirts+C_i_diagonalskirts);
V_tip_plates(i) = ((y_komma*(h_depth_SA(i)-H_split)*Nq)+(y_komma*...
    (t_plates/2)*Ny))*((C_av_outerskirts+C_av_innerskirts+...
    C_av_diagonalskirts)*t_plates);

% Calculating the variable s [Pa]
syms p2
eqn = p2*(V_x6(i)) + WeightForce_total == (y_komma + ((a_SA(i)*p2)/...
    h_depth_SA(i)))*V_x1(i) + (y_komma - (((1-a_SA(i))*p2)/...
    h_depth_SA(i)))*V_x2(i)+ (((y_komma - (((1-a_SA(i))*p2)/...
    h_depth_SA(i)))*V_x3(i))+V_x4(i))*V_x5(i)) + V_outer_plates(i) ...
    + V_inner_plates(i) + V_tip_plates(i) + Fbuoy_total;

s2(i) = double (solve(eqn,p2));

% Calculating the forces acting within the system
V_Force_SA(i) = WeightForce_total + s2(i)*(V_x6(i));

```

```

V_Q_outer_SA(i) = (y_komma + ((a_SA(i)*s2(i))/h_depth_SA(i)))*V_x1(i);
V_Q_inner_SA(i) = (y_komma - (((1-a_SA(i))*s2(i))/h_depth_SA(i)))*V_x2(i);
V_Q_tip_SA(i) = (((y_komma - (((1-a_SA(i))*s2(i))/h_depth_SA(i)))*...
    *V_x3(i))+V_x4(i))*V_x5(i);
V_Qtot_SA(i) = V_Q_outer_SA(i) + V_Q_inner_SA(i) + V_Q_tip_SA(i)...
    +V_outer_plates(i)+ V_inner_plates(i)+ V_tip_plates(i)+ Fbuoy_total;

% Holding Capacity Cylindrical Caisson
R_sos_SA(i) = ((y_komma*h_depth_SA(i))/2)*Ktandelta*pi*D_av*h_depth_SA(i);
R_sis_SA(i) = R_sos_SA(i);
W_c_SA(i) = (4*WeightForce_total)/9;
W_s_SA(i) = (((pi*(D_outer)^2)/4)*h_depth_SA(i))*(y_komma);

H_c_SA(i) = R_sos_SA(i)+R_sis_SA(i)+W_c_SA(i)+W_s_SA(i);
H_c2_SA(i) = H_c_SA(i)/1000;

% Holding Capacity Square Caisson
R_sos_SQ_SA(i) = ((y_komma*(h_depth_SA(i)-H_split))/2)*Ktandelta*...
    (4*C_av_innerskirts)*(h_depth_SA(i)-H_split);
R_sis_SQ_SA(i) = R_sos_SQ_SA(i);
W_c_SQ_SA(i) = (4*WeightForce_total)/9;
W_s_SQ_SA(i) = (A_SQ_outer)*(h_depth_SA(i)-H_split)*(y_komma);

H_c_SQ_SA(i) = R_sos_SQ_SA(i)+R_sis_SQ_SA(i)+W_c_SQ_SA(i)+W_s_SQ_SA(i);
H_c2_SQ_SA(i) = H_c_SQ_SA(i)/1000;

% Holding Capacity Trapezoidal Caisson
R_sos_trap_SA(i) = ((y_komma*(h_depth_SA(i)-H_split))/2)*Ktandelta*...
    (C_av_trap)*(h_depth_SA(i)-H_split);
R_sis_trap_SA(i) = R_sos_trap_SA(i);
W_c_trap_SA(i) = (4*WeightForce_total)/9;
W_s_trap_SA(i) = (A_inner_trapC)*(h_depth_SA(i)-H_split)*(y_komma);

H_c_trap_SA(i) = R_sos_trap_SA(i)+R_sis_trap_SA(i)+W_c_trap_SA(i)+...
    W_s_trap_SA(i);
H_c2_trap_SA(i) = H_c_trap_SA(i)/1000;

% Testing the suction against the critical suction, to determine if
% the square chamber is necessary
if s2(i) < s_crit(i)
    s2(i) = s2(i);
else
% Determining the multiple of the area
Am_SQ_outer = m_SA*A_SQ_outer;

Z_inner_SQ = (A_SQ_inner/(Ktandelta*(4*C_i_innerskirts)));
Z_outer_SQ = ((Am_SQ_outer-A_SQ_outer)/(Ktandelta*(4*C_o_innerskirts)));

% Setting the factors for the round caisson
V_x1(i) = ((Z_outer_SA)^2)*((exp(h_depth_SA(i)/Z_outer_SA))-1-...
    (h_depth_SA(i)/Z_outer_SA))*(Ktandelta)*(pi*D_outer);

```

```

V_x2(i) = ((Z_inner_SA)^2)*((exp(h_depth_SA(i)/Z_inner_SA))-1-...
    (h_depth_SA(i)/Z_inner_SA))*(Ktandelta)*(pi*D_inner);
V_x3(i) = (Z_inner_SA*((exp(h_depth_SA(i)/Z_inner_SA))-1)*Nq);
V_x4(i) = (y_komma*t*Ny);
V_x5(i) = (pi*D_av*t);
V_x6(i) = ((pi*(D_inner^2))/4);

% Same factors as for the round suction caisson, but
% determined for the square one
V_x7(i) = ((Z_outer_SQ)^2)*((exp((h_depth_SA(i)-H_split)/Z_outer_SQ))...
    -1-((h_depth_SA(i)-H_split)/Z_outer_SQ))*(Ktandelta)*...
    (4*(C_o_innerskirts));
V_x8(i) = ((Z_inner_SQ)^2)*((exp((h_depth_SA(i)-H_split)/Z_inner_SQ))...
    -1-((h_depth_SA(i)-H_split)/Z_inner_SQ))*(Ktandelta)*...
    (4*(C_i_innerskirts));
V_x9(i) = (Z_inner_SQ*((exp((h_depth_SA(i)-H_split)/Z_inner_SQ))-1)*Nq);
V_x10(i) = (y_komma*t_plates*Ny);
V_x11(i) = (A_SQ_outer-A_SQ_inner);
V_x12(i) = A_SQ_inner;

% The plating for that is not used as a caisson is now
% determined for a full system instead of a quarter
V_outer_plates(i) = ((y_komma*((h_depth_SA(i)-H_split))^2)/2)*Ktandelta*...
    ((4*C_o_outerskirts)+(4*C_o_diagonalskirts));
V_inner_plates(i) = ((y_komma*((h_depth_SA(i)-H_split))^2)/2)*Ktandelta*...
    ((4*C_i_outerskirts)+(4*C_i_diagonalskirts));
V_tip_plates(i) = ((y_komma*(h_depth_SA(i)-H_split)*Nq)+(y_komma*...
    (t_plates/2)*Ny))*(((4*C_av_outerskirts)+(4*C_av_diagonalskirts))...
    *t_plates);

% Calculating the new variable s [Pa], based on the full system
% In this equation, the additional terms for the square
% caisson are taken into account
syms p2
eqn = (p2*V_x12(i)) + 4*(p2*(V_x6(i))) + 4*(WeightForce_total) == 4*...
    ((y_komma + ((a_SA(i)*p2)/h_depth_SA(i)))*V_x1(i) + (y_komma - ...
    (((1-a_SA(i))*p2)/h_depth_SA(i)))*V_x2(i) ...
    + (((y_komma - (((1-a_SA(i))*p2)/h_depth_SA(i)))*V_x3(i))+V_x4(i))...
    *V_x5(i)) + V_outer_plates(i) + ...
    ((y_komma + ((a2_SA*p2)/(h_depth_SA(i)-H_split)))*V_x7(i) + ...
    (y_komma - (((1-a2_SA)*p2)/(h_depth_SA(i)-H_split)))*V_x8(i) + ...
    (((y_komma - (((1-a2_SA)*p2)/(h_depth_SA(i)-H_split)))*V_x9(i))...
    +V_x10(i))*V_x11(i))+ V_tip_plates(i) + V_inner_plates(i)...
    + 4*(Fbuoy_total);

s2(i) = double (solve(eqn,p2));

V_Force_SA(i) = WeightForce_total + s2(i)*(V_x6(i));
V_Q_outer_SA(i) = (y_komma + ((a_SA(i)*(s2(i)))/h_depth_SA(i)))*V_x1(i);
V_Q_inner_SA(i) = (y_komma - (((1-a_SA(i))*(s2(i)))/h_depth_SA(i)))*V_x2(i);
V_Q_tip_SA(i) = (((y_komma - (((1-a_SA(i))*(s2(i)))/h_depth_SA(i)))*...

```

```

*V_x3(i))+V_x4(i))*V_x5(i));

% Calculating the terms for the square suction caisson
V_Q_outer_SA_SQ(i) = (y_komma + ((a2_SA*(s2(i)))/(h_depth_SA(i)...
-H_split)))*V_x7(i);
V_Q_inner_SA_SQ(i) = (y_komma - (((1-a2_SA)*(s2(i)))/(h_depth_SA(i) - ...
H_split)))*V_x8(i);
V_Q_tip_SA_SQ(i) = (((y_komma - (((1-a2_SA)*(s2(i)))/(h_depth_SA(i) - ...
H_split)))*V_x9(i))+V_x10(i))*V_x11(i));

% Calculating the total frictional forces
V_Qtot_SA(i) = V_Q_outer_SA(i) + V_Q_inner_SA(i) + V_Q_tip_SA(i)...
+ V_outer_plates(i) + V_Q_outer_SA_SQ(i) + V_Q_inner_SA_SQ(i) + ...
V_Q_tip_SA_SQ(i) + V_inner_plates(i) + V_tip_plates(i) + 4*Fbuoy_total;

% Holding Capacity Cylindrical Caisson
R_sos_SA(i) = ((y_komma*h_depth_SA(i))/2)*Ktandelta*pi*D_av*h_depth_SA(i);
R_sis_SA(i) = R_sos_SA(i);
W_c_SA(i) = (4*WeightForce_total)/9;
W_s_SA(i) = (((pi*(D_outer)^2)/4)*h_depth_SA(i))*(y_komma);

H_c_SA(i) = R_sos_SA(i)+R_sis_SA(i)+W_c_SA(i)+W_s_SA(i);
H_c2_SA(i) = H_c_SA(i)/1000;

% Holding Capacity Square Caisson
R_sos_SQ_SA(i) = ((y_komma*(h_depth_SA(i)-H_split))/2)*Ktandelta*...
(4*C_av_innerskirts)*(h_depth_SA(i)-H_split);
R_sis_SQ_SA(i) = R_sos_SQ_SA(i);
W_c_SQ_SA(i) = (4*WeightForce_total)/9;
W_s_SQ_SA(i) = (A_SQ_outer)*(h_depth_SA(i)-H_split)*(y_komma);

H_c_SQ_SA(i) = R_sos_SQ_SA(i)+R_sis_SQ_SA(i)+W_c_SQ_SA(i)+W_s_SQ_SA(i);
H_c2_SQ_SA(i) = H_c_SQ_SA(i)/1000;

% Holding Capacity Trapezoidal Caisson
R_sos_trap_SA(i) = ((y_komma*(h_depth_SA(i)-H_split))/2)*Ktandelta*...
(C_av_trap)*(h_depth_SA(i)-H_split);
R_sis_trap_SA(i) = R_sos_trap_SA(i);
W_c_trap_SA(i) = (4*WeightForce_total)/9;
W_s_trap_SA(i) = (A_inner_trapC)*(h_depth_SA(i)-H_split)*(y_komma);

H_c_trap_SA(i) = R_sos_trap_SA(i)+R_sis_trap_SA(i)+W_c_trap_SA(i)+...
W_s_trap_SA(i);
H_c2_trap_SA(i) = H_c_trap_SA(i)/1000;
end

% If the suction still is larger than the critical suction, the
% trapezoidal caissons are added.

if s2(i) < s_crit(i)
    s2(i) = s2(i);

```

```

else
% Determining the multiple of the area
Am_trap_outer = m_SA*A_outer_trapC;

Z_inner_trap = (A_inner_trapC/(Ktandelta*C_inner_trap));
Z_outer_trap = ((Am_trap_outer-A_outer_trapC)/(Ktandelta*C_outer_trap));

% Setting the factors for the round caisson
V_x1(i) = ((Z_outer_SA)^2)*((exp(h_depth_SA(i)/Z_outer_SA))-1-...
    (h_depth_SA(i)/Z_outer_SA))*(Ktandelta)*(pi*D_outer);
V_x2(i) = ((Z_inner_SA)^2)*((exp(h_depth_SA(i)/Z_inner_SA))-1-...
    (h_depth_SA(i)/Z_inner_SA))*(Ktandelta)*(pi*D_inner);
V_x3(i) = (Z_inner_SA*((exp(h_depth_SA(i)/Z_inner_SA))-1)*Nq);
V_x4(i) = (y_komma*t*Ny);
V_x5(i) = (pi*D_av*t);
V_x6(i) = ((pi*(D_inner^2))/4);

% Same factors as for the round suction caisson , but
% determined for the square one
V_x7(i) = ((Z_outer_SQ)^2)*((exp((h_depth_SA(i)-H_split)/Z_outer_SQ))...
    -1-((h_depth_SA(i)-H_split)/Z_outer_SQ))*(Ktandelta)*...
    (4*(C_o_innerskirts));
V_x8(i) = ((Z_inner_SQ)^2)*((exp((h_depth_SA(i)-H_split)/Z_inner_SQ))...
    -1-((h_depth_SA(i)-H_split)/Z_inner_SQ))*(Ktandelta)*...
    (4*(C_i_innerskirts));
V_x9(i) = (Z_inner_SQ*((exp((h_depth_SA(i)-H_split)/Z_inner_SQ))-1)*Nq);
V_x10(i) = (y_komma*t_plates*Ny);
V_x11(i) = (A_SQ_outer-A_SQ_inner);
V_x12(i) = A_SQ_inner;

% Same factors as for the round caisson , but for the trapezoidal chambers
V_x13(i) = ((Z_outer_trap)^2)*((exp((h_depth_SA(i)-H_split)/Z_outer_trap))...
    -1-((h_depth_SA(i)-H_split)/Z_outer_trap))*(Ktandelta)*C_outer_trap;
V_x14(i) = ((Z_inner_trap)^2)*((exp((h_depth_SA(i)-H_split)/Z_inner_trap))...
    -1-((h_depth_SA(i)-H_split)/Z_inner_trap))*(Ktandelta)*C_inner_trap;
V_x15(i) = (Z_inner_trap*((exp((h_depth_SA(i)-H_split)/Z_inner_trap))-1)*Nq);
V_x16(i) = (y_komma*t_plates*Ny);
V_x17(i) = (A_outer_trapC-A_inner_trapC);
V_x18(i) = A_inner_trapC;

V_outer_plates(i) = 0;
V_inner_plates(i) = 0;
V_tip_plates(i) = 0;

% Calculating the new variable s [Pa], based on the full system
% In this equation, the additional terms for the square and
% trapezoidal caisson are taken into account

```

```
syms p2
```

```

eqn = 4*(p2*V_x18(i)) +(p2*V_x12(i)) + 4*(p2*(V_x6(i))) + 4*...
    (WeightForce_total) == 4*((y_komma + ((a_SA(i)*p2)/h_depth_SA(i)))...
    *V_x1(i) + (y_komma - (((1-a_SA(i))*p2)/h_depth_SA(i))*V_x2(i) ...
    + (((y_komma - (((1-a_SA(i))*p2)/h_depth_SA(i))*V_x3(i))+V_x4(i))...
    *V_x5(i))) +((y_komma + ((a2_SA*p2)/(h_depth_SA(i)-H_split)))*V_x7(i)...
    + (y_komma - (((1-a2_SA)*p2)/(h_depth_SA(i)-H_split)))*V_x8(i) + ...
    (((y_komma - (((1-a2_SA)*p2)/(h_depth_SA(i)-H_split)))*V_x9(i))+...
    V_x10(i))*V_x11(i))+ (4*((y_komma + ((a2_SA*p2)/(h_depth_SA(i)...
    -H_split))*V_x13(i) + (y_komma - (((1-a2_SA)*p2)/(h_depth_SA(i) -...
    H_split))*V_x14(i) +(((y_komma - (((1-a2_SA)*p2)/(h_depth_SA(i)...
    -H_split))*V_x15(i))+V_x16(i))*V_x17(i)))) + 4*(Fbuoy_total);

s2(i) = double (solve(eqn,p2));

V_Force_SA(i) = WeightForce_total + s2(i)*(V_x6(i));
V_Q_outer_SA(i) = (y_komma + ((a_SA(i)*(s2(i)))/h_depth_SA(i))*V_x1(i);
V_Q_inner_SA(i) = (y_komma - (((1-a_SA(i))*(s2(i)))/h_depth_SA(i))*V_x2(i);
V_Q_tip_SA(i) = (((y_komma - (((1-a_SA(i))*(s2(i)))/h_depth_SA(i))...
    *V_x3(i))+V_x4(i))*V_x5(i));

% Calculating the terms for the square suction caisson
V_Q_outer_SA_SQ(i) = (y_komma + ((a2_SA*(s2(i)))/(h_depth_SA(i)...
    -H_split))*V_x7(i);
V_Q_inner_SA_SQ(i) = (y_komma - (((1-a2_SA)*(s2(i)))/(h_depth_SA(i)...
    -H_split))*V_x8(i);
V_Q_tip_SA_SQ(i) = (((y_komma - (((1-a2_SA)*(s2(i)))/(h_depth_SA(i)...
    -H_split))*V_x9(i))+V_x10(i))*V_x11(i));

% Calculating the terms for the trapezoidal suction caissons
V_Q_outer_SA_trap(i) = (y_komma + ((a2_SA*(s2(i)))/(h_depth_SA(i) -...
    H_split))*V_x13(i);
V_Q_inner_SA_trap(i) = (y_komma - (((1-a2_SA)*(s2(i)))/(h_depth_SA(i) -...
    H_split))*V_x14(i);
V_Q_tip_SA_trap(i) = (((y_komma - (((1-a2_SA)*(s2(i)))/(h_depth_SA(i)...
    -H_split))*V_x15(i))+V_x16(i))*V_x17(i));

% Calculating the total frictional forces
V_Qtot_SA(i) = V_Q_outer_SA(i) + V_Q_inner_SA(i) + V_Q_tip_SA(i) +...
    V_Q_outer_SA_trap(i) +V_Q_inner_SA_trap(i) + V_Q_tip_SA_trap(i)+...
    V_Q_outer_SA_SQ(i) + V_Q_inner_SA_SQ(i) + V_Q_tip_SA_SQ(i)...
    + 4*Fbuoy_total;

% Holding Capacity Cylindrical Caisson
R_sos_SA(i) = ((y_komma*h_depth_SA(i))/2)*Ktandelta*pi*D_av*h_depth_SA(i);
R_sis_SA(i) = R_sos_SA(i);
W_c_SA(i) = (4*WeightForce_total)/9;
W_s_SA(i) = (((pi*(D_outer)^2)/4)*h_depth_SA(i))*(y_komma);

H_c_SA(i) = R_sos_SA(i)+R_sis_SA(i)+W_c_SA(i)+W_s_SA(i);
H_c2_SA(i) = H_c_SA(i)/1000;

```



```

% Holding Capacity Square Caisson
R_sos_SQ_SA(i) = ((y_komma*(h_depth_SA(i)-H_split))/2)*Ktandelta*...
    (4*C_av_innerskirts)*(h_depth_SA(i)-H_split);
R_sis_SQ_SA(i) = R_sos_SQ_SA(i);
W_c_SQ_SA(i) = (4*WeightForce_total)/9;
W_s_SQ_SA(i) = (A_SQ_outer)*(h_depth_SA(i)-H_split)*(y_komma);

H_c_SQ_SA(i) = R_sos_SQ_SA(i)+R_sis_SQ_SA(i)+W_c_SQ_SA(i)+W_s_SQ_SA(i);
H_c2_SQ_SA(i) = H_c_SQ_SA(i)/1000;

% Holding Capacity Trapezoidal Caisson
R_sos_trap_SA(i) = ((y_komma*(h_depth_SA(i)-H_split))/2)*Ktandelta*...
    (C_av_trap)*(h_depth_SA(i)-H_split);
R_sis_trap_SA(i) = R_sos_trap_SA(i);
W_c_trap_SA(i) = (4*WeightForce_total)/9;
W_s_trap_SA(i) = (A_inner_trapC)*(h_depth_SA(i)-H_split)*(y_komma);

H_c_trap_SA(i) = R_sos_trap_SA(i)+R_sis_trap_SA(i)+W_c_trap_SA(i)+...
    W_s_trap_SA(i);
H_c2_trap_SA(i) = H_c_trap_SA(i)/1000;
end
end

end

%% Plotting the behaviour of the foundation system

%-----
% Plotting the behaviour of the foundation system for individual phases
% (Cohesionless case)
%-----

figure(1)
plot(h_depth, V_Qtot_SW)
title('Total resistance force during the Selfweight penetration phase')
xlabel('Penetration depth [m]')
ylabel('Total resistance force [N]')

figure(2)
plot(h_depth_SA,s2)
title('Suction required for a total depth of 0.5 m')
xlabel('Penetration depth [m]')
ylabel('Required suction [Pa]')

figure(3)
plot(h_depth_SA,V_Qtot_SA)
title('Total resistance forces during the suction assisted phase')
xlabel('Penetration depth [m]')
ylabel('Total resistance force [N]')

figure(4)

```

```

plot(h_depth_SA,V_Q_tip_SA)
title('Resistance force at the tips during the suction assisted phase')
xlabel('Penetration depth [m]')
ylabel('Resistance force at the tips [N]')

figure(5)
plot(h_depth_SA,V_Q_inner_SA)
title('Resistance force at the inside of the caisson during the suction assisted')
xlabel('Penetration depth [m]')
ylabel('Resistance force at the inside of the caisson [N]')

figure(6)
plot(h_depth_SA,V_Q_outer_SA)
title('Resistance force at the outside of the caisson during the suction assisted')
xlabel('Penetration depth [m]')
ylabel('Resistance force at the outside of the caisson [N]')

figure(7)
plot(h_depth_SA, V_Q_outer_SA)
hold on
plot(h_depth_SA, V_Q_inner_SA)
hold on
plot(h_depth_SA, V_Q_tip_SA)
hold off

title('Resistance forces during the suction assisted penetration phase')
xlabel('Penetration depth [m]')
ylabel('Resistance force [N]')
legend('Outer resistance force', 'Inner resistance force',...
      'Tip resistance force', 'Location', 'Southeast')

%-----
% Plotting the behaviour of the foundation system for all phases
% (Cohesionless case)
%-----

h_tot = [h_depth h_depth_SA];
V_Q_outer_tot = [V_Q_outer_SW V_Q_outer_SA];
V_Q_inner_tot = [V_Q_inner_SW V_Q_inner_SA];
V_Q_tip_tot = [V_Q_tip_SW V_Q_tip_SA];
V_Qtot = [V_Qtot_SW V_Qtot_SA];
H_c2 = [H_c2_SW H_c2_SA];
H_c2_SQ = [H_c2_SQ_SW H_c2_SQ_SA];
H_c2_trap = [H_c2_trap_SW H_c2_trap_SA];

figure(8)
plot(h_tot,V_Qtot)
title('Total resistance force during the installation')
xlabel('Penetration depth [m]')
ylabel('Total resistance force [N]')

```

```

figure(9)
plot(h_tot, V_Q_outer_tot)
hold on
plot(h_tot, V_Q_inner_tot)
hold on
plot(h_tot, V_Q_tip_tot)
hold off

title('Resistance forces over the penetration depth')
xlabel('Penetration depth [m]')
ylabel('Resistance force [N]')
legend('Outer resistance force', 'Inner resistance force', ...
       'Tip resistance force', 'Location', 'Northwest')

figure(10)
plot(h_depth_SA, a_SA)
title('Flow factor "a" over the penetration depth')
xlabel('Penetration depth [m]')
ylabel('Flow factor a [-]')

% critical suction
figure(11)
plot(h_depth_SA, s2)
hold on
plot(h_depth_SA, s_crit)
hold off

title('Calculated suction vs Critical suction ')
xlabel('Penetration depth [m]')
ylabel('Required suction [Pa]')
legend('Suction Houlsby & Byrne', 'Critical Suction', 'Location', 'Northwest')

figure(12)
plot(h_tot, H_c2)
hold on
plot(h_tot, H_c2_SQ)
hold on
plot(h_tot, H_c2_trap)
hold off

title('Holding capacity of one suction caisson')
xlabel('Penetration depth [m]')
ylabel('Holding capacity [kN]')
legend('Circular Caissons', 'Square Caisson', 'Trapezoidal Caisson' , ...
       'Location', 'Northwest')

else
%% Calculations for the self weight penetration depth (h_Self_Weight)
Nq=1; % Due to undrained conditions
f=0.7;
Nc_isk = 9;

```

```

% Calculating the Self-Weight penetration phase (Cohesive case)
%

% Initializing the values for all intermediate steps
Q_outer_SW = 0;
Q_inner_SW = 0;
Q_tip_SW = 0;
h_Self_Weight = 0;
Qtot_SW = 0;

while Qtot_SW < WeightForce_total;
% Updating the depth for every step of the loop [m]
h_Self_Weight = h_Self_Weight + 0.00000001;

%%% If the plates not reach the seabed in the first phase
if h_Self_Weight < (H_split)
Q_outer_plates_SW = 0;
Q_inner_plates_SW = 0;
Q_tip_plates_SW = 0;

% Initializing terms su1 and su2 (undrained shear strengths)
% Calculating the average undrained shear strength between
% mudline and depth h [Pa]
s_u1 = s_u0 + rate_change*(h_Self_Weight/2);
% Calculating the undrained shear strength at depth h [Pa]
s_u2 = s_u0 + rate_change*h_Self_Weight;

% Calculating the resistance forces
Q_outer_SW = h_Self_Weight*alpha*s_u1*(pi*D_outer);
Q_inner_SW = h_Self_Weight*alpha*s_u1*(pi*D_inner);
Q_tip_SW = (y_komma*h_Self_Weight*Nq + s_u2*Nc)*(pi*D_av*t);

Qtot_SW = Q_outer_SW + Q_inner_SW + Q_tip_SW + Q_outer_plates_SW ...
+ Q_inner_plates_SW + Q_tip_plates_SW + Fbuoy_total;

%%% If the plates reach the seabed in the first phase
else
% Initializing terms su1 and su2 (undrained shear strengths)
% Calculating the average undrained shear strength between
% mudline and depth h [Pa]
s_u1 = s_u0 + rate_change*(h_Self_Weight/2);
% Calculating the undrained shear strength at depth h [Pa]
s_u2 = s_u0 + rate_change*h_Self_Weight;

% Calculating the resistance forces
Q_outer_SW = h_Self_Weight*alpha*s_u1*(pi*D_outer);
Q_inner_SW = h_Self_Weight*alpha*s_u1*(pi*D_inner);
Q_tip_SW = (y_komma*h_Self_Weight*Nq + s_u2*Nc)*(pi*D_av*t);

```

```

% Calculating the frictional terms of the plates combined
Q_outer_plates_SW = (h_Self_Weight-H_split)*alpha*s_u1_SA*(C_o_outerskirts...
    + C_o_innerskirts + C_o_diagonalskirts);
Q_inner_plates_SW = (h_Self_Weight-H_split)*alpha*s_u1_SA*(C_i_outerskirts...
    + C_i_innerskirts + C_i_diagonalskirts);
Q_tip_plates_SW = ((y_komma*(h_Self_Weight-H_split)*Nq)+(s_u2_SA*Nc))*...
    ((C_av_outerskirts+C_av_innerskirts+C_av_diagonalskirts)*t_plates);

Qtot_SW = Q_outer_SW + Q_inner_SW + Q_tip_SW + Q_outer_plates_SW ...
    + Q_inner_plates_SW + + Q_tip_plates_SW + Fbuoy_total;
end
end

%% For loop for the Self-Weight penetration to determine force per depth
%Initializing all arrays, to be able to store the data.
h_depth = [0:0.00001:h_Self_Weight];

for i = 1:length(h_depth)
    %%% If the plates not reach the seabed in the first phase
    if h_depth < (H_split)

        V_Q_outer_plates_SW(i) = 0;
        V_Q_inner_plates_SW(i) = 0;
        V_Q_tip_plates_SW(i) = 0;

        % Initializing terms su1 and su2 (undrained shear strengths)
        V_s_u1(i) = s_u0 + rate_change*(h_depth(i)/2);
        V_s_u2(i) = s_u0 + rate_change*h_depth(i);

        % Calculating the resistance forces
        V_Q_outer_SW(i) = h_depth(i)*alpha*V_s_u1(i)*(pi*D_outer);
        V_Q_inner_SW(i) = h_depth(i)*alpha*V_s_u1(i)*(pi*D_inner);
        V_Q_tip_SW(i) = (y_komma*h_depth(i)*Nq + V_s_u2(i)*Nc)*(pi*D_av*t);

        V_Qtot_SW(i) = V_Q_outer_SW(i) + V_Q_inner_SW(i) + V_Q_tip_SW(i) +...
            V_Q_outer_plates_SW(i)+ V_Q_inner_plates_SW(i) +...
            V_Q_tip_plates_SW(i) + Fbuoy_total;

        % Holding Capacity Cylindrical Caisson
        Q_su_SW(i) = alpha*s_u0*pi*D_outer*h_depth(i);
        Q_b_SW(i) = s_u0*Nc_isk*f*((pi*(D_outer)^2)/4);
        W_c_SW(i) = (4*WeightForce_total)/4;
        W_s_SW(i) = (((pi*(D_outer)^2)/4)*h_depth(i))*(y_komma);

        H_c_SW(i) = Q_su_SW(i)+Q_b_SW(i)+W_c_SW(i)+W_s_SW(i);
        H_c2_SW(i) = H_c_SW(i)/1000;

        % Holding Capacity Square Caisson
        H_c2_SQ_SW(i) = 0;

        % Holding Capacity Trapezoidal Caisson

```

```

H_c2_trap_SW(i) = 0;

else
% Part where the plate does reach the seabed
% Initializing terms su1 and su2 (undrained shear strengths)
V_s_u1(i) = s_u0 + rate_change*(h_depth(i)/2);
V_s_u2(i) = s_u0 + rate_change*h_depth(i);

% Calculating the resistance forces
V_Q_outer_SW(i) = h_depth(i)*alpha*V_s_u1(i)*(pi*D_outer);
V_Q_inner_SW(i) = h_depth(i)*alpha*V_s_u1(i)*(pi*D_inner);
V_Q_tip_SW(i) = (y_komma*h_depth(i)*Nq + V_s_u2(i)*Nc)*(pi*D_av*t);

V_Q_outer_plates_SA(i) = (h_depth(i)-H_split)*alpha*s_u1_SA*...
    (C_o_outerskirts+ C_o_innerskirts + C_o_diagonalskirts);
V_Q_inner_plates_SA(i) = (h_depth(i)-H_split)*alpha*s_u1_SA*...
    (C_i_outerskirts+ C_i_innerskirts + C_i_diagonalskirts);
V_Q_tip_plates_SA(i) = ((y_komma*(h_depth(i)-H_split)*Nq)+(s_u2_SA*Nc))...
    *((C_av_outerskirts+C_av_innerskirts+C_av_diagonalskirts)*t_plates);

V_Qtot_SW(i) = V_Q_outer_SW(i) + V_Q_inner_SW(i) + V_Q_tip_SW(i) +...
    V_Q_outer_plates_SW(i)+ V_Q_inner_plates_SW(i)+ V_Q_tip_plates_SW(i)...
    + Fbuoy_total;

% Holding Capacity Cylindrical Caisson
Q_su_SW(i) = alpha*s_u0*pi*D_outer*h_depth(i);
Q_b_SW(i) = s_u0*Nc_isk*f*((pi*(D_outer)^2)/4);
W_c_SW(i) = (4*WeightForce_total)/9;
W_s_SW(i) = (((pi*(D_outer)^2)/4)*h_depth(i))*(y_komma);

H_c_SW(i) = Q_su_SW(i)+Q_b_SW(i)+W_c_SW(i)+W_s_SW(i);
H_c2_SW(i) = H_c_SW(i)/1000;

% Holding Capacity Square Caisson
Q_su_SQ_SW(i) = alpha*s_u0*(4*C_o_innerskirts)*(h_depth(i)-H_split);
Q_b_SQ_SW(i) = s_u0*Nc_isk*f*(A_SQ_outer);
W_c_SQ_SW(i) = (4*WeightForce_total)/9;
W_s_SQ_SW(i) = ((A_SQ_outer)*(h_depth(i)-H_split))*(y_komma);

H_c_SQ_SW(i) = Q_su_SQ_SW(i)+Q_b_SQ_SW(i)+W_c_SQ_SW(i)+W_s_SQ_SW(i);
H_c2_SQ_SW(i) = H_c_SQ_SW(i)/1000;

% Holding Capacity Trapezoidal Caisson
Q_su_trap_SW(i) = alpha*s_u0*(4*C_outer_trap)*(h_depth(i)-H_split);
Q_b_trap_SW(i) = s_u0*Nc_isk*f*(A_trap_outer);
W_c_trap_SW(i) = (4*WeightForce_total)/9;
W_s_trap_SW(i) = ((A_trap_outer)*(h_depth(i)-H_split))*(y_komma);

H_c_trap_SW(i) = Q_su_trap_SW(i)+Q_b_trap_SW(i)+W_c_trap_SW(i)+...
    W_s_trap_SW(i);

```

```

H_c2_trap_SW(i) = H_c_trap_SW(i)/1000;
end

end

%% For loop for the Suction Assisted penetration to determine force per depth
m = 1;
h_max = H_inner;
h_depth_SA = [h_Self_Weight:0.001:h_max];

%-----
% Calculating the Suction Assisted penetration phase (Cohesive case)
%-----
for i = 1:length(h_depth_SA)
s_u1_SA(i) = s_u0 + rate_change*(h_depth_SA(i)/2);
s_u2_SA(i) = s_u0 + rate_change*h_depth_SA(i);
Nc_star = 3*4*alpha;
D_m = m*D_av;

% Calculating the critical suction by Yuqi
s_crit_Y(i) = (y_komma*(h_depth_SA(i)) + ((4*(h_depth_SA(i))*alpha*...
(s_u1_SA(i)))/D_inner))-(y_komma*(h_depth_SA(i)) + (((1+((1.5*...
(h_depth_SA(i))/D_outer))^2)*alpha*(s_u1_SA(i)))/(1+((3*...
(h_depth_SA(i))/D_outer)))) + (2 + pi + asin(alpha) + asin(alpha)...
+ sqrt(1-(alpha^2)) - sqrt(1-(alpha^2)))*(s_u2_SA(i));

if h_depth_SA(i) < (H_split)
% Part where the plate does not yet reach the seabed

% Initializing the resistance forces of the plates , which are zero in
% this part
V_Q_outer_plates_SA(i) = 0;
V_Q_inner_plates_SA(i) = 0;
V_Q_tip_plates_SA(i) = 0;

% Calculating the suction variable s [Pa]
syms p2
eqn = WeightForce_total + p2*((pi*(D_inner)^2)/4) == h_depth_SA(i)*alpha*...
s_u1_SA(i)*(pi*D_outer)+ h_depth_SA(i)*alpha*s_u1_SA(i)*(pi*D_inner)...
+ (y_komma*h_depth_SA(i)*Nq - p2 + s_u2_SA(i)*Nc)*(pi*D_av*t) + ...
V_Q_outer_plates_SA(i) + V_Q_inner_plates_SA(i) + V_Q_tip_plates_SA(i)...
+ Fbuoy_total;

s2(i) = double (solve(eqn,p2));

% Calculating the forces acting within the system
V_Force_SA(i) = WeightForce_total + s2(i)*((pi*(D_inner)^2)/4);
V_Q_outer_SA(i) = h_depth_SA(i)*alpha*s_u1_SA(i)*(pi*D_outer);
V_Q_inner_SA(i) = h_depth_SA(i)*alpha*s_u1_SA(i)*(pi*D_inner);
V_Q_tip_SA(i) = (y_komma*h_depth_SA(i)*Nq - s2(i) + s_u2_SA(i)*Nc)...
*(pi*D_av*t);

```

```

V_Qtot_SA(i) = V_Q_outer_SA(i) + V_Q_inner_SA(i) + V_Q_tip_SA(i) + ...
    V_Q_outer_plates_SA(i) + V_Q_inner_plates_SA(i) + V_Q_tip_plates_SA(i)...
    + Fbuoy_total;

% Holding Capacity Cylindrical Caisson
Q_su_SA(i) = alpha*s_u0*pi*D_outer*h_depth_SA(i);
Q_b_SA(i) = s_u0*Nc_isk*f*((pi*(D_outer)^2)/4);
W_c_SA(i) = (4*WeightForce_total)/4;
W_s_SA(i) = (((pi*(D_outer)^2)/4)*h_depth_SA(i))*(y_komma);

H_c_SA(i) = Q_su_SA(i)+Q_b_SA(i)+W_c_SA(i)+W_s_SA(i);
H_c2_SA(i) = H_c_SA(i)/1000;

% Holding Capacity Square Caisson
H_c2_SQ_SA(i) = 0;

% Holding Capacity Trapezoidal Caisson
H_c2_trap_SA(i) = 0;

else
% Part where the plate does reach the seabed

% Initializing the resistance forces of the plates, which are nonzero in
% this part
V_Q_outer_plates_SA(i) = (h_depth_SA(i)-H_split)*alpha*s_u1_SA(i)*...
    (C_o_outerskirts+ C_o_innerskirts + C_o_diagonalskirts);
V_Q_inner_plates_SA(i) = (h_depth_SA(i)-H_split)*alpha*s_u1_SA(i)*...
    (C_i_outerskirts+ C_i_innerskirts + C_i_diagonalskirts);
V_Q_tip_plates_SA(i) = ((y_komma*(h_depth_SA(i)-H_split)*Nq)+...
    (s_u2_SA(i)*Nc))*((C_av_outerskirts+C_av_innerskirts+...
    C_av_diagonalskirts)*t_plates);

% Calculating the variable s [Pa]
syms p2
eqn = WeightForce_total + p2*((pi*(D_inner)^2)/4) == h_depth_SA(i)*alpha*...
    s_u1_SA(i)*(pi*D_outer)+ h_depth_SA(i)*alpha*s_u1_SA(i)*(pi*D_inner)...
    + (y_komma*h_depth_SA(i)*Nq - p2 + s_u2_SA(i)*Nc)*(pi*D_av*t) + ...
    V_Q_outer_plates_SA(i) + V_Q_inner_plates_SA(i) + V_Q_tip_plates_SA(i)...
    + Fbuoy_total;

s2(i) = double (solve(eqn,p2));

% Calculating the forces acting within the system
V_Force_SA(i) = WeightForce_total + s2(i)*((pi*(D_inner)^2)/4);
V_Q_outer_SA(i) = h_depth_SA(i)*alpha*s_u1_SA(i)*(pi*D_outer);
V_Q_inner_SA(i) = h_depth_SA(i)*alpha*s_u1_SA(i)*(pi*D_inner);
V_Q_tip_SA(i) = (y_komma*h_depth_SA(i)*Nq - s2(i) + s_u2_SA(i)*Nc)*...
    (pi*D_av*t);
V_Qtot_SA(i) = V_Q_outer_SA(i) + V_Q_inner_SA(i) + V_Q_tip_SA(i)...
    + V_Q_outer_plates_SA(i) + V_Q_inner_plates_SA(i) + ...
    V_Q_tip_plates_SA(i) + Fbuoy_total;

```



```

% Holding Capacity Cylindrical Caisson
Q_su_SA(i) = alpha*s_u0*pi*D_outer*h_depth_SA(i);
Q_b_SA(i) = s_u0*Nc_isk*f*((pi*(D_outer)^2)/4);
W_c_SA(i) = (4*WeightForce_total)/9;
W_s_SA(i) = (((pi*(D_outer)^2)/4)*h_depth_SA(i))*(y_komma);

H_c_SA(i) = Q_su_SA(i)+Q_b_SA(i)+W_c_SA(i)+W_s_SA(i);
H_c2_SA(i) = H_c_SA(i)/1000;

% Holding Capacity Square Caisson
Q_su_SQ_SA(i) = alpha*s_u0*(4*C_o_innerskirts)*(h_depth_SA(i)-H_split);
Q_b_SQ_SA(i) = s_u0*Nc_isk*f*(A_SQ_outer);
W_c_SQ_SA(i) = (4*WeightForce_total)/9;
W_s_SQ_SA(i) = ((A_SQ_outer)*(h_depth_SA(i)-H_split))*(y_komma);

H_c_SQ_SA(i) = Q_su_SQ_SA(i)+Q_b_SQ_SA(i)+W_c_SQ_SA(i)+W_s_SQ_SA(i);
H_c2_SQ_SA(i) = H_c_SQ_SA(i)/1000;

% Holding Capacity Trapezoidal Caisson
Q_su_trap_SA(i) = alpha*s_u0*(4*C_outer_trap)*(h_depth_SA(i)-H_split);
Q_b_trap_SA(i) = s_u0*Nc_isk*f*(A_trap_outer);
W_c_trap_SA(i) = (4*WeightForce_total)/9;
W_s_trap_SA(i) = ((A_trap_outer)*(h_depth_SA(i)-H_split))*(y_komma);

H_c_trap_SA(i) = Q_su_trap_SA(i)+Q_b_trap_SA(i)+W_c_trap_SA(i)+...
    W_s_trap_SA(i);
H_c2_trap_SA(i) = H_c_trap_SA(i)/1000;

% Testing the suction against the critical suction, to determine if
% the square chamber is necessary

if s2(i) < s_crit_Y(i)
    s2(i) = s2(i);
else

% The plating for that is not used as a caisson is now
% determined for a full system instead of a quarter
V_Q_outer_plates_SA(i) = (h_depth_SA(i)-H_split)*alpha*s_u1_SA(i)*...
    ((4*C_o_outerskirts)+(4*C_o_diagonalskirts));
V_Q_inner_plates_SA(i) = (h_depth_SA(i)-H_split)*alpha*s_u1_SA(i)*...
    ((4*C_i_outerskirts)+(4*C_i_diagonalskirts));
V_Q_tip_plates_SA(i) = ((y_komma*(h_depth_SA(i)-H_split)*Nq)+(s_u2_SA(i)*...
    *Nc))*(((4*C_av_outerskirts)+(4*C_av_diagonalskirts))*t_plates);

% Calculating the new variable s [Pa], based on the full system
% In this equation, the additional terms for the square
% caisson are taken into account

syms p2
eqn = (4*WeightForce_total) + 4*(p2*((pi*(D_inner)^2)/4)) + (p2*A_SQ_inner)...
```

```

== 4*(h_depth_SA(i)*alpha*s_u1_SA(i)*(pi*D_outer)+ h_depth_SA(i)*...
alpha*s_u1_SA(i)*(pi*D_inner) + (y_komma*h_depth_SA(i)*Nq - p2 + ...
s_u2_SA(i)*Nc)*(pi*D_av*t))+(h_depth_SA(i)-H_split)*alpha*s_u1_SA(i)...
*(4*C_o_innerskirts)+ (h_depth_SA(i)-H_split)*alpha*s_u1_SA(i)*...
(4*C_i_innerskirts) + ( y_komma*(h_depth_SA(i)-H_split)*Nq - p2 +...
s_u2_SA(i)*Nc)*(A_SQ_tip)+ V_Q_outer_plates_SA(i) + ...
V_Q_inner_plates_SA(i) + V_Q_tip_plates_SA(i) + 4*(Fbuoy_total);

s2(i) = double (solve(eqn,p2));

% Calculating the forces acting within the system
V_Force_SA(i) = WeightForce_total + s2(i)*((pi*(D_inner)^2)/4);
V_Q_outer_SA(i) = h_depth_SA(i)*alpha*s_u1_SA(i)*(pi*D_outer);
V_Q_inner_SA(i) = h_depth_SA(i)*alpha*s_u1_SA(i)*(pi*D_inner);
V_Q_tip_SA(i) = (y_komma*h_depth_SA(i)*Nq - s2(i) + s_u2_SA(i)*Nc)...
*(pi*D_av*t);

% Calculating the terms for the square suction caisson
V_Q_outer_SA_SQ(i) = (h_depth_SA(i)-H_split)*alpha*s_u1_SA(i)*...
(4*C_o_innerskirts);
V_Q_inner_SA_SQ(i) = (h_depth_SA(i)-H_split)*alpha*s_u1_SA(i)*...
(4*C_i_innerskirts);
V_Q_tip_SA_SQ(i) = (y_komma*(h_depth_SA(i)-H_split)*Nq - s2(i)...
+ s_u2_SA(i)*Nc)*(A_SQ_tip);

V_Qtot_SA(i) = V_Q_outer_SA(i) + V_Q_inner_SA(i) + V_Q_tip_SA(i) + ...
V_Q_outer_plates_SA(i)+ V_Q_outer_SA_SQ(i) + V_Q_inner_SA_SQ(i) ...
+ V_Q_tip_SA_SQ(i) + V_Q_inner_plates_SA(i) + V_Q_tip_plates_SA(i) ...
+ 4*Fbuoy_total;

% Holding Capacity Cylindrical Caisson
Q_su_SA(i) = alpha*s_u0*pi*D_outer*h_depth_SA(i);
Q_b_SA(i) = s_u0*Nc_isk*f*((pi*(D_outer)^2)/4);
W_c_SA(i) = (4*WeightForce_total)/9;
W_s_SA(i) = (((pi*(D_outer)^2)/4)*h_depth_SA(i))*(y_komma);

H_c_SA(i) = Q_su_SA(i)+Q_b_SA(i)+W_c_SA(i)+W_s_SA(i);
H_c2_SA(i) = H_c_SA(i)/1000;

% Holding Capacity Square Caisson
Q_su_SQ_SA(i) = alpha*s_u0*(4*C_o_innerskirts)*(h_depth_SA(i)-H_split);
Q_b_SQ_SA(i) = s_u0*Nc_isk*f*(A_SQ_outer);
W_c_SQ_SA(i) = (4*WeightForce_total)/9;
W_s_SQ_SA(i) = ((A_SQ_outer)*(h_depth_SA(i)-H_split))*(y_komma);

H_c_SQ_SA(i) = Q_su_SQ_SA(i)+Q_b_SQ_SA(i)+W_c_SQ_SA(i)+W_s_SQ_SA(i);
H_c2_SQ_SA(i) = H_c_SQ_SA(i)/1000;

% Holding Capacity Trapezoidal Caisson
Q_su_trap_SA(i) = alpha*s_u0*(4*C_outer_trap)*(h_depth_SA(i)-H_split);
Q_b_trap_SA(i) = s_u0*Nc_isk*f*(A_trap_outer);

```

```

W_c_trap_SA(i) = (4*WeightForce_total)/9;
W_s_trap_SA(i) = ((A_trap_outer)*(h_depth_SA(i)-H_split))*(y_komma);

H_c_trap_SA(i) = Q_su_trap_SA(i)+Q_b_trap_SA(i)+W_c_trap_SA(i)+...
    W_s_trap_SA(i);
H_c2_trap_SA(i) = H_c_trap_SA(i)/1000;

end

% Testing the suction against the critical suction, to determine if
% the trapezoidal chambers are necessary
if s2(i) < s_crit_Y(i)
    s2(i) = s2(i);
else

V_outer_plates(i) = 0;
V_inner_plates(i) = 0;
V_tip_plates(i) = 0;

% Calculating the new variable s [Pa], based on the full system
% In this equation, the additional terms for the square and
% trapezoidal caisson are taken into account
syms p2
eqn = (4*WeightForce_total) + 4*(p2*((pi*(D_inner)^2)/4)) + (p2*A_SQ_inner)...
    == 4*(h_depth_SA(i)*alpha*s_u1_SA(i)*(pi*D_outer)+ h_depth_SA(i)*...
    alpha*s_u1_SA(i)*(pi*D_inner) + (y_komma*h_depth_SA(i)*Nq - p2 + ...
    s_u2_SA(i)*Nc)*(pi*D_av*t)) + (h_depth_SA(i)-H_split)*alpha*s_u1_SA(i)...
    *(4*C_o_innerskirts)+ (h_depth_SA(i)-H_split)*alpha*s_u1_SA(i)*...
    (4*C_i_innerskirts) + (y_komma*(h_depth_SA(i)-H_split)*Nq - p2 + ...
    s_u2_SA(i)*Nc)*(A_SQ_tip)+ 4*((h_depth_SA(i)-H_split)*alpha*s_u1_SA(i)...
    *(C_outer_trap)+(h_depth_SA(i)-H_split)*alpha*s_u1_SA(i)*...
    (C_inner_trap) + (y_komma*(h_depth_SA(i)-H_split)*Nq - p2 + s_u2_SA(i)...
    *Nc)*(A_tip_trap))+V_Q_outer_plates_SA(i) + V_Q_inner_plates_SA(i)...
    + V_Q_tip_plates_SA(i) + 4*(Fbuoy_total);

s2(i) = double (solve(eqn,p2));

% Calculating the forces acting within the system
V_Force_SA(i) = WeightForce_total + s2(i)*((pi*(D_inner)^2)/4);
V_Q_outer_SA(i) = h_depth_SA(i)*alpha*s_u1_SA(i)*(pi*D_outer);
V_Q_inner_SA(i) = h_depth_SA(i)*alpha*s_u1_SA(i)*(pi*D_inner);
V_Q_tip_SA(i) = (y_komma*h_depth_SA(i)*Nq - s2(i) + s_u2_SA(i)*Nc)...
    *(pi*D_av*t);

% Calculating the terms for the square suction caisson
V_Q_outer_SA_SQ(i) = (h_depth_SA(i)-H_split)*alpha*s_u1_SA(i)*...
    (4*C_o_innerskirts);
V_Q_inner_SA_SQ(i) = (h_depth_SA(i)-H_split)*alpha*s_u1_SA(i)*...
    (4*C_i_innerskirts);
V_Q_tip_SA_SQ(i) = (y_komma*(h_depth_SA(i)-H_split)*Nq - s2(i) +...
    s_u2_SA(i)*Nc)*(A_SQ_tip);

```

```

% Calculating the terms for the square suction caisson
V_Q_outer_SA_trap(i)= (h_depth_SA(i)-H_split)*alpha*s_u1_SA(i)*...
    (C_outer_trap);
V_Q_inner_SA_trap(i)= (h_depth_SA(i)-H_split)*alpha*s_u1_SA(i)*...
    (C_inner_trap);
V_Q_tip_SA_trap(i)= (y_komma*(h_depth_SA(i)-H_split)*Nq - s2(i) +...
    s_u2_SA(i)*Nc)*(A_tip_trap);

% Holding Capacity Cylindrical Caisson
Q_su_SA(i) = alpha*s_u0*pi*D_outer*h_depth_SA(i);
Q_b_SA(i) = s_u0*Nc_isk*f*((pi*(D_outer)^2)/4);
W_c_SA(i) = (4*WeightForce_total)/9;
W_s_SA(i) = (((pi*(D_outer)^2)/4)*h_depth_SA(i))*(y_komma);

H_c_SA(i) = Q_su_SA(i)+Q_b_SA(i)+W_c_SA(i)+W_s_SA(i);
H_c2_SA(i) = H_c_SA(i)/1000;

% Holding Capacity Square Caisson
Q_su_SQ_SA(i) = alpha*s_u0*(4*C_o_innerskirts)*(h_depth_SA(i)-H_split);
Q_b_SQ_SA(i) = s_u0*Nc_isk*f*(A_SQ_outer);
W_c_SQ_SA(i) = (4*WeightForce_total)/9;
W_s_SQ_SA(i) = ((A_SQ_outer)*(h_depth_SA(i)-H_split))*(y_komma);

H_c_SQ_SA(i) = Q_su_SQ_SA(i)+Q_b_SQ_SA(i)+W_c_SQ_SA(i)+W_s_SQ_SA(i);
H_c2_SQ_SA(i) = H_c_SQ_SA(i)/1000;

% Holding Capacity Trapezoidal Caisson
Q_su_trap_SA(i) = alpha*s_u0*(4*C_outer_trap)*(h_depth_SA(i)-H_split);
Q_b_trap_SA(i) = s_u0*Nc_isk*f*(A_trap_outer);
W_c_trap_SA(i) = (4*WeightForce_total)/9;
W_s_trap_SA(i) = ((A_trap_outer)*(h_depth_SA(i)-H_split))*(y_komma);

H_c_trap_SA(i) = Q_su_trap_SA(i)+Q_b_trap_SA(i)+W_c_trap_SA(i)+...
    W_s_trap_SA(i);
H_c2_trap_SA(i) = H_c_trap_SA(i)/1000;
    end
end
end

%% Plotting the behaviour of the foundation system

%-----
% Plotting the behaviour of the foundation system for individual phases
% (Cohesive case)
%-----

% Plotting the total resistance force against the penetration depth
figure(1)
plot(h_depth, V_Qtot_SW)
title('Total resistance force during the Selfweight penetration phase')

```

```

xlabel('Penetration depth [m]')
ylabel('Total resistance force [N]')

figure(2)
plot(h_depth_SA,s2)
title('Suction required for a total depth of 0.5 m')
xlabel('Penetration depth [m]')
ylabel('Required suction [Pa]')

figure(3)
plot(h_depth_SA,V_Qtot_SA)
title('Total resistance forces during the suction assisted phase')
xlabel('Penetration depth [m]')
ylabel('Total resistance force [N]')

figure(4)
plot(h_depth_SA,V_Q_tip_SA)
title('Resistance force at the tips during the suction assisted phase')
xlabel('Penetration depth [m]')
ylabel('Resistance force at the tips [N]')

figure(5)
plot(h_depth_SA,V_Q_inner_SA)
title('Resistance force at the inside of the caisson during the suction assisted phase')
xlabel('Penetration depth [m]')
ylabel('Resistance force at the inside of the caisson [N]')

figure(6)
plot(h_depth_SA,V_Q_outer_SA)
title('Resistance force at the outside of the caisson during the suction assisted phase')
xlabel('Penetration depth [m]')
ylabel('Resistance force at the outside of the caisson [N]')

figure(7)
plot(h_depth_SA, V_Q_outer_SA)
hold on
plot(h_depth_SA, V_Q_inner_SA)
hold on
plot(h_depth_SA, V_Q_tip_SA)
hold off

title('Resistance forces during the suction assisted penetration phase')
xlabel('Penetration depth [m]')
ylabel('Resistance force [N]')
legend('Outer resistance force', 'Inner resistance force',...
      'Tip resistance force')

%-----
% Plotting the behaviour of the foundation system for all phases
% (Cohesive case)
%-----

```

```

h_tot = [h_depth h_depth_SA];
V_Q_outer_tot = [V_Q_outer_SW V_Q_outer_SA];
V_Q_inner_tot = [V_Q_inner_SW V_Q_inner_SA];
V_Q_tip_tot = [V_Q_tip_SW V_Q_tip_SA];
V_Qtot = [V_Qtot_SW V_Qtot_SA];
H_c2 = [H_c2_SW H_c2_SA];
H_c2_SQ = [H_c2_SQ_SW H_c2_SQ_SA];
H_c2_trap = [H_c2_trap_SW H_c2_trap_SA];

figure(8)
plot(h_tot,V_Qtot)
title('Total resistance force during the installation')
xlabel('Penetration depth [m]')
ylabel('Total resistance force [N]')

figure(9)
plot(h_tot, V_Q_outer_tot)
hold on
plot(h_tot, V_Q_inner_tot)
hold on
plot(h_tot, V_Q_tip_tot)
hold off

title('Resistance forces over the penetration depth')
xlabel('Penetration depth [m]')
ylabel('Resistance force [N]')
legend('Outer resistance force', 'Inner resistance force',...
       'Tip resistance force', 'Location', 'Southeast')

% critical suction
figure(10)
plot(h_depth_SA,s2)
hold on
%plot(h_depth_SA,s_crit)
%hold on
plot(h_depth_SA,s_crit_Y)
hold off

title('Calculated suction vs Critical suction ')
xlabel('Penetration depth [m]')
ylabel('Required suction [Pa]')
legend('Calculated Suction', 'Critical Suction Yuqi',...
       'Location', 'Southeast')

figure(11)
plot(h_tot,H_c2)
hold on
plot(h_tot,H_c2_SQ)
hold on
plot(h_tot,H_c2_trap)

```

```

hold off

title('Holding capacity of one suction caisson')
xlabel('Penetration depth [m]')
ylabel('Holding capacity [kN]')
legend('Circular Caissons', 'Square Caisson', 'Trapezoidal Caisson' , ...
       'Location', 'Southeast')

end

```